SPIN STRUCTURE OF ANTIFERROMAGNETIC THIN FILMS INVESTIGATED WITH SPIN-POLARIZED SCANNING TUNNELING MICROSCOPY

Dissertation

zur Erlangung des akademischen Grades

Dr. rer. nat.

vorgelegt der

die Naturwissenschaftliche Fakultät II
Institut für Physik
der Martin-Luther-Universität Halle-Wittenberg

von Herrn Chunlei Gao
geboren am 16.03.1977 in China

Gutachter:

1. Prof. Dr. Jürgen Kirschner

2. Prof. Dr. Henning Neddermeyer

3. Prof. Dr. Markus Morgenstern

Halle (Saale), 2006

verteidigt am 18.12.2006

.

Abstract

The objective of this thesis is to investigate noncollinear antiferromagnetic surface spin structures with spin-polarized scanning tunneling microscopy (Sp-STM). The spin-polarized measurements are realized by using a soft magnetic ring as the scanning electrode. A complete separation of topographic and spin signal is achieved through operating the Sp-STM in the differential magnetic mode. Two systems were studied. First, a large $(\sqrt{10} \times 2\sqrt{10})R18.4°$ reconstruction of Mn films with a noncollinear spin structure was found on Fe(001). By combining maps of the spin polarization of two orthogonal directions, the vector field of the polarization in the unit cell was fully constructed. Nearly antiparallel alignments of surface Mn moments was resolved on atomic scale. The complex behavior is explained on basis of the tendency of Mn to form antiferromagnetic coupled surface dimers. Second, the spin structure of chemical ordered NiMn thin films on Cu(001) was investigated. An in-plane magnetic compensated surface was found. Different spin polarizations of Ni and Mn were observed. A partially antiferromagnetic coupling between surface Mn (Ni) moments was attributed to be responsible to the $p(2 \times 2)$ reconstruction of the surface. The experimental results are compared with the first principle calculations.

Kurzfassung

Das Ziel dieser Dissertation ist die Untersuchung von nicht-kollinearen antiferromagnetischen Oberflächenspinstrukturen mittels der spinpolarisierten Rastertunnelmikroskopie. Die spinpolarisierten Rastermessungen wurden durch die Benutzung einer weichmagnetischen Ringelektrode ermöglicht. Die topographischen Signale und die Spinsignale konnten durch Messungen im differentiellen magnetischen Modus getrennt werden. Es wurden zwei Systeme ultradünner Filme untersucht. Zunächst wurde bei Manganfilmen, die auf einer Fe(001)-Oberfläche gewachsenen wurden, eine neue $(\sqrt{10} \times 2\sqrt{10})R18.4°$ Oberflächenrekonstruktion mit nicht-kollinearer Spinstruktur gefunden. Durch Vergleich von spinpolarisierten Messungen in zwei zueinander senkrechten Richtungen konnte das volle Vektorfeld der Spinpolarisation in der Oberflächeneinheitszelle rekonstruiert werden. Die nahezu antiparallele Ausrichtung der magnetischen Momente der Manganatome an der Oberfläche konnte mit atomarer Auflösung gezeigt werden. Dieses Verhalten kann damit erklärt werden, dass die Manganatome eine Tendenz dazu zeigen, antiferromagnetisch gekoppelte Dimere zu bilden. Weiterhin wurde die Spinstruktur von antiferromagnetisch geordneten dünnen Filmen aus NiMn auf Cu(001) untersucht. Diese Filme zeigen in der Oberflächenebene kompensierte magnetische Momente. Es wurde eine unterschiedlich große Spinpolarisation der Ni und Mn-Atome beobachtet. Eine partielle antiferromagnetische Kopplung der Mn- und Ni-Oberflächenmomente führt zur Entstehung einer p(2x2) Obeflächenrekonstruktion. Die dazugehörigen experimentellen Resultate werden mit *ab-initio* Rechnungen verglichen.

Contents

1. Introduction

In the past few decades, magnetic thin films and nanostructures were intensively studied in various aspects for their importance in both fundamental physics and application. Among these studies the magnetic domain imaging techniques played an important role because magnetic domains link the physical properties of atoms with the macroscopic behaviors of magnetic materials [1]. Hand-in-hand with the increasing density of magnetic recording medium achieved mainly by reducing the size of single recording bits, an improving resolution in magnetic imaging has been required. Different techniques using different detection media such as magnetic powder, LASER, x-rays, electrons and even neutrons were developed. In general, the magnetic imaging techniques are divided into two branches. One branch is mapping the local magnetic field which emerges from the sample (magnetic stray field). A method of this kind is the Bitter-technique developed in 1932 [2] in which the tiny magnets (magnetic powder) align to the stray field of the sample. A resolution of a few 10 nanometers was achieved with this technique [3]. Another technique which detects the stray field is magnetic force microscopy (MFM). The magnetostatic interaction between a magnetic tip and the stray field of the sample surface is analyzed with respect to the lateral position of the tip [4]. The resolution is about 20 nm to 100 nm [5]. The second branch of magnetic imaging techniques utilizes the interaction of photons, electrons and neutrons with the spin-polarized electronic structure or local magnetic field within the atoms of the magnetic materials. For example, Magneto-optical Kerr microscopy is based on the phenomenon that the polarization of light is changed when it is reflected from a magnetic sample [6]. The resolution is limited by the wavelength, typically in a few hundred nanometers [7]. Lorentz microscopy, which utilizes the Lorentz effect when electrons transverse the magnetic sample, has a resolution in the nanometer range [8]. Surface sensitive techniques were also developed such as scanning electron microscopy with polarization analysis (SEMPA) and spin-polarized low energy electron microscopy (SPLEEM). SEMPA measures the spin polarization of the secondary electrons that are emitted from a magnetic sample while a finely focused unpolarized high energy electron beam (10 KeV) scans over the sample surface. The first experiment was done by Koike et al. in 1987 [9]. The resolution of SEMPA is around tens of nanometer. SPLEEM uses a spin-polarized low energy electron beam ($\sim$10 eV) to hit the magnetic sample. The spin contrast in the reflected beam arises from the exchange interaction and the different inelastic mean free paths of electrons with spin parallel and antiparallel to the spin of the electrons in the ferromagnetic sample [10]. Another

technique called photoemission electron microscopy (PEEM) has an advantage of element specificity which enables to detect the alignment of each element in alloys or in the multilayers [11]. All these techniques yield insight into magnetism and magnetic material and have their advantages and drawbacks. From the resolution point of view, these techniques cannot achieve atomic resolution while the magnetic moments of the atoms are the basic building blocks of magnetic materials. Recently, spin-polarized scanning tunneling microscopy (Sp-STM) [12] demonstrated atomic resolution of spin on a two-dimensional antiferromagnetic surface which opens a door to the study of magnetism on the atomic scale.

Structurally, atomic resolution was achieved in scanning tunneling microscopy (STM) which was developed by Binnig and Rohrer in 1981 [13, 14]. This technique utilizes the electron tunneling effect where the tunneling current depends exponentially on the distance between the tip and sample. When the tip scans over the surface, a contour map which reflects the local charge density is recorded. The idea of Sp-STM is based on the tunneling magnetoresistance (TMR) effect [15] as first proposed by Pierce in 1988 [16]. Due to the TMR effect, the tunneling probability between two ferromagnetic electrodes separated by an insulating layer depending on the relative orientation of the magnetization of the electrodes. In the STM geometry, the vacuum barrier replaces the insulating layer. Experimentally, different approaches were tried to obtain the spin-dependent tunneling effect in the scanning configuration. One method, which was not very successful, is using optically pumped semiconducting GaAs tips [17]. Through changing the helicity of the LASER light, the spin polarization of the tunneling current is modulated. Thus, depending on the geometry of incident light, both in-plane and out-of-plane sensitivity can be achieved. An alternative method is simply using a ferromagnetic tip. There are three different operation modes: constant current mode, spectroscopic mode and differential magnetic mode. Details of these three modes will be discussed in the next Chapter. In all these modes, atomic resolution of the magnetic moments was achieved.

Most of the magnetic domain imaging techniques focus on ferromagnetic materials. In ferromagnetic domains, all the atomic moments are pointing to one direction which give a net magnetization. The size of the ferromagnetic domains varies from a few tens nanometers to several hundred micrometers or even more which are relatively easy to observe. In many magnetic devices, antiferromagnetic materials are in direct contact with ferromagnetic materials as a pinning layer. The physical origin of the coupling between the ferromagnetic and antiferromagnetic layers at the interface gained a lot of interest in recent years. This phenomenon is not fully understood, yet. One important reason for that is the lack of knowledge about the spin structure of the antiferromagnetic material at the interface. It is difficult to map the spin structure of antiferromagnetic materials as these systems show no net magnetic moment. Traditional methods applied in measuring the antiferromagnetic structures are usually bulk sensitive such as neutron diffraction [18, 19], magnetic torque measurements [20] and nuclear magnetic resonance [21]. These methods measure

collective effects. A certain amount of material is needed to have a reasonable signal to noise ratio. As to antiferromagnetic surfaces, there are two types of surface configurations. One has net magnetic moments at the surface (uncompensated surface), e.g., layer-wise antiferromagnetic structures like Mn/Fe(001) [22, 23] or Cr(001) [24]. They have opposite magnetic direction between adjacent atomic layers. If the terraces are large enough (a few ten nm), the spin contrast from the different layers can be resolved with SEMPA [25]. As to antiferromagnetic surfaces which are compensated, in some collinear cases, X-ray magnetic linear dichroism (XMLD)-PEEM can determine the direction of magnetic axis of collinear spin structure [26]. A real imaging of the spin configuration, especially the noncollinear spin structure of compensated surfaces needs atomic resolution. This was realized with the development of Sp-STM.

This work focuses on mapping the spin structure of antiferromagnetic surfaces with Sp-STM using a ferromagnetic ring electrode operating in the differential magnetic mode. Single crystalline Mn and equiatomic NiMn were studied. The thesis is organized as following: In Chapter 2, a brief description of STM and Sp-STM is given. The resolution of STM and Sp-STM is discussed. The experimental setup, the preparation of the ring electrode and the realization of spin-dependent measurements are discussed in Chapter 3. The layer-wise antiferromagnetic Mn films on Fe(001) were measured as a test of the ring electrodes. Chapter 4 focuses on the spin configuration of reconstructed Mn films on Fe(001). The growth and morphology were characterized with low energy electron diffraction (LEED) and STM. An antiferromagnetic coupling of the surface atoms was observed by comparing the atomically resolved spin image with the topography within the reconstruction unit cells. Further, two orthogonal spin-polarized measurements show that the reconstruction has a noncollinear spin structure. By combining the two measurements, a vector field of spin polarization was constructed. Chapter 5 describes the spin structure of NiMn thin films on Cu(001). First, the growth and structure of NiMn films on Cu(001) were discussed. A chemically ordered equiatomic structure of NiMn was found. Extraordinary large buckling of surface atoms was observed with LEED and STM. Sp-STM measurements show spin contrast between Ni and Mn atoms at the surface, and between surface Mn (Ni) atoms as well depending on the bias voltage. *Ab-initio* calculations show the antiferromagnetic coupling between nearest Mn atoms is the ground state. The comparison between experimental results and theoretical calculations gives a good agreement. A possible spin structure of NiMn thin films is proposed. First measurements with Sp-STM were done on Co/NiMn/Cu(001). The relation between the ferromagnetic and antiferromagnetic domains are discussed. Further experiments to verify the assumption are proposed. Finally, a conclusion is given in Chapter 6.

.

2. Theoretical background

2.1   Antiferromagnetism: from bulk to thin films

An atom may carry a permanent magnetic moment depending on its electronic structure. The interaction between magnetic atoms results in different magnetic effects. The spontaneous magnetic order comes from a strong interaction, i.e., the exchange interaction, which can be described by the exchange integral J_e. When J_e is positive, the atomic moments align parallel; the substance is said to be ferromagnetic. When J_e is negative, an antiparallel arrangement of the strongly coupled atomic dipoles is favored which defines the antiferromagnetic order. For ferromagnetic materials, the spontaneous magnetic order occurs below a critical temperature, i.e., the Curie temperature T_C. The counterpart in antiferromagnetism is the Néel temperature (T_N). That is, T_N is the temperature above which the ordered arrangement of the magnetic moments disappear.

The main difference in macroscopic behavior between ferromagnetic and antiferromagnetic material is that the antiferromagnet shows no net magnetic moment which makes the study of antiferromagnetism not straightforward. A direct evidence of an antiparallel arrangement of the magnetic moments in antiferromagnets was provided by neutron diffraction methods developed essentially since 1945 [27]. Neutrons, generated from atomic power plants, have a wavelength comparable to the interatomic spacing in crystals and can thus be used to study the crystal structure. Besides the scattering by the atomic nuclei of crystalline materials, neutrons can also be scattered by atoms that have magnetic moments due to the fact that neutron possesses a nuclear spin. Since the scattering process is coherent when the substance has an ordered structure, the antiferromagnetic order can also be distinguished. Magnetic structures, exchange integrals, magnetic moments per atom can be extracted from neutron scattering measurements.

Most antiferromagnetic materials are compounds in which the cations are separated by much larger distances than atomic distances in ferromagnetic materials. The exchange interaction must occur indirectly via nonmagnetic anions such as O^{2-}, e.g. MnO, NiO [28, 29, 26]. Only few metals have been observed to possess antiferromagnetism such as Cr, Mn and some rare earth metals. Their antiferromagnetic properties differ considerably from those observed for compounds because the antiferromagnetic coupling happens within neighboring atoms via direct exchange. In

some cases, the antiferromagnetism may lead to an unusually complicated structure, for example, α-Mn [30] with its 58 atoms in the unit cell. Many antiferromagnetic alloys of transition metals are of interest due to their novel properties [31, 32].

Similar to ferromagnetic materials, domains are also present in antiferromagnetic materials. The antiferromagnetic domains, however, have a different origin compared to those in ferromagnetic materials. In ferromagnetism, the domains are defined as a regime where all the magnetic moments are pointing to the same direction. The formation of domains can reduce the magnetostatic energy through closing the magnetic flux. In antiferromagnetism, the presence of domains only increases the exchange energy because of additional disorder. Considering cooling an antiferromagnetic sample below its Néel temperature, it is reasonable to expect that in different regions of the crystal, the magnetic axis varies in direction. Thus, the structurally equivalent crystal axes are broken into magnetically inequivalent axes. One example is NiO [28, 26] where the magnetic moments are arranged in ferromagnetic sheets lying in the (111) plane. There are four equivalent (111) planes which resulting in four different magnetic inequivalent domains. There are transition regions between them where domain walls are expected. Crystalgraphic defects may be needed to form the antiferromagnetic domain walls. Since the magnetostatic energy is not present in antiferromagnetism, the wall thickness and energy mainly depends on the exchange and crystalline anisotropy energies. The existence of antiferromagnetic domains can reduce the magentoelastic energy.
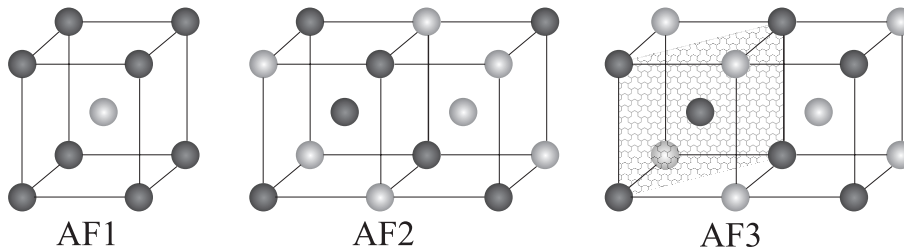

Figure 2.1: Three types of antiferromagnetic spin structure in body centered cubic structure. The black and white atoms represent the atoms with opposite magnetic moments. The magnetic moments are totally compensated in all three cases. They show different spin patterns at the surface. The details are discussed in the text.

Antiferromagnetic thin films have also been intensively studied. Besides polycrystalline films, a simple approach is to study single crystalline structure in epitaxially grown films such as Mn/Fe(001) [22, 23], Cr/Fe(001) [33], FeMn/Cu(001) [34]. Depending on the spin structure and crystalline orientation, the surface of the antiferromagnetic thin films shows various behaviors. As an example, Figure 2.1 gives three possible spin configurations of a body centered cubic (bcc) structure which are the so called antiferromagnetic structure type AF1, AF2 and AF3(011). Though in bulk, the magnetic moments are totally compensated, the crystal contains ferromagnetic sheets which are coupled antiferromagnetically to the neighboring

atomic sheets. Thus, if the crystal is cut through the low index planes, the surface can be compensated or uncompensated depending on the spin structure. As can be seen, the (001) surface is uncompensated in AF1 while compensated in AF2 and AF3. Similarly, the (011) plane shows net magnetic moments in AF3 but not in AF1 and AF2. The situation may be even more complicated at the surface region. Due to the reduction of neighboring atoms, the surface atoms tend to interact stronger with each other. The interactions can be of chemical, electronic or magnetic origin. Structurally, these interactions lead to the widely observed surface reconstructions. The study of the spin structure of antiferromagnetic surfaces is only possible with the development of Sp-STM [12]. The knowledge of the surface antiferromagnetic spin structure on the atomic level is important for understanding magnetically induced surface reconstructions (or vise versa), the evolvement of magnetism at the surface region.

2.2 Spin-polarized scanning tunneling microscopy

2.2.1 Scanning tunneling microscopy

Since the invention of scanning tunneling microscopy by Binnig and Rohrer [13, 14], STM has revolutionized the field of surface science and has become the basic experimental tool for nanoscience and nanotechnology. The physics underlaid in STM is the tunneling effect which can be simply explained by Fig. 2.2.

In classic mechanics, electrons below the work function are restricted in the solid and have no means to leave. According to quantum mechanics, wave functions of electrons decay exponentially into the vacuum which can be simply expressed in one dimension by the following equation,

$$\psi = Ae^{-2\sqrt{2m(\phi-E)}(Z/\hbar)} \tag{2.1}$$

where A is a constant, ϕ is the work function, Z is the distance to the surface and E is the energy measured with respect to the Fermi level. Therefore, the electrons have a non-vanishing probability to escape from the solid. When the tip and sample are far apart, they are independent. Their vacuum levels are equal, as shown in Fig. 2.2 (a). The Fermi levels (E_F) of the tip and sample lie below the vacuum level by their respective work functions ϕ_s and ϕ_t. If the tip and sample are brought together within a few atomic lattices, they tend to evolve into an equilibrium state where their Fermi levels are equal as illustrated in Fig. 2.2 (b). The tails of the wave functions of the tip and sample overlap in the vacuum region, the electrons have equal probability to tunnel from the tip to sample or vice versa. When a voltage V is applied to sample, the energy levels will be rigidly shifted upward or downward by amount of |eV| (cf. Fig. 2.2 (c) and (d)), depending on the polarity of the
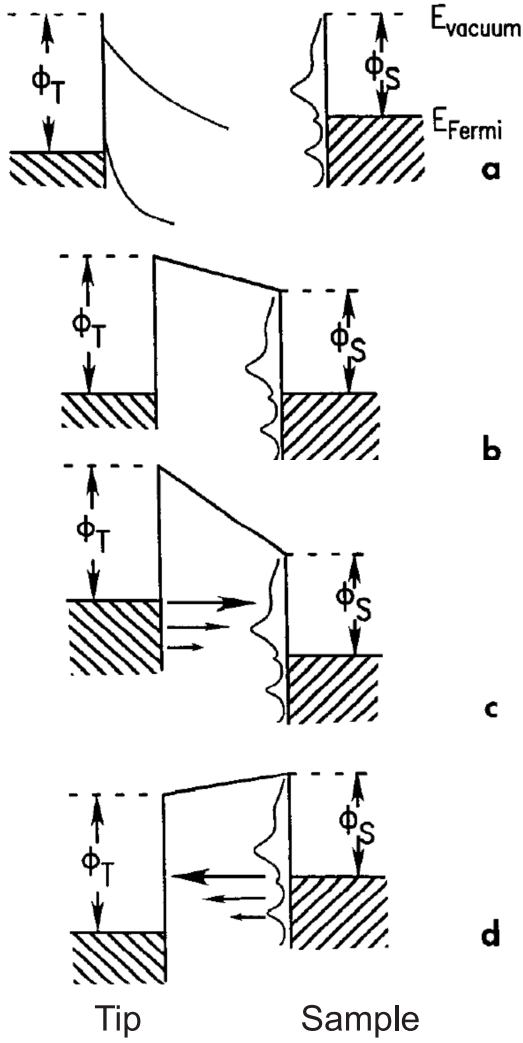
Figure 2.2: Energy level diagram for sample and tip. (a) Independent sample and tip. (b) Sample and tip at equilibrium, separated by small vacuum gap. (c) Positive sample bias: electrons tunnel from tip to sample. (d) Negative sample bias: electrons tunnel from sample to tip. Picture taken from [35]

applied voltage. A net tunneling current arises either from sample to tip or from tip to sample. The tunneling current I can be written in equation 2.2 based on the perturbative-transfer Hamiltonian formalism introduced by Bardeen [36].

$$I = e/\hbar \sum_{s,t} |M_{st}|^2 \delta(E_s - E_t)[f(E_s) - f(E_t + eV)] \tag{2.2}$$

Here, the δ-function means that the electrons do not lose energy during tunneling (elastic tunneling) and the Fermi-Dirac function $f(E)$ is taken into account because the tunneling can only occur from filled states into empty states. The energy shift eV is due to the applied bias voltage. The key problem in calculating the tunneling current is to calculate the tunnel matrix elements M_{st} which is the convolution of the tip and sample states

$$M_{st} = \hbar/2m \int dS(\psi_s^* \nabla \psi_t - \psi_t^* \nabla \psi_s) \tag{2.3}$$

8

The tunneling current depends on the overlap between the wave functions of the tip and sample in the tunneling barrier. Since the wave functions of the electrons decay exponentially into the tunneling barrier, the tunneling current depends exponentially on the distance between the tip and sample. This property of the tunneling current is used to operate the scanning tunneling microscopy.

A complete description of the tunneling current needs a full knowledge of the electronic states of the sample and tip. The STM tip is notoriously difficult to control. In the theory of STM, the description of the tip is simplified in various ways, among which, the Tersoff-Hamann [37, 38] approach is now widely used because of its simplicity and good explanation of STM images. It gives correct predictions in many standard situations, for example, in the research of molecular adsorption or surface reconstructions. In this approach, the tip is treated as a featureless spherical *s*-wave. The charge density is constant. Within this assumption, the tunnel matrix in equation 2.3 is much simplified. The tunneling current is proportional to the charge density at the surface:

$$I(\mathbf{R}) \propto \sum_{E_n > E_F - eV_{bias}}^{E_n < E_F} |\psi_s(\mathbf{R}, E_n)|^2 \qquad (2.4)$$

Thus, the density of states (DOS) above the sample surface in vacuum at the tip position determines the STM image. Within this model, it is estimated that a change of tip-surface distance by $1\,\text{Å}$ results in a variation of a factor of ten in the tunneling current. This implies that only the very apex atom of the tip dominates the tunneling process. The Tersoff-Hamann approach, however, failed to explain the large corrugations on close packed metal surface. This problem will be discussed again in section 2.4.

2.2.2 Spin-dependent tunneling effect

Since the electron carries both charge and spin, a challenging task is to detect the spin with atomic resolution. The first idea was proposed by Pierce [16] based on the tunneling magnetoresistance which was first discovered by Jullière [15] in 1975. In ferromagnetic materials, at the Fermi energy, the spin up and spin down electrons are not equally populated. In a magnetic tunneling junction, two ferromagnetic electrodes are separated by a thin insulating layer. Jullière found that the tunneling current depends on the relative orientation of the magnetization direction of the two electrodes. Usually, the tunneling current is larger when the two ferromagnetic electrodes are parallely magnetized. As an early attempt to explain the magnetic tunneling effect, Jullière proposed a model based on the spin polarization of the conduction electrons in both ferromagnetic electrodes. In his model, he assumed that the tunneling probability from any occupied state of one electrode to any unoccupied state in the other electrode is the same and that the tunneling current is

independent of the geometry and the electronic structure of the barrier. Further assumptions are the conservation of the electron spin during the tunneling process, zero temperature (T=0 K), and a small external voltage. Under these conditions, the tunneling current is proportional to product of the density of states of each electrodes: in the parallel case,

$$I_F \propto n_s^\uparrow n_t^\uparrow + n_s^\downarrow n_t^\downarrow \tag{2.5}$$

while in the antiparallel case,

$$I_A \propto n_s^\uparrow n_t^\downarrow + n_s^\uparrow n_t^\downarrow \tag{2.6}$$

Here, the $n_{s(t)}^{\uparrow(\downarrow)}$ are the number of electron states involved in the tunneling process with spin up (spin down) of the sample (tip). Though, many simplifications are included in this model, it leads to a qualitative description of the spin-dependent tunneling process.

A more recent model developed by Slonczewski [39] includes the influence of the tunneling barrier. He analyzed the tunneling current through a rectangular barrier by assuming a free electron model in the two ferromagnetic electrodes and shows that the spin-dependent tunneling current not only depends on the spin polarization of the ferromagnetic electrodes but also strongly correlates to the properties of the tunneling barrier.
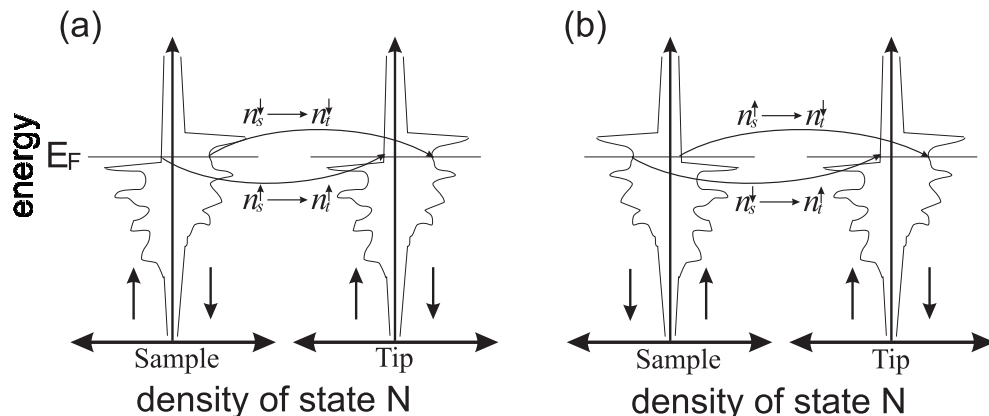

Figure 2.3: Tunneling between two ferromagnetic electrodes (in the spin-polarized scanning tunneling microscopy, these two electrodes can be regarded as sample and tip) that show a split density of states n(↑/↓ indicate majority/minority states). In (a), the magnetization of the two electrodes are parallel. In (b), the magnetization of the two electrodes are antiparallel. The tunneling pathes in both cases are indicated in the image. The detailed explanation can be found in the text.

In the case of Sp-STM, the situation is similar. The insulating layer is replaced by a vacuum barrier which in principle simplifies the tunneling process considerably. In a general treatment, the interaction between the tip and sample such as exchange or dipole interactions are neglected. Thus, the spin-dependent tunneling current

is determined by the electronic structure of the two ferromagnetic electrodes and properties of the tunneling barrier. As shown in Fig. 2.3 (a), when two electrodes are ferromagnetically aligned, electrons tunnel between the minority (majority) states of the sample and the minority (majority) states of the tip. The tunneling current is:

$$I_F = I(n_s^\uparrow \rightarrow n_t^\uparrow) + I(n_s^\downarrow \rightarrow n_t^\downarrow) \tag{2.7}$$

In Fig. 2.3 (b), when two electrodes are antiferromagnetically aligned, electrons tunnel between the minority (majority) states of the sample and the majority (minority) states of the tip. The tunneling current is:

$$I_A = I(n_s^\uparrow \rightarrow n_t^\downarrow) + I(n_s^\downarrow \rightarrow n_t^\uparrow) \tag{2.8}$$

If we look back to the Bardeen's approach [36] in the theory of scanning tunneling microscopy, a more elaborate description of the tunneling current needs to solve the tunnel matrix elements expressed by equation 2.3 for the spin-polarized states of the sample and tip in both parallel and antiparallel cases.

Phenomenologically, the spin-dependent tunneling current is described in terms of the angle θ between the two magnetic axes, and $P_{s(t)}$, the effective spin polarization of the sample (tip) which reflects the imbalance of spin up and spin down electrons at the Fermi level of the sample (tip):

$$I(R, V, \theta) = I_0(1 + P_s P_t cos\theta) \tag{2.9}$$

where

$$cos\theta = \frac{\mathbf{M}_s \cdot \mathbf{M}_t}{|\mathbf{M}_s||\mathbf{M}_t|} \tag{2.10}$$

The tunneling current can be separated into two parts: the spin-independent part (I_0) and the spin-dependent part ($I_p = I_0 P_s P_t cos\theta$). The ratio between them, i.e., $I_0 P_s P_t cos\theta/I_0$, is defined as the spin polarization of the tunneling current.

2.2.3   Spin-polarized scanning tunneling microscopy

As mentioned in the introduction, there are two kinds of spin-polarized STM distinguished mainly by the tip materials. One is using LASER pumped semiconducting GaAs tips. The first successful experiment was done by Alvarado and Renaud in 1992 [17]. After the initial experiment, several groups [40, 41] tried this approach. Due to the difficulty in controlling the tip, this direction had a limited progress in recent years. An alternative approach is using ferromagnetic tips. A preliminary experiment was performed by Johnson and Clark in 1990 [42]. They used a Ni tip in combination with the surface of permalloy. The magnetization direction of the tip was fixed. They observed a modulation of the tunneling current while the magnetization direction of the sample was periodically switched at a frequency well above

the cut-off frequency of the STM feedback circuit. In this early work, it was also realized the Sp-STM experiments should be performed in ultrahigh vacuum (UHV) in order to avoid spin scattering due to adsorbates or oxide interlayers. Different ways in obtaining spin contrast with ferromagnetic (antiferromagnetic) tips were developed. In the following, the differences of these methods are discussed shortly according to a recent paper by Wortmann et al. [43].

The constant current mode

Scanning tunneling microscopy is mostly operated in the constant current mode which means the tunneling current is kept constant by adjusting the vertical position of the tip while the tip scans on the surface. In this case, the contour of the surface electronic structure is mapped which is defined as the "topography". As pointed out in the previous section, when a ferromagnetic tip and sample are in the tunneling condition, the tunneling current can be separated into the spin-independent part $I_0(R, V)$ and spin-dependent part $I_p(R, V, \theta)$ which depends on the tip position R, the bias voltage V and the angle θ between the magnetization direction of the tip and sample. The tip was treated as structureless as in the Tersoff-Hamann model [37, 38] which means the density of states (DOS) is constant. In this case, the constant current STM image is governed by the energy integrated local density of states (LDOS) of the sample surface under the tip which includes both nonmag-
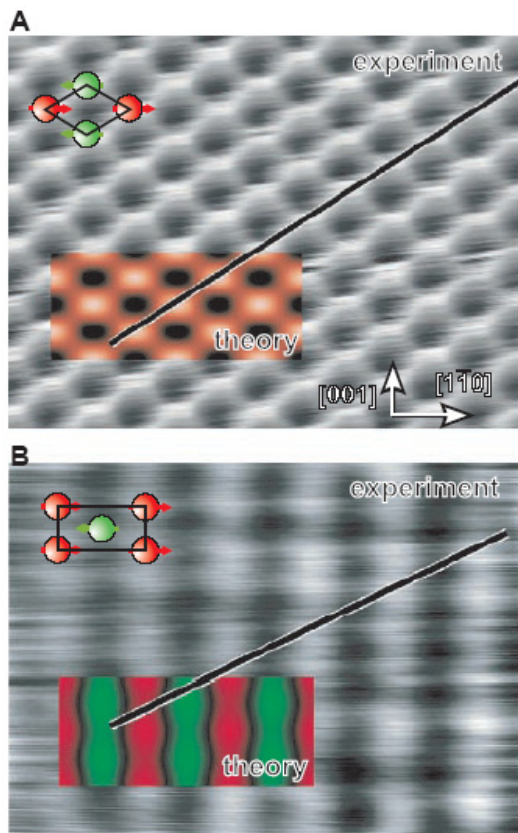

Figure 2.4: Topographic images of Mn monolayer on W(110) taken with (A) a nonmagnetic W tip and (B) a magnetic Fe tip. The image size is 2.7 nm by 2.2 nm [12]

netic and magnetic parts. The nonmagnetic and magnetic contributions are mixed which gives the topography. When the magnetization of the surface is not homogenous, the magnetic influences are observable as additional modulation in the topography. Wiesendanger et al. [44] were the first to use this imaging mode. They investigated the surface of Cr(001) which has a layer-wise antiferromagnetic order, i.e., the magnetization directions of neighboring atomic terraces are opposite. They found that the step height between neighboring terraces alternates between $0.12\,\text{Å}$ and $0.16\,\text{Å}$ when a ferromagnetic CrO_2 tip was used while the step height observed with a W tip is $0.14\,\text{Å}$. The modulation of the step height was attributed to spin-dependent tunneling. The ratio between magnetic and nonmagnetic contribution depends on the spin polarization of the investigated system. Usually, the integrated magnetic LDOS is much smaller than integrated nonmagnetic LDOS. The modulation effect of the topography is not easily visible. High resolution spin images were recorded in this mode in some cases, for example, the two dimensional antiferromagnetic configuration of Mn on W(110) [12] as shown in Fig. 2.4. The stripe lines come from the magnetic contribution. The origin of atomic resolution with a ferromagnetic tip will be discussed later.

The spectroscopic mode

In the spectroscopic mode, the local differential conductivity dI/dV is measured which is proportional to the LDOS. In the experiment, the dI/dV signal is measured by adding to the dc-bias a small ac-bias voltage with an amplitude of a few to a few tens mV. The modulation of the tunneling current due to the change of the bias voltage is extracted by a lock-in amplifier. The signal is proportional to the LDOS in a narrow energy interval $\triangle E$ around $E_F + eV$. In the case of a ferromagnetic tip and sample, the bias voltage can be chosen to maximize the ratio of magnetic
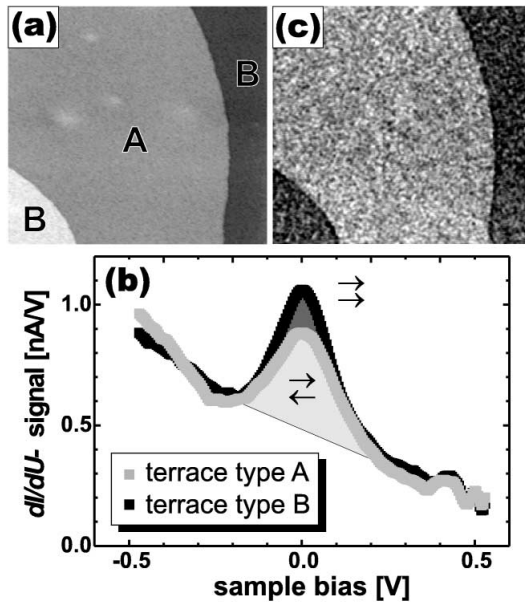

Figure 2.5: (a) Topography of Cr(001) showing three different terraces separated by monoatomic steps; (b) dI/dV curve from two neighboring terraces. (c) Spin-polarized spectroscopic image of the same surface region as shown in (a) using a tunneling current $0.18\,\text{nA}$ and a sample bias -60 mV. The scan size is 500 nm×500 nm. Images are taken from [24]

13

LDOS over nonmagnetic LDOS. The first experiment was done by Bode et al. [45] on Gd(0001) using Fe coated W tips. A recent example [24] is given in Fig. 2.5 of Cr(001) which is a topological antiferromagnets as discussed before. In Fig. 2.5 (b), a clear difference is seen between two neighboring terraces taken with a Fe tip in the dI/dV spectroscopy which means the magnetization direction of one terrace is parallel to the tip while the other terrace is antiparallel to the tip. By choosing an energy where the difference between two cases is maximized, the spin contrast is maximized as shown in Fig. 2.5 (c). Atomic resolution in spin image was also achieved in this mode, for example, in a two dimensional antiferromagnetic Fe monolayer on W(001) [46].

The differential magnetic mode

When the magnetization direction of the tip (or sample) is switched periodically, the tunneling current changes at the same frequency due to the tunneling magnetoresistance effect [15]. The change of the tunneling current upon the reversal of the magnetization is defined as the differential magnetic conductivity. This mode was first proposed by Pierce [16]. Later on, it was tried by Johnson and Clark [42] as already mentioned before. In their experiment, the magnetization of the sample was switched periodically. In this case, they did not manage to scan the tip on the surface because of magnetostriction. The first successful Sp-STM experiment operating in differential magnetic mode by switching the magnetization direction of the tip was done by Wulfhekle et al. [48]. Since the modulation frequency of the tip magnetization is much higher than the cut-off frequency of the STM feedback loop, the STM only sees the average tunneling current which is free of spin information, as will be discussed in Chapter 3.3. The change of the tunneling cur-
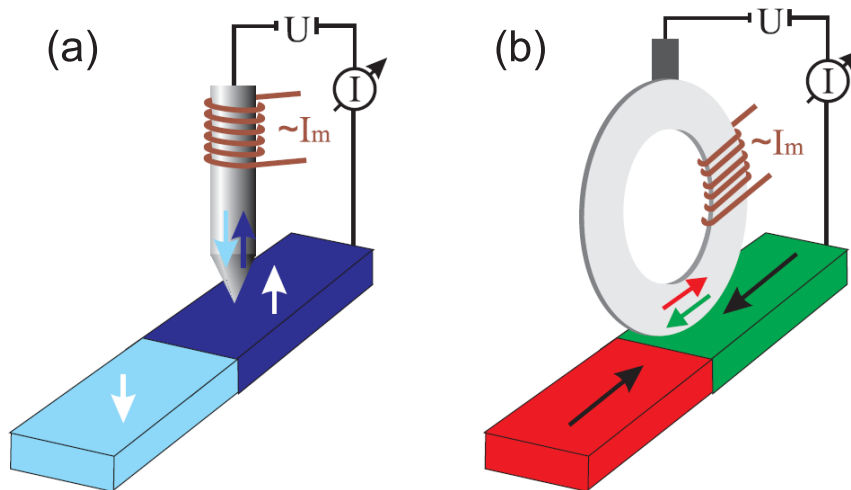

Figure 2.6: Schematic representation of Sp-STM electrodes for measuring a) the out-of-plane and b) the in-plane component [47].

rent due to the switching of tip magnetization is extracted with a phase sensitive lock-in amplifier which gives the spin information of the surface. In this case, the measured spin signal is proportional to the magnetic part of the integrated LDOS according to Wortmann et al. [43]. Thus, a complete separation of the nonmagnetic and magnetic contributions is achieved. The detailed setup and operation principles of Sp-STM operating in the differential magnetic mode will be discussed in the next Chapter. Depending on the system investigated, two different tip constructions were developed as shown in Fig. 2.6. One uses a ferromagnetic needle to measure the out-of-plane component [48]. The other uses a ferromagnetic ring to measure a well defined in-plane component [49].

All these three operation modes of Sp-STM have their advantages and drawbacks. The constant current mode is easy to operate. It does not need any modulation of the STM electric circuit. Compared to normal STM, only a replacement of the non-magnetic tip with a magnetic tip is necessary. The disadvantage is that the spin information cannot be separated from the topography in all cases. The image is a mixture of the magnetic and nonmagnetic LDOS which makes the extract of the spin information difficult. The spectroscopic mode can neither separate the nonmagnetic and magnetic contribution completely. However, one can choose a certain DC-bias voltage where the ratio of the magnetic LDOS over the nonmagentic LDOS is maximized to obtain better spin contrast. Both in the constant current mode and spectroscopic mode, nonmagnetic tips coated with ferromagnetic (antiferromagnetic) materials [50, 46] or bulk antiferromagnetic tips [51] were used. They give much smaller stray field comparing to bulk ferromagnetic tips. Especially, in the case of an antiferromagnetic tip, the stray field is completely diminished. This is important when imaging soft magnetic thin films. In the differential magnetic mode, bulk ferromagnetic tips were used. The advantage of this mode is that the topography and spin signal are well separated. The stray field can be reduced by choosing a proper geometry of the tip. The magnetization direction of the tip can also be precisely defined by the shape of the tip, either perpendicular or parallel to the sample surface. In the constant current and spectroscopic modes, the magnetization direction of the tip can be changed between in-plane and out-of-plane, but the in-plane magnetization direction of the tip is arbitrary. A well defined in-plane magnetization direction of the tip is important when imaging noncollinear antiferromagnetic spin structures. Wortmann et al. [43] predicted that the same spin structure can show very different patterns when mapped with differently oriented magnetic tips.

2.2.4   Resolution in STM and Sp-STM

In the ideal spin-polarized scanning tunneling microscope, atomic resolution should be recorded simultaneously in both topographic and spin channel. Thus, a direct comparison of structure and spin configuration can be done. Atomic resolution in the spin channel has been achieved on different surfaces with different tip materials

15

in both constant current mode [12, 51, 52] and spectroscopic mode [46], but to our knowledge, no experiment has shown atomic resolution in both structure and spin simultaneously. In the following, the origin of atomic resolution in topography and spin and the relation between them will be discussed.

First, from the tip side of view, in the Tersoff-Hamann approach, the tip is modeled as a macroscopic continuum of s-wave symmetry. The center of curvature of the tip follows the contour of the LDOS at the Fermi edge in the low bias limit. Within Tersoff-Hamann scheme, the surface corrugation decreases exponentially both with the tip radius and the tip-surface distance. The spatial variation of the surface electron density of close packed metal surfaces at the position of the tip, i.e, 5-10 Å above the surface is extremely weak. Thus, only superstructures with periodicity larger than $\sim$6 Å can be resolved. The atomic corrugation for most metal surfaces within the Tersoff-Hamann model is very small, a few pm or even less. While experimentally, individual atoms are resolved on almost every metal surface with a corrugation in the ten pm range [54, 55]. Nowadays, it is generally accepted that d states tip must be considered in order to explain the large corrugation. This was
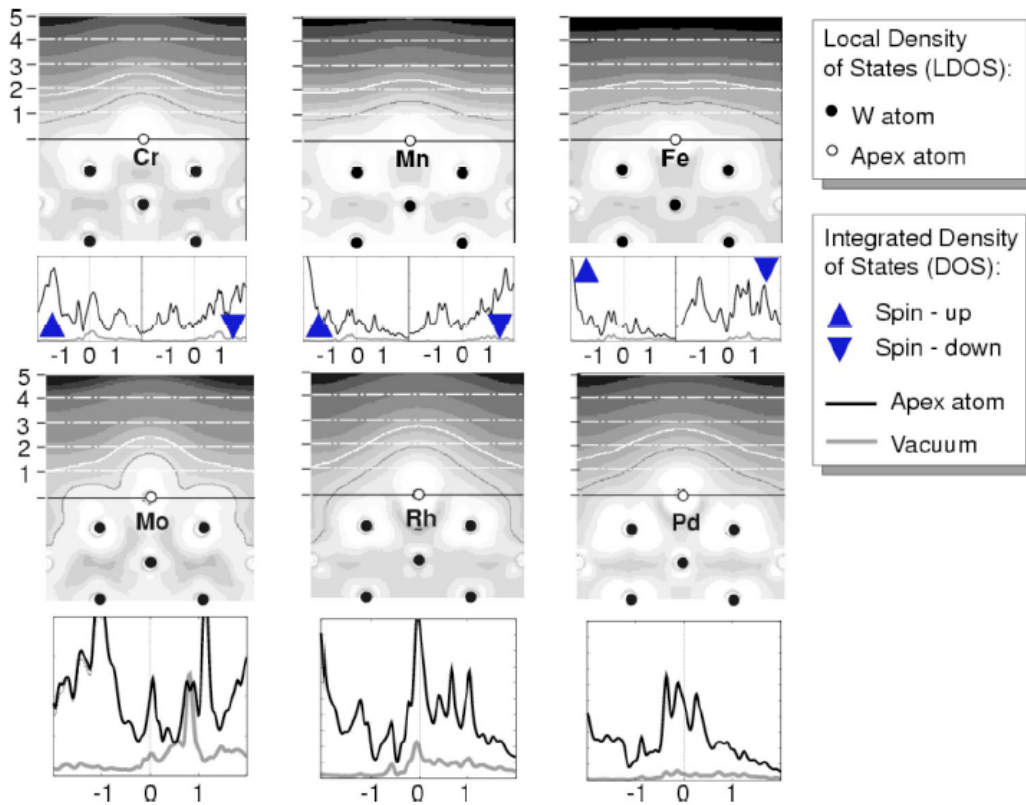

Figure 2.7: Local density of states and integrated density of states of selected magnetic and nonmagnetic scanning tunneling microscope (STM) tip models. The tip is mimicked by a W(100) surface with single 3d and 4d impurities. Image taken from [53].

first proposed by Chen [56] in 1990. He calculated the d_{z^2} tip states in terms of the commonly used tip materials, W, Pt and Ir and gave much lager corrugation height. Thus, the resolving of single atoms depends on the tip materials and tip states. In the Sp-STM, 3d transition metals are used as tip materials. Hofer et al. [57, 58] analyzed the differences of different material ended tips for 3d, 4d and 5d transition metals by calculating the electronic states in real space of one absorbed atom on W(100) as the tip apex. He showed the protrusion of single electron states into the vacuum which qualitatively reflect the sharpness of the tip end. The general tendency he found is that 4d tips are shaper than 3d tips as shown in Fig. 2.7. The 5d tip are even sharper [58]. The calculation is consistent with the fact that atomic resolved images are usually recorded with W or PtIr tips. Thus, the usage of 3d transition metals as the tip materials reduces the resolution intrinsically.

Second, from the sample point of view, the presence of in-plane antiferromagnetic coupling of surface atoms gives larger unit cells. For example, on a two dimensional antiferromagnetic surface, as shown in Fig. 2.8, the spin unit cell is double of the
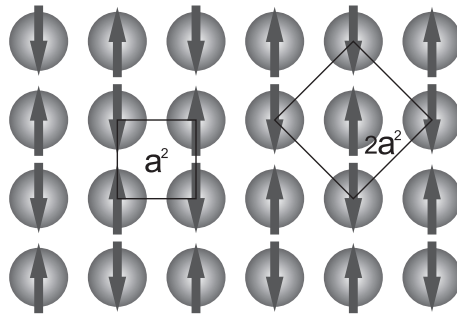

Figure 2.8: Top view of a two dimensional antiferromagnetic surface. The magnetic moments of nearest neighbor atoms are antiparallel. The size of the structural unit cell is a^2 while the spin unit cell is $2a^2$.

structural unit cell. This makes the resolving of spin relatively easier though the spin signal is usually quite small. Considering the antiferromagnetic surface as described in Fig. 2.8, at the position of the surface atoms, whether the corrugation of the total charge density is larger or smaller than the corrugation of spin-dependent electronic density is determined by the spin polarization of the surface charge density. Only when the spin polarization is larger than 50%, the spin corrugation is larger than the total charge corrugation. However, as already discussed before, in the simple Tersoff-Hamann picture, the tunneling current is determined by the local density of states at the tip position which is about 4-10 Å above the surface. Thus, a proper description of the density of the states in the region above the surface is very important. Heinze [50] described the surface using the full-potential linearized augmented plane wave (FLAPW) method which is a two-dimensional(2D) method consisting of a semi-infinite vacuum region. The vacuum wave function is expanded

into basis functions

$$\psi_{\mathbf{k}_\parallel \nu}(\mathbf{r}_\parallel, z) = \sum_n c^n_{\mathbf{k}_\parallel} d^n_{\mathbf{k}_\parallel}(z) e^{i(\mathbf{k}_\parallel + \mathbf{G}^n_\parallel)\mathbf{r}_\parallel} \qquad (2.11)$$

which are 2D plane waves parallel to the surface. Here, $\mathbf{k}_\parallel$ is the wave vector, $\mathbf{G}^n_\parallel$ is the reciprocal lattice vector and $c^n_{\mathbf{k}_\parallel}$ is a constant. The linearized z-dependent basis function can be simplified following the assumption of Sacks [59] by approximating the z-dependent part by its simplified tail. Then, the vacuum wave function of energy ϵ will decay inside the barrier as

$$d^n_{\mathbf{k}_\parallel}(z) = e^{-z\sqrt{2m|\epsilon|/\hbar^2 + (\mathbf{k}_\parallel + \mathbf{G}^n_\parallel)^2}} \qquad (2.12)$$

we can see the wave function with small periodicity decays much faster than the one with large periodicity. This explains why the reconstructed surface is much easier to resolve whether these reconstruction has chemical or structural origin. Any magnetic superstructure lowers the translational symmetry as well. Thus, the spin-dependent part of the work function decays much slower into the vacuum which means even at the position of the surface atoms, the spin corrugation is small, at the STM tip position, the spin corrugation is more significant than the structural corrugation.

Comparing the three operation modes of the Sp-STM, the spin signal is either proportional to the spin-dependent LDOS at a certain energy window, or integrated LDOS. These two have the same translational symmetry. From this point of view, there are no differences between the three operation modes of Sp-STM. In the constant current mode, the image is dominated by the magnetic contribution, especially when the surface magnetic unit cell is much larger than the atomic distances, such in as on the surface of some compounds like $Fe_3O_4(111)$ [51] and $Mn_3N_2(010)$ [52]. Because of the mixture of the topography and spin signal, a high resolution in spin means that the atomic corrugation is shielded. In the spectroscopic mode, though the topography and the spin signal can be recorded at the same time, the atomic resolution in both channel was not achieved. Since in this case, the tip is magnetized in one direction, it is not much different from the constant current mode. The topographic image still contains a spin contribution. In the differential magnetic mode, the tip magnetization is switched at a frequency much higher than the cut-off frequency of the feedback loop. The topographic image contains no magnetic information. An atomically resolved topography was not achieved at the same time when the atomic resolution in spin was achieved. The separation of magnetic and nonmagnetic density of states enhance the corrugation in the spin channel. This is an unique advantage of Sp-STM operating in the differential magnetic mode. We, however, found that a high resolution in spin often means the loss of atomic resolution in topography. It is not known in the spin-dependent vacuum tunneling which bands dominate the tunneling process, s-,p- or d-bands. The resolution on close packed metal surface is determined by the tip states. It is possible that a highly

spin-polarized tip state is in general conflicting with a sharp tip state. It is consistent with the calculation of Hofer [57, 58], that a spin-polarized tip with a 3-d transition metal is not as sharp as a nonmagnetic 4-d and 5-d transition metal tip.

As a short conclusion, it is clarified with above discussion that the spin-dependent wave function decays slower that spin-independent wave function which makes the spin easier to resolve atomically.

.

3. Experimental details

3.1 Ultrahigh vacuum system and surface analysis tools

The experiments were performed under ultrahigh vacuum (UHV) conditions. The base pressure of the UHV chamber was better than 1×10^{-10} mbar. The chamber is divided into two parts as sketched in Fig. 3.1: an in-situ sample preparation and characterization chamber and a scanning tunneling microscopy (STM) chamber. The sample is transferred between the two chambers via a small wagon sitting on a rail. A two-stage load lock system ensures the change of substrates or STM scanners within three hours without breaking the vacuum of the main chamber. The whole UHV system was placed on pneumatic suspension legs to damp mechanical vibration for STM measurements. Auger electron spectroscopy (AES) and low energy electron diffraction (LEED) were installed in the preparation chamber. The AES electron gun and the LEED fluorescence screen were arranged opposite to each other. In this configuration, medium energy electron diffraction (MEED) can be done which was used to monitor the growth process. In the following, these tools are described briefly.

Auger electron spectroscopy

AES is a well established technique used for elemental analysis of surfaces [60]. The name is derived from the effect first observed by P. Auger in the mid-1920's [61]. Auger electrons are emitted from atoms during relaxation of the core level holes. The energy of Auger electrons are determined by the electronic structure of the elements which is unique for each element so that the Auger electrons give the fingerprints of all the elements except H and He. It offers a high sensibility (typically ca. 0.01 monolayer). In our experiments, AES was used to check the cleanness of the samples.

Low energy electron diffraction

The wave nature of electrons is used to perform diffraction experiments of solids. There are two factors which make the low energy electrons (typically from ten to a few hundred eV) surface sensitive. First, the mean free path of low energy electrons in solids is short (around 5 to 10 Å). Only the electrons scattered from the near surface can leave the surface. Second, the electron's de Broglie wavelength (the wavelength of 100 eV electron is 1.22 Å) fits very well with the typical distance be-
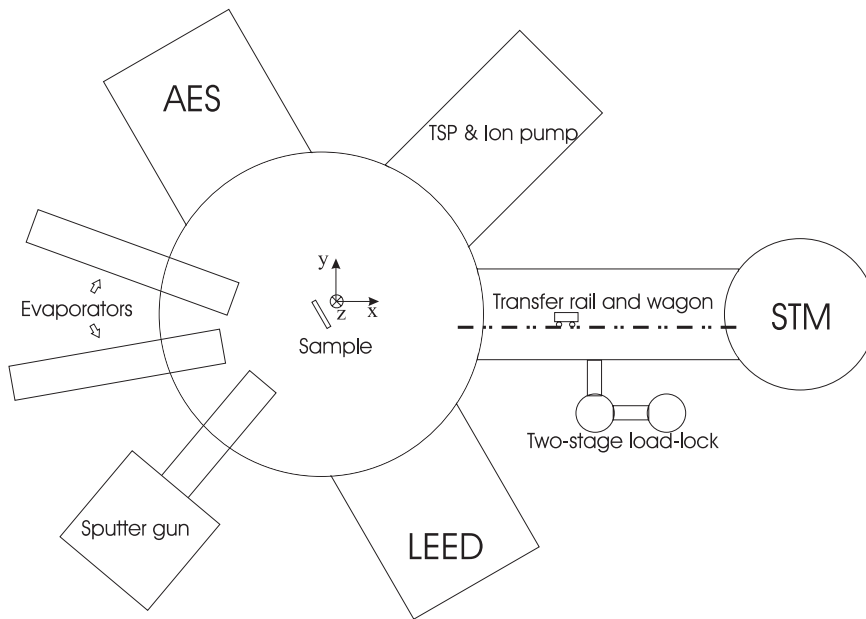
Figure 3.1: Schematic representation (top view) of the UHV chamber equipped with AES, LEED and STM. The coordinates show three of five moveable dimensions of the manipulator. The other two are the rotation around z-axis and the rotation around the normal axis of the sample surface.

tween atoms in crystals and thus diffraction phenomena are expected. There are two major operation modes for LEED. In the first mode, the surface diffraction pattern is inspected which can quickly give information about the surface symmetry and periodicity. The second application of LEED is to determine the crystal structure quantitatively, i.e., to determine the positions of the atoms in the surface plane as well as perpendicular to the surface. For this purpose, one needs to measure the intensity of the diffraction spots as a function of the incident electron energy, so called LEED I-V curves. The intensity and peak positions in the I-V curve reflect the diffraction -constructive or destructive- which is determined by the lateral as well as the normal positions of the atoms within the electron's penetration depth. The positions of the atoms can be determined by fitting the LEED I-V curve with multiple scattering calculations. In the simulation of the I-V curve, a structural model is built first with different scattering potentials for different elements. This model structure needs to be modified during the simulation until a good agreement between calculated and experimental curves is achieved. The degree of the agreement is quantified by a the reliability factor (R-factor). The lower the R-factor, the better the agreement. A comprehensive overview of LEED can be found in ref. [62, 63].

Medium energy electron diffraction

MEED is similar to the better-known RHEED (Reflection High-Energy Electron Diffraction) [64], except for the lower energy of the incident electron beam, typi-

cally in the range 2-5 keV. Its usage is also similar: due to the high energy of the electrons, grazing incidence is used to minimize the penetration depth of the electrons into the sample and enhance the surface sensitivity. If the surface is atomically flat, the MEED pattern is sharp and bright. If the surface is rough, the MEED pattern is more diffuse. This behavior can lead to oscillations of the spot intensity as the film grows in layer-by-layer mode. Therefore, MEED can be used to characterize the growth mode. MEED oscillations give the information such as growth rate and film thickness with high accuracy.

3.2 Substrates and sample preparation

Two different substrates were used in our experiments: Fe whiskers and Cu(001) single crystals. The substrates were mounted on a temperature variable sample holder which is connected to a manipulator with 5 dimensional freedom as shown in Fig. 3.1. The 5 dimensions are x, y, z, the rotation around z axis and the rotation around the normal axis of the substrate surface which enable the access of AES, LEED and MEED.

Fe whiskers are grown from the vapor phase and have a needle-like shape with a rectangular cross section of a width of a few hundred μm and a length of 1 to 2 cm [1]. Fe whiskers have nearly perfectly flat surfaces with terraces of several hundred nm in width. Fe whiskers also contain much less contaminations such as C or S compared to Fe crystal grown from the melt. Another reason for choosing Fe whiskers is that they have a simple magnetic structure. We will come back to this point again later in this Chapter. Fe whiskers were cleaned by cycles of Ar^+ ion sputtering and annealing to 720 K. Between the cycling, the substrate was checked with AES and LEED until a clean, flat and well ordered surface was achieved.

The Cu(001) substrate was cut from a Czochralski grown single crystal with a miscut angle less than $0.2°$. The substrate has a disk shape with a diameter of 6 mm and a thickness of 2 mm. The cleaning procedure of Cu(001) is similar to Fe whiskers, except that the annealing temperature is higher (about 770K).

The materials deposited on the substrates were evaporated from electron beam heating evaporators. The electrons emitted from a heated tungsten filament are accelerated in a concentric electrostatic field to the growth material, which is held at a high positive potential (around 1 KeV). The growth material is heated up to evaporation condition. The vapor is partially ionized which can be detected by a flux monitor, which gives a direct measurement of the evaporation rate. A detailed description can be found in [65]. Rod shaped materials with a diameter of 2 mm were used for Fe, Co and Ni. Manganese flakes were used instead of a Mn rod because nitrogen was often used in the fabrication of Mn rods forming manganese nitride. The nitrogen was released in the vacuum when Mn rods were heated up leading to a bad

pressure during deposition. With Mn flakes, no significant amount of nitrogen was observed. The growth procedure was monitored with MEED. The detail of MEED oscillations will be discussed in Chapter 4 and 5.

3.3 Spin-polarized STM setup

A commercially available Omicron room temperature micro-STM was adopted in our Sp-STM setup. In this kind of STM, vibration isolation is achieved by a non-magnetic setup, i.e., by viton O-rings which ensure a vanishing of the magnetic field near the tip. As discussed in Chapter 2, the working distance between the STM tip and sample surface is about a few angstroms. Thus, it is crucial to keep or adjust the distance between the tip and sample with sub-angstrom precision during scanning. Technically, this is realized by the piezo-electric element to which the STM tip is attached. Piezoelectric materials have the useful property that they change their length slightly when exposed to an electric field. By adjusting the voltage on the z piezo element, the distance between the tip and the surface can be regulated. In most
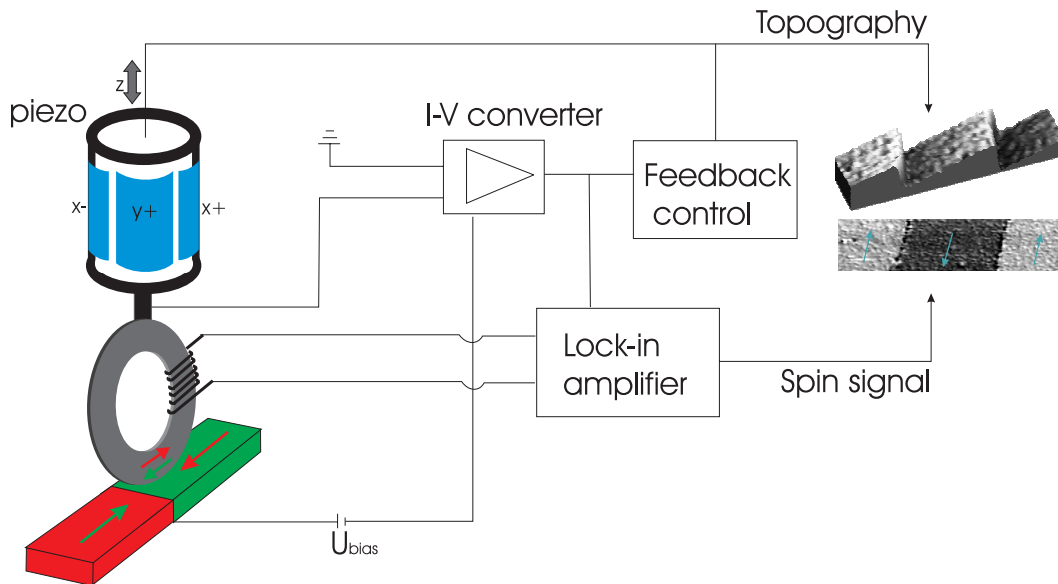

Figure 3.2: Electric circuit of the Sp-STM together with a tube geometry of the piezo. The bias voltage is applied between the ring and the sample. The tunneling current is analyzed in two routes after the I-V convertor. In one route, it goes into a feedback control system which then adjusts the voltage applied to the z piezo and gives the topography. In the other route, the tunneling current goes into a lock-in amplifier which also supplies a sinusoidal current to the coil wound around the ring to switch the magnetization direction of the ring periodically. The variation of the tunneling current due to the magnetic switching of the ring electrode is extracted by the lock-in amplifier which gives the spin information of the surface.

STMs, the voltage on the piezo element is adjusted such that the tunneling current always has the same value, for example 1 nA. This distance regulation is performed by the feedback electronics as sketched in Fig. 3.2, which continuously measure the deviation of the tunneling current from the desired value and retracts the tip when the current is too high or advances it when the current is too low. While this feedback system is active, two other parts of the piezo element are used to move the tip in the X- and Y-directions, parallel to the surface, to scan over the surface, line by line, similar to the way a television image is built up. In most modern scanning probe microscopes, a tube geometry is adopted as shown in Fig. 3.2. Each of the four indicated sections (X+, X-, Y+, Y-) can be adjusted individually. If all four sections are altered by the same amount, the tip moves in the z-direction. If the X+ side is made longer, and at the same time the X- side is made shorter by the same amount, the tube bends a little bit. For small deformation, the tip moves primarily in the X-direction. The same can be done in the Y-direction. Figure 3.3 (a) gives a photo of a real scanner with a tube geometry.

To realize spin-polarized measurements, additional circuits were added to the usual STM circuits as shown in Fig. 3.2. The normal tip is replaced by a magnetic ring with a coil wound around it. Two additional pins served as connectors for the coil were attached to the scanner as shown in Fig. 3.3 (a). The magnetization direction of the ring was changed periodically by applying an alternating current to the coil. The driving current is generated by the lock-in amplifier with a frequency between 20 and 40 KHz, which is well above the cut-off frequency of the STM feedback loop. Thus, the feedback cannot "see" the change of the tunneling current due to the switching of the magnetization direction of the ring, which then gives the topographic information correctly as already discussed in Chapter 2. The modulation of
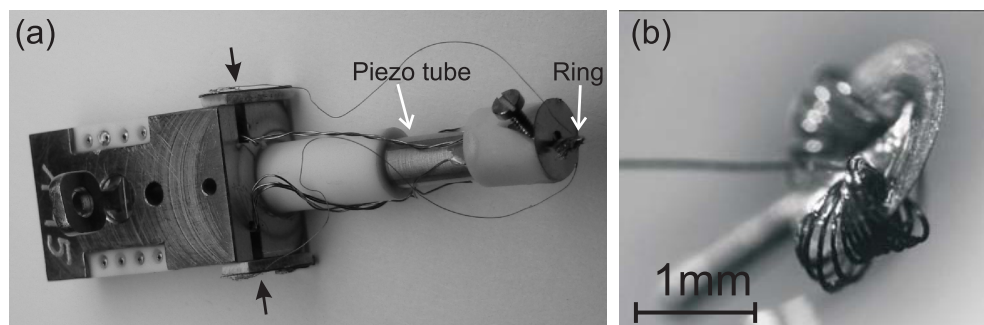

Figure 3.3: (a) Scanner of the Omicron micro-STM. The piezo tube is connected to a holder where the pins for electric contacts are comprised. The ring is fixed to the piezo tube with a screw. Two additional pins (marked with black arrows) were added to the scanner where the two ends of a copper wire from the coil on the ring are attached to. (b) Picture of the ring with coil wound around it. The ring is attached to a 300μm thick Ta wire with silver paste. The Ta wire is then inserted to a hole at the end of the scanner and fixed with a screw as shown in (a). Picture (b) was taken from [49].

the tunneling current due to the switching of the magnetization of the ring electrode is extracted by a phase sensitive lock-in amplifier which gives the spin signal. This process is sketched in Fig. 3.4. The current for the coil from the lock-in amplifier is a sinusoidal signal. From the magnetic switching behavior of the ring measured by magneto-optical Kerr effect (MOKE) [49], it is expected that the change of magnetization of the ring obeys a square wave shape. The tunneling current depends on the spin polarization of the ring (P_T) and sample (P_S) and the relative orientation between their magnetization directions. The angle between the magnetization direction of the tip and the sample is θ. The tunneling current can be written as:

$$I_{\uparrow\uparrow} = I_0(1 + P_T P_S cos\theta) \tag{3.1}$$

When the magnetization direction of the tip is switched to the opposition direction, the tunneling current is changed:

$$I_{\uparrow\downarrow} = I_0(1 - P_T P_S cos\theta) \tag{3.2}$$

Thus, the average current, i.e., the DC component, which is totally spin independent gives the topography of the surface.

$$I = (I_{\uparrow\uparrow} + I_{\uparrow\downarrow})/2 = I_0 \tag{3.3}$$

The difference of the tunneling current between these two states gives pure spin information.

$$\Delta I = I_{\uparrow\uparrow} - I_{\uparrow\downarrow} = 2I_0 P_T P_S cos\theta \tag{3.4}$$

In the experiment, I_0 is kept constant and P_T can also be treated as a fixed value, so that the spin signal ΔI is proportional the projection of the spin polarization of
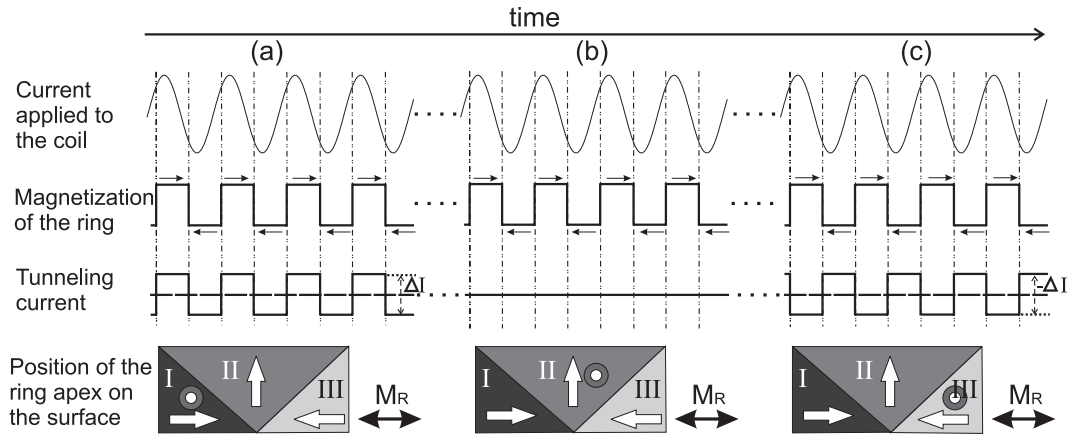

Figure 3.4: Schematic explanation of the spin contrast while the ring scans on a magnetic surface with domains. The white arrows in the bottom images give the magnetization direction in the domains. The position of the ring at different time is also indicated. M_R gives the magnetization direction of the ring. A detail description of the spin contrast can be found in the text.

the surface on the ring direction, which is $P_S cos\theta$. This procedure can be described by Fig. 3.4. The magnetization of the ring is set perpendicular to the magnetization of the region II. When the ring scanned from region I to III, region I and III have opposite magnetic moments, so they give opposite spin signal. While in region II, the projection of the magnetic moments on the ring direction is zero, which means that ΔI equals zero. This gives the contrast observed in the spin image, black, gray, and white with a phase sensitive lock-in amplifier. In this way, the relative spin polarization of the surface along the ring direction can be measured.

3.4 Preparation of the scanning electrodes: tip and ring

Preparation of tungsten tips

As has been mentioned in Chapter 2, the resolution of STM depends on the tip material. The atomically resolved topographic images in this thesis were recorded with tungsten tips. The W tips were electrochemically etched which was known
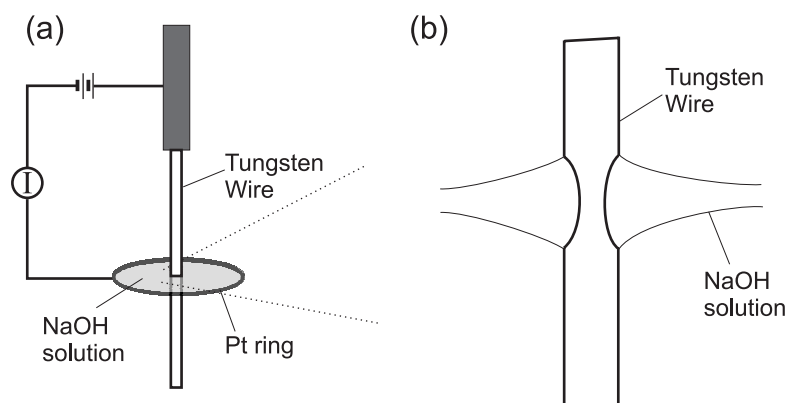

Figure 3.5: A simple sketch for etching a W tip. The detail description can be find in the text.

to form sharp tips [66]. The setup is shown in Fig. 3.5. A Pt ring sustained a membrane of 5% NaOH solution inside. The Pt ring was kept in horizontal position to obtain a homogeneous membrane. A W wire with a diameter of 380 μm was inserted through the membrane in the center. A DC current was applied between the W wire and Pt ring with W as the anode and Pt as the cathode. The etching current was 60 mA at the beginning and was reduced to 10 mA at the end to reduce the etching rate which was helpful to form sharp tips. Due to the surface tension of the liquid, at the position where the tungsten wire and the NaOH solution was in contact, the membrane extended along the W wire to both sides as shown in the enlarged description in Fig. 3.5 (b). The current density in this contact area was not

homogeneous which resulted in a concave curvature around the W wire and finally a sharp tip was formed. During the etching process, the membrane might break for a few times. To reform the membrane, the Pt ring was put into the NaOH solution and then taken out. The important thing in this procedure was to keep the membrane at the same position of the W wire. Finally, the bottom part of the tip was dropped into pure water which stopped etching immediately and the remaining NaOH solution on the wire was washed away. We use the bottom part in our STM measurements. Usually, after two hours Ar^+ ion sputtering at 2 KeV to remove the oxidized layer, atomic resolution was achieved.

Preparation of the rings

Special care was taken when choosing the material for the ring electrode. We used an amorphous alloy of $Co_{68.15}Fe_{4.35}Si_{12.5}B_{15}$. This is a soft magnetic material with almost vanishing magnetostriction $(< 4 \times 10^{-8})$ which ensures a constant distance during the switching of the magnetization of the ring. The material also has a very low intrinsic coercivity smaller than 10 μT. The low coercivity ensures a rapid switching of the magnetization of the ring without mechanical vibrations.
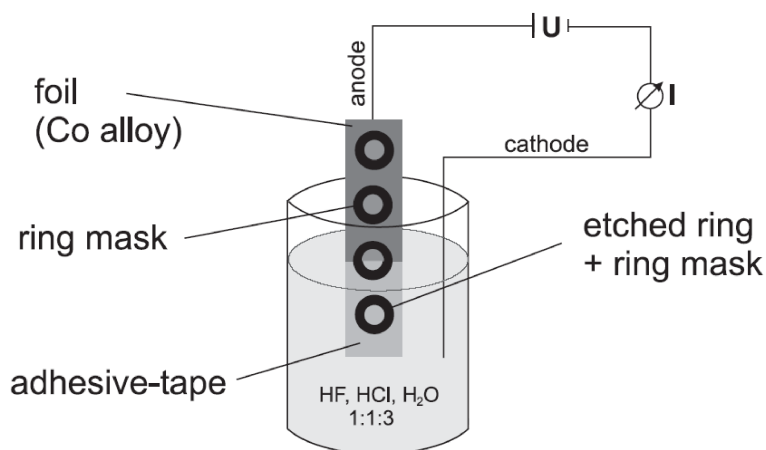

Figure 3.6: A sketch for etching a ring [47]. The detailed description can be found in the text.

The rings used in the Sp-STM were electrochemically etched from a foil of 25 μm thickness. To etch the rings, we glued non-conductive masks on one side of the CoFeSiB foil. These masks had an outer diameter of 2 mm and an inner diameter of 0.7 mm. On the other side of the foil, adhesive-tape was fixed. A scheme of this preparation setup is shown in Fig. 3.6. The etching solution was a mixture of HF (40%), HCl (32%) and H_2O. The cathode is a Pt wire and the anode is the CoFeSiB foil. By applying a voltage between these two electrodes, the foil exposed to the solution was etched away and the area covered with the masks remained. During the etching process, a current of 40-60 mA was applied. After etching, the masks

and the adhesive-tape were removed with ethanol. The etching procedure alone produces some irregular structures at the outer and inner perimeter of the rings. To reduce the roughness, the inner perimeter was polished with a fine raper. The outer perimeter of the rings where the tunneling happens was first polished with sandpaper of a grain size of 10 μm for 5 minutes, afterwards with a diamond paste, 10 minutes with a grain size of 6 μm, 10 minutes with a grain size of 1 μm and 5 minutes with a grain size of 0.25 μm. After these steps, the rings were annealed in H_2 atmosphere to 513 K for 3 h. The ring material cannot be annealed to higher temperatures, because it crystalizes and becomes hard magnetic. Finally, a small coil of an enameled copper wire with a diameter of 50 μm was wound around the ring. To connect the ring to the STM scanner, a Ta wire was fixed to the ring with conductive silver paste. The ring is finally done at this point. A picture of the ring is shown in Fig. 3.3 (b). After the ring was introduced into the UHV, in-situ cleaning and improvement of the ring electrode was carried out. For that purpose, a sputter gun and an Fe evaporator were mounted around the STM scanner. Before every scanning, the ring was first cleaned by Ar^+ ion sputtering and then a few monolayers of Fe were deposited on the ring. This procedure was found to increase the chance to obtain high spin contrast.

3.5 Test of the ring: antiferromagnetic Mn films on Fe(001)

In general, a ring can survive for 3 to 6 months until the insulating layer of the coil was sputtered away resulting in a leak current into the tunneling current. It is essential to make sure at the very beginning whether the ring works properly or not. Since the apex of the ring cannot be chosen or modified in a controlled way, one cannot really tell if a ring is good or not. The best way to check the ring is to scan on a magnetic surface to obtain the spin contrast.

For this purpose, a proper model system needs to be chosen. It is known from the discussion of the previous section that first, the system should have well defined magnetization direction which is parallel to the ring. Second, the lateral size where spin contrast can be observed should not be too large or too small so that it is suitable for STM observation. The well studied Mn/Fe(001) system is adopted in our case. Mn thin films on Fe(001) were studied by many groups as well as in our own lab [23]. Mn grows pseudomorphically on Fe(001) and forms a body centered tetragonal (bct) structure. It is already well established that for Mn thickness above two monolayers, the film has a Type I antiferromagnetic structure as sketched in Fig. 2.1 (a) with the magnetization directions of the Mn either parallel or antiparallel to the magnetization direction of the underlying Fe. Thus, on the surface, neighboring Mn terraces have opposite magnetization direction as shown in Fig. 3.7 (d). Fe
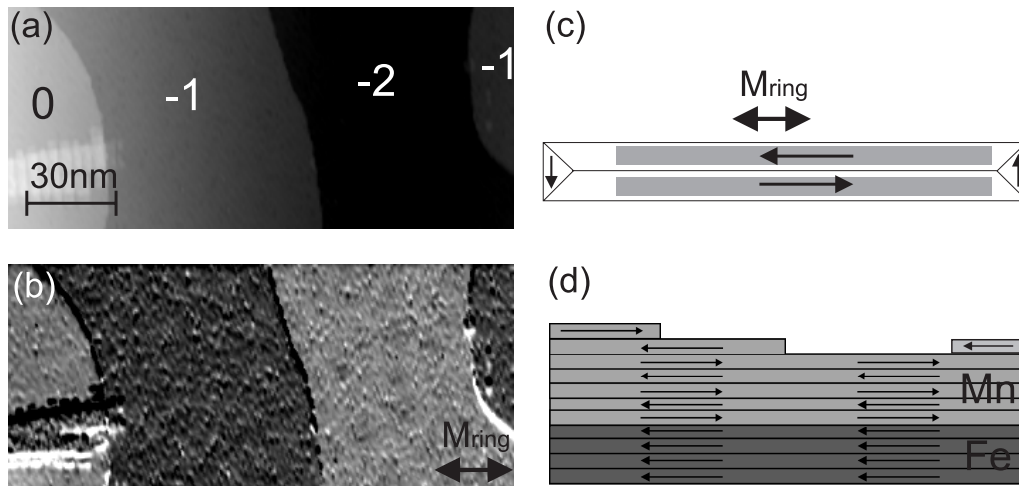
Figure 3.7: Test of the ring on 6 ML Mn thin films deposited on Fe whisker. (a) and (b) are the topography and corresponding spin signal. 0, -1 and -2 in (a) show three atomic layers from the most top one to the layers below. (c) sketches the domain structure of Fe whisker and the geometry between the ring and the Fe whisker while scanning. The shadowed area are the position where measurements were carried out. (d) explains the origin of spin contrast between neighboring layers on the surface arising from the Mn thin films.

whisker was chosen as the substrate because it has a simple magnetic domain structure. Typically, the domain pattern consists of a so called Landau structure, where a 180° domain wall runs parallel to the long axis of the Fe whisker and the magnetic flux was closed at both ends of the whisker by forming 90° domain walls as shown in Fig. 3.7 (c). This domain structure has been observed with scanning electron microscopy with polarization analysis (SEMPA) [67] and Kerr-microscopy [1]. In our experiments, the ring was aligned parallel to the long axis of the whisker and sat on the long shape domain where the magnetization direction is in the ring plane as indicated by the shadowed area in Fig. 3.7 (c). The terrace sizes were typically around several ten nm which was suitable for STM observation. Figure 3.7 (a) and (b) gives the topography and corresponding spin images. On the surface, three successive atomic layers (marked as 0,-1,-2) were exposed as indicated in Fig. 3.7 (a). In the spin image, we can see that layer 0 and -2 are brighter than layer -1 which is consistent with the model shown in Fig. 3.7 (d). The spin polarization of the tunneling current which is defined as $\Delta I / I$ can be calculated. The typical value we obtained was around 3%. From the spin image and the polarization of the tunneling current, it can be judged if the ring was working properly or not. The well defined in-plane magnetization of Mn films by the underlying Fe whisker also allows to confirm the the magnetic sensitive direction of the ring. We never obtained similar spin contrast as shown in Fig. 3.7 (b) while the ring was perpendicular to the long edge of the Fe whisker. This means the magnetization direction of the apex atoms is restricted in the ring plane by the shape anisotropy. The well defined in-plane di-

rection of spin sensitivity allows the mapping of noncollinear spin structure as will be demonstrated in the following Chapters.

.

4. Structure and magnetic properties of reconstructed Mn on Fe(001)

4.1 Manganese: from bulk to thin films

Manganese has the most complex structural and magnetic properties among all elements. Unlike other magnetic transition metals which crystallize in cubic or hexagonal structures such as face centered cubic (fcc) Ni, body centered cubic (bcc) Fe and hexagonal close-packed (hcp) Co, Mn shows different structural phases and accompanied magnetic behaviors at various ambient conditions.

The stable bulk phase of Mn under room temperature is α-Mn which has a cubic structure containing 58 atoms per unit cell [30] as shown in Fig. 4.1. The lattice
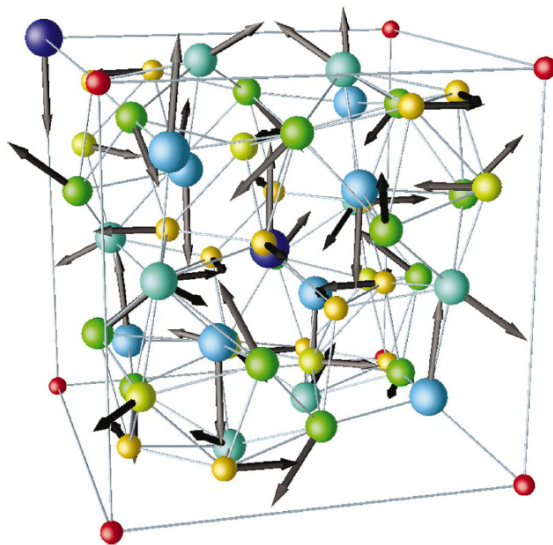
Figure 4.1: Crystalline and magnetic structure of antiferromagnetic α-Mn. Atomic positions in the full cubic tetragonal unit cell and magnitude and directions of the magnetic moments are shown. Atoms on crystallographically inequivalent sites are marked by different colors: dark blue: MnI, light blue: MnII, green and turquoise: MnIII (a) and (b), yellow and yellow-green: MnIV (a) and (b). The calculated magnetic structure is indicated by the arrows. The magnetic moment on the MnI site has been aligned parallel to the [001] direction. The picture is taken from Ref. [68].

constant of paramagnetic α-Mn is 8.865 Å [18]. The 58 atoms can be divided into four crystallographically inequivalent sites [30] which are labeled as MnI, MnII, MnIII and MnIV as shown in Fig. 4.1. α-Mn shows antiferromagnetism below the Néel temperature of 95K [69]. A tetragonal distortion with the lattice constants of $a = b = 8.877$ Å and $c = 8.873$ Å [19] accompanies the magnetic transition.

The magnetic structure is antibody-centered which leads to the increase of inequivalent sites to 6 [19]. The structure and magnetism of α-Mn were intensively studied by both experimentalists [18, 19, 20, 21] and theoreticians [68, 70]. Different techniques such as neutron diffraction [18, 19], magnetic torque measurements [20] and nuclear magnetic resonance [21] were employed. Nowadays, it is generally accepted that Mn has a complex noncollinear antiferromagnetic spin structure with large magnetic moments on site I and II and much smaller moments on the remaining positions. The magnitude and directions of the magnetic moments depend on the assumption made in the simulation of the experimental results or in the theoretical calculations. Hobbs et al. [68] found magnetic moments of Mn atoms change as a function of the volume of the atoms assumed in the calculations. The increase of the size of α-Mn leads to the increase of magnetic moments of Mn atoms on site III and IV.

A structural transition from α-Mn to β-Mn takes place at T=1000 K. β-Mn is relatively simple. It is a cubic structure with 20 atoms in the unit cell which can be divided into two inequivalent sites [71]. It has been demonstrated that β-Mn remains magnetically disordered in the quenched phase down to the temperature of 1.4 K and exhibits strong spin fluctuation [72, 73]. In a narrow temperature interval between 1368 K and 1406 K, fcc γ-Mn is stabilized. γ-Mn shows antiferromagnetic ordering below the the Néel temperature of 500 K [74, 75] in the quenched phase. A lattice distortion accompanied to the magnetic ordering occurs similar to the α phase. Above 1406 K, until the melting temperature of 1517 K, a bcc δ phase is formed.

Various structural phases of Mn can be stabilized at room temperature by epitaxial growth on different substrates. When deposited on close packed surface of fcc(111) or hcp(0001), it was found that Mn first adopts a close packed structure following the structure of the substrate [76]. A $(\sqrt{3} \times \sqrt{s})R30°$ superstructure, which is also called "expanded" phase of Mn, was observed when Mn exceeds certain thickness [77, 78, 79]. Similarities between the "expanded" Mn and α-Mn were found with photoemission [77] and extended x-ray absorption fine structure (EXAFS) [79] measurements. Some literature proposed structural models using α-Mn(111) as a prototype [76, 78]. A recent paper reported the epitaxial growth of α-Mn on MgO(111) at a high substrate temperature (200°C) [80]. They concluded that Mn grown on MgO(111) has (110) texture of α-Mn. The structural features resemble those of metastable "expanded" Mn, indicating a possible connection between α-Mn and the "expanded" Mn.

As to the growth of Mn on (001) cubic surfaces, tetragonal structures were observed. For example, tetragonally distorted γ-Mn is stabilized on Cu(001) or Ni(001) and assumes a high-spin antiferromagnetic type-I ground state [81, 82]. Body centered tetragonal (bct) Mn has been produced by epitaxial growth on Fe(001) with an in-plane lattice constant of a=b=2.866 Å and an out-of-plane lattice constant of c=3.228 Å [83]. The bct phase persists up to the thickness between 10 to 20 ML de-

pending on the growth conditions [25]. The bct Mn films show a layer-wise antiferromagnetic structure [22, 23]. It was proposed by several groups that subsequently deposited Mn undergoes a structural transition to α-Mn [84, 85]. Up to now, there are no direct or conclusive evidences, yet.

In our experiment, we investigated Mn films deposited on Fe(001). A structural transition was observed as the thickness of Mn increased. The structure of Mn after the transition is not exactly α-Mn. It has a structural unit cell twice as large as that of α-Mn. The structure was checked with LEED and STM. Further, the magnetic properties of reconstructed Mn films were investigated with Sp-STM on the atomic level which confirmed a noncollinear spin structure within the large reconstruction unit cell.

4.2   Growth and structure of Mn on Fe(001)

4.2.1   Growth of Mn on Fe(001)

Mn was deposited on an Fe whisker while keeping the substrate temperature at 373 K. The growth rate was about 0.5 ML per minute. The intensity of MEED spots was recorded during the growth process. Figure 4.2 gives a typical MEED curve. The MEED intensity decreased very fast as soon as the shutter was opened which means either the surface was notably roughened or most likely Mn has a different diffraction coefficient. Two maxima following the initial drop in the MEED curve can be considered as the completion of the first and second atomic layer from
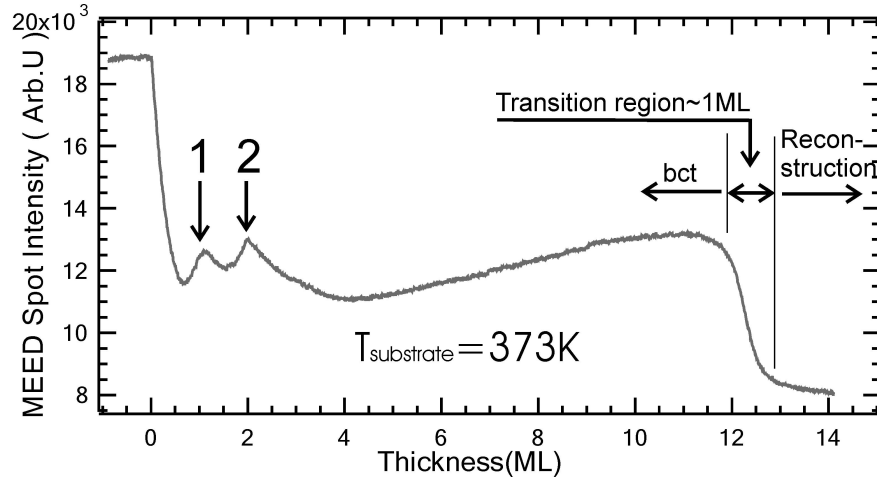

Figure 4.2: MEED spot intensity as a function of the Mn thickness. 1 and 2 indicate two maxima in the curve. Two structural regions, one is known as bct structure, the other one is reconstructed Mn, and the transition region (TR) of about 1 ML between the two structural regions can be seen.

which the growth rate was determined. The oscillations in the MEED curve imply a layer-by-layer growth mode of Mn on Fe(001) at least for the first two or three monolayers (ML). RHEED and EXAFS measurements [84] have shown the layer spacing of Mn films up to 2 ML was slightly smaller than thicker films [83, 84]. STM measurements [86] show totally different island shape and size of 0.6 ML and 5.1 ML Mn films grown on Fe(001) at a substrate temperature of 420 K indicating a change of growth mode. In our measurements, the MEED intensity was almost constant or even slightly increased after three monolayers. We attribute the disappearance of the MEED oscillations to the change of growth mode to the step flow growth (or almost step flow mode) after 2 ML which may happen at high temperature growth. In the step flow mode, the roughness of the surface does not change so that the MEED intensity is stable. At about 12 ML, the MEED intensity decreased dramatically within 1 ML. This is due to the structural transition as has been discussed in the literature [84, 85]. The transition may occur at varying thickness from 10 to 20 ML depending on the pressure, substrate temperature or substrate quality.

LEED and STM observations confirmed the change of growth mode and accompanied structural transition in the MEED curve. Figure 4.3 gives the LEED pattern and the STM image of 10.2 ML Mn on Fe(001). The LEED pattern showed a sharp
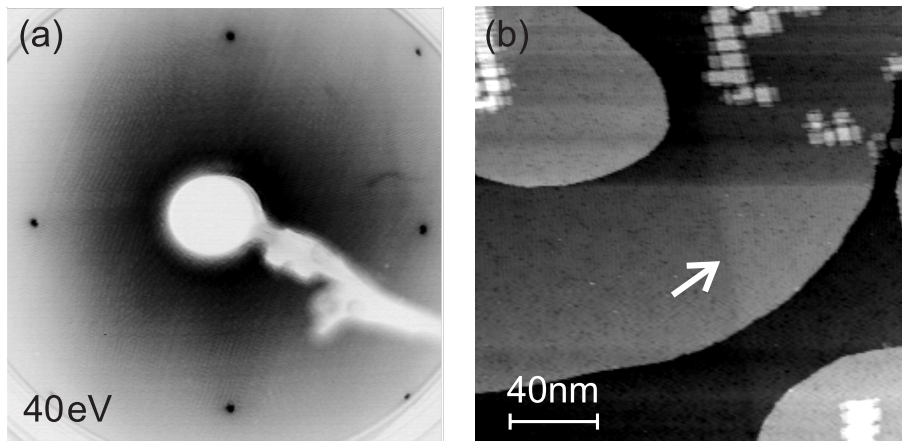

Figure 4.3: (a) LEED pattern of 10.2 ML Mn on Fe(001). Sharp (1×1) pattern with weak diffuse background was observed. (b) Corresponding STM image shows Mn terraces around 100 nm in width. U_{bias}=0.1 V, $I_t = 3$ nA. The arrow indicates a buried Fe step on the substrate.

(1×1) structure which did not change much in the whole thickness range before the transition took place. STM image (Fig. 4.3 (b)) showed atomically flat Mn terraces of about 100 nm in width. This is similar to the situation of step flow growth. The steps of Mn do not follow the steps of the substrate since the terraces of the Fe surface are as large as several hundred nm. A buried Fe step was visible as indicated by the white arrow in the STM image because of the different layer thickness of bct Mn (1.6 Å) and bcc Fe (1.4 Å). Some small rectangular shaped islands were
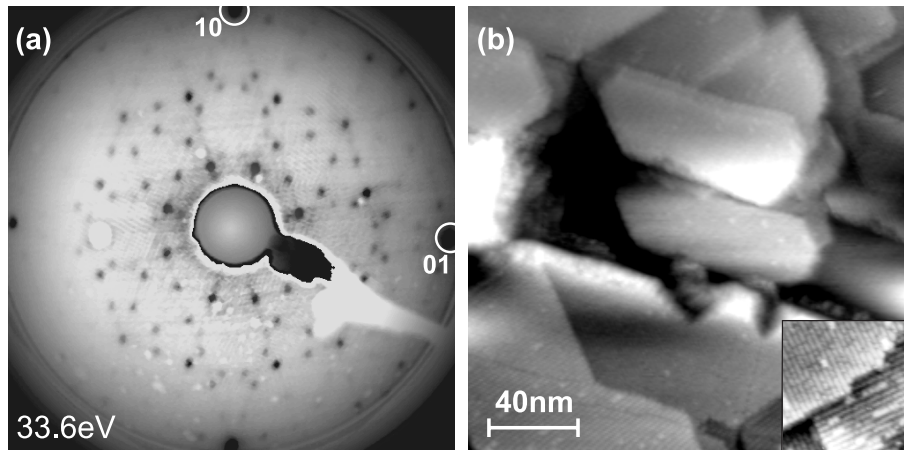
Figure 4.4: (a) LEED pattern of 14 ML Mn on Fe(001). (1×1) diffraction spots are indicated in the picture. (b) Topography of 14 ML Mn films. U_{bias}=0.1 V, $I_t = 3$ nA. The inset image shows an enlargement of the surface area.

observed which can be the precursor of the following structural transition. The structure of bct Mn films on Fe(001) has been studied intensively. We will not go much into detail of it.

Figure 4.4 gives the LEED pattern of 14 ML Mn on Fe(001) and the corresponding STM image. The LEED pattern is complicated indicating a totally different structural phase of Mn. The explanation of the complex LEED pattern will be given in the following section. The STM image (Fig. 4.4 (b)) gave a rather rough surface containing rectangular (or close to rectangular shape) terraces with deep holes. Periodic features were observed on the surface (see inset of Fig. 4.4 (b)) which should be related to the complex LEED pattern. Obviously, a transition from simple bct to a large superstructure happened. The transition finished within one monolayer as shown in the MEED curve indicating that there exists a critical thickness where Mn atoms start to rearrange. It is most likely that not only the atoms of surface layer joined in the rearrangement but also the the whole film was involved.

4.2.2 Reconstruction determined with LEED and STM

The LEED pattern is identified as a superstructure as given in Fig. 4.5 (b). Figure 4.5 (a) shows the way to extract information from the LEED pattern. Each cross of the lines corresponds to a diffraction spot. The extension of the lines go through the (1×1) spots which means the reconstruction is related to the substrate lattice. Here only the diffraction spots of one domain are marked by the cross lines. In a similar way, the diffraction spots from other domain can be determined. The size and orientation of the domains are shown in Fig. 4.5 (b) in real space. There are eight domains or four unique subpatterns relating to the four fold symmetry of
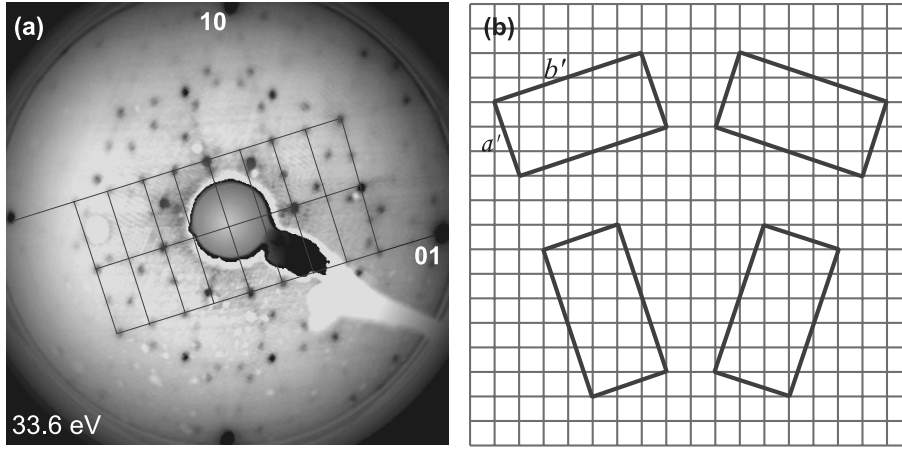
37

Figure 4.5: (a) LEED pattern of 14 ML Mn on Fe(001). The lines on the image act as a guidance to extract structural information from the LEED pattern. (b) The size of the Mn reconstruction is shown in real space relating the lattice of Fe substrate. The small square lattice represent the Fe substrate. The lattice constant is 2.866 Å. Four rectangles represent four unique subpatterns of Mn reconstruction. $a' = 9.06$ Å, $b' = 18.12$ Å.

Fe(001) surface. The reconstruction is of type $(\sqrt{10} \times 2\sqrt{10})R18.4°$ or in matrix representation $\begin{pmatrix} 3 & 1 \\ -2 & 6 \end{pmatrix}$. The unit cell size calculated by adopting the lattice of bcc Fe is $a' = 9.06$ Å, $b' = 18.12$ Å. This is approximately twice as large as the unit cell of the (001) α-Mn which is 8.87Å$\times$ 8.87Å [19]. Though it has been proposed by a few groups [84, 85] that the reconstructed Mn is α-Mn, there is no strong evidence reported yet. Our LEED observations indicate a structure more like a $p(2 \times 1)$ reconstruction of α-Mn.

Figure 4.6 gives the STM images of the reconstructed Mn surface. The surface is characterized by parallel lines of protrusions separated by $b \approx 18$ Å. The distance between two protrusions within one line is $a' \approx 9$ Å as shown in Fig. 4.6 (a). The size agrees well with the unit cell calculated from the LEED pattern. According to the LEED pattern, there are four unique subpatterns. In the STM images, they correspond to differently oriented parallel lines running along [130], [$\bar{1}$30], [310] and [$\bar{3}$10] which are all shown from Fig. 4.6 (a) to (d). Figure 4.6 (a) and (b) are slightly different from Fig. 4.6 (c) and (d) because of the different status (shape) of the STM tip. The influence of tip on the STM images will be discussed later in this Chapter. The protrusions act as basic growth units as seen from STM image. Some protrusions in the top most layer are missing, such that the protrusions in the layer below can be seen. This allows to estimate the layer thickness to about 1 Å. There are between 14 and 15 Mn atoms in the volume of 9 Å$\times$18 Å$\times$1 Å when taking the packing density of α-Mn. This block is the growth unit and about half of the Wigner-Seitz cell of α-Mn of 29 Mn atoms. From the unit cell size, it can be concluded that the film grows in the [001] direction of α-Mn. Thus, in average,
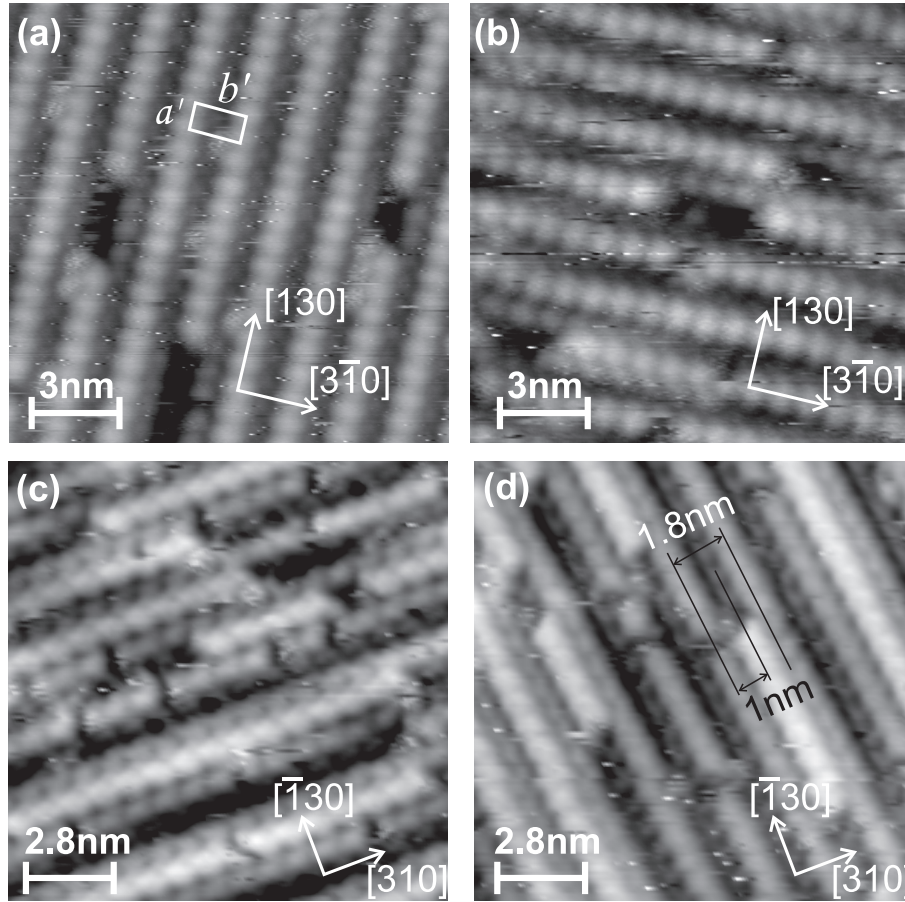
Figure 4.6: Topography of reconstructed Mn surface. U_{bias}=0.1 V, $I_t = 3$ nA. Four different oriented patterns were observed characterized by stripes running along [130],[3$\bar{1}$0], [310] and [$\bar{1}$30] as shown from (a) to (d). The surface unit cell is indicated in image (a) where $a' \approx 9$ Å, $b' \approx 18$ Å. In image (d), a lateral shift between two stripes from one layer to the next layer is indicated.

every two layers, 29 Mn atoms are grown. Since only full atoms can be added, there must be a small difference between the odd and even layers induced by one atom if the structure stays as α-Mn. Even though the difference may be trivial, it cannot be distinguished in STM images. Most probably, two unit cells of α-Mn experience different distortions which give the double surface periodicity. The in-plane translational vector along the long side of the unit cell from one layer to neighboring layer can be measured due to the incompletion of the top most layer. As shown in Fig. 4.6 (d), the shift vector along the long side of the unit cell is about 10 Å. It is difficult to determine the shift vector along the short side of the unit cell precisely due to the limited resolution of the image.

Atomic resolution within the reconstruction unit cell was obtained in high tunneling current and low bias voltage limit as shown in Fig. 4.7. The reconstruction unit
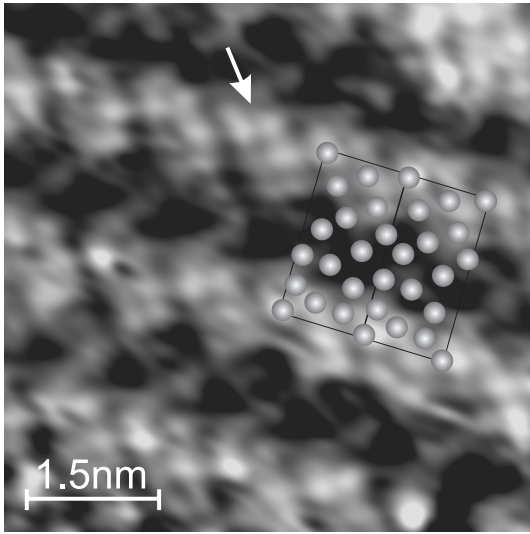
Figure 4.7: Atomically resolved STM image of Mn reconstruction. The image was taken with a W tip. U_{bias}=0.03 V, I_t = 25 nA. The positions of Mn atoms within the reconstruction unit cell are estimated.

cell is characterized by double atomic rows as indicated by the white arrow in the image. The distance between the two atomic rows is around 3 Å while the distance between the two atoms within the same row is about 4 Å. The in-plane positions of the atoms within the unit cell can be determined especially for the atoms in the peak position of the reconstructed surface. The resolution in the valley of the reconstruction is not sufficient to distinguish single atoms. In this case, 14 atoms are considered in one reconstruction unit cell as has been determined from the volume of the growth unit. From the STM image, we can see that Mn atoms tend to form dimers at the surface region which is possibly due to the dangling bonds of Mn atoms at the surface.

More information from LEED pattern

At low energy, additional spots which are not included in the diffraction pattern of $(\sqrt{10} \times 2\sqrt{10})R18.4°$ reconstruction were observed in the LEED. As shown in Fig. 4.8, eight more spots marked by the white circles are clearly visible at 17.9 eV. These spots are at the position of ([1/5, 1/2). There are two possible origins of these extra spots. One is that these spots come from a totally different superstructure, for example, $p(2 \times 5)$. In the STM measurements we never observed other kinds of reconstructions besides the $(\sqrt{10} \times 2\sqrt{10})R18.4°$ reconstruction. Therefore, this explanation is not convincing. Another origin is that the extra spots are related to the $(\sqrt{10} \times 2\sqrt{10})R18.4°$ reconstruction. In LEED, at certain energies, the scattering phase between two adjacent layers is a multiple of 2π and the interference is constructive, giving additional spots in the pattern. If we convert the (1/5,1/2) diffraction spots into real space and deduce the in-plane translational vector from one reconstruction layer to the neighboring layer as shown by the arrows in Fig. 4.8 (b). The translational vector along the long side of the reconstruction unit cell is 9.9 Å , consistent with the STM observation. The shift vector along the short side of the reconstruction unit is 2.7 Å. This gives a clue to build the structure of the
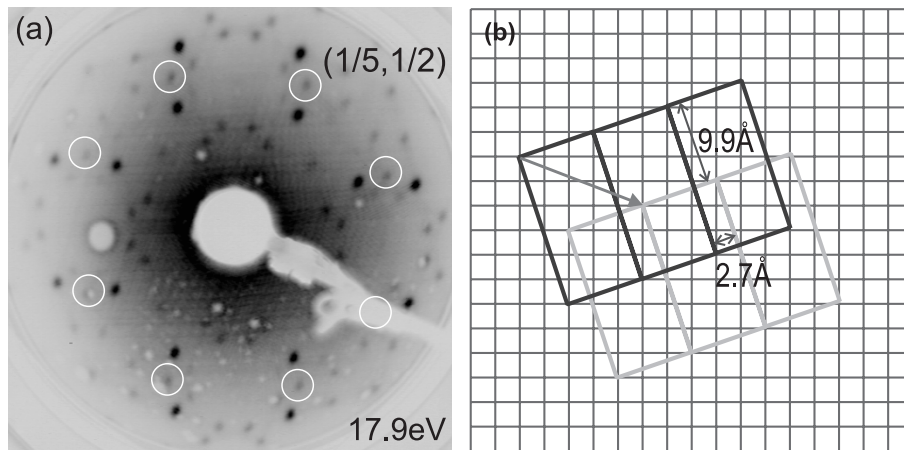
Figure 4.8: (a) LEED pattern of 14 ML Mn on Fe(001). The film is the same one as shown in Fig. 4.4. compared to Fig. 4.4 (a), additional spots at e = 17.9 eV are visible at (1/5,1/2) as marked by the white circles. These spots are related to the translational vector of the reconstruction unit from one layer to the neighboring layer as shown in (b). The substrate lattice, the reconstruction unit cell are drawn. The translational vector corresponds to the (1/5,1/2) spots is marked by the arrow. The shift of the reconstruction unit between neighboring layers along the long and short side of the unit cell are given, too.

reconstructed Mn.

In short, Mn was grown on Fe(001) at the substrate of 373 K. Above certain thickness, a structural transition from bct Mn to a reconstructed Mn happens. By examining the LEED pattern and STM images, the reconstruction is identified as $(\sqrt{10} \times 2\sqrt{10})R18.4°$. The growth unit and procedure were estimated which gives a clue that the reconstruction may be not simple α-Mn.

4.3 Surface spin structure of reconstructed Mn

4.3.1 From a layer wise antiferromagnet to a complex spin structure

If the thickness of Mn was chosen within the transition region, bct and reconstructed Mn coexist. The Sp-STM image shows flat bct Mn terraces and reconstructed islands as given in Fig. 4.9. The images were taken with a ring electrode. As already discussed in Chapter 2 and 3, this technique gives the topography and spin signal at the same time. In the topographic image, one can see that most of the surface is atomically flat. An atomic step edge of bct Mn runs across the image. There is a reconstructed island in the bottom-left corner of the image. On the top of the island, periodic features were observed. This is the same reconstruction of Mn as discussed

before which means the reconstructed Mn already starts to appear as islands with a typical height between 0.5 nm and 1.5 nm. In the corresponding spin channel (see Fig. 4.9 (b)), a strong contrast between the two neighboring bct Mn terraces demonstrates the layer-wise antiferromagnetic order of bct Mn on Fe(001) [23]. The origin of the spin contrast has been discussed in Chapter 3. On the top of the reconstructed island, a regular structure was seen in the spin signal. This suggests that the reconstructed Mn atoms show magnetic moments as well.
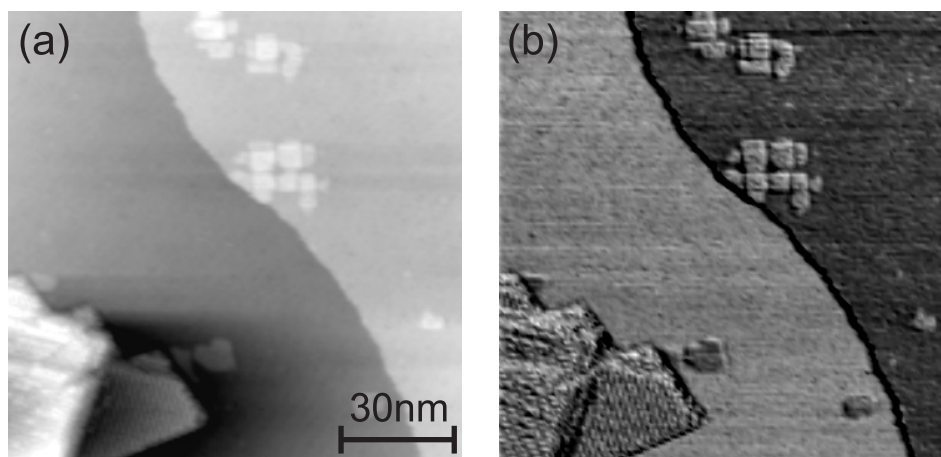
Figure 4.9: (a) Sp-STM images of (a) the topography and (b) the spin signal of 11 ML Mn on Fe(001) (U=0.1 V, I=3 nA). The atomically flat terraces in (a) are bct Mn separated by an atomic step edge. Spin contrast between neighboring atomic layers was observed in (b). The island in the left-bottom part is reconstructed Mn.

Atomically resolved images can be obtained in the spin channel with the ring electrode. Figure 4.10 (a) and (b) show the topography and the corresponding spin signal. In the topography, the resolution is not fully atomic because most probably, s-electrons tunnel in the Fe ended tip while high resolution images on metal surface were attributed to the d state tip [56]. In the spin channel, the spin of single atoms can be resolved as shown in Fig. 4.10 (b). The reason of a better spin image is related to the lower spatial frequency of the spin structure as has been discussed in Chapter 2. An averaging over many unit cells of Fig. 4.10 (b) was done to reduce the noise (cf. Fig. 4.10 (d)). As a comparison, the atomically resolved topography image that has been shown in Fig. 4.7 is given here again. In the spin images, a strong contrast was observed. The spin image is characterized by double rows of white and black dots, which implies a nearly opposite spin polarization of neighboring rows. Additionally, an intermediate spin contrast is found at the lower ends of the rows corresponding to topographic positions between the reconstruction lines. In the STM images, the ring electrode was arranged nearly perpendicular to the reconstruction lines and nearly parallel to the dimer rows. The high contrast of the white and black dots suggests that these correspond to high spin Mn atoms. When putting the structural model of Fig. 4.10 (c) to the spin image, the positions
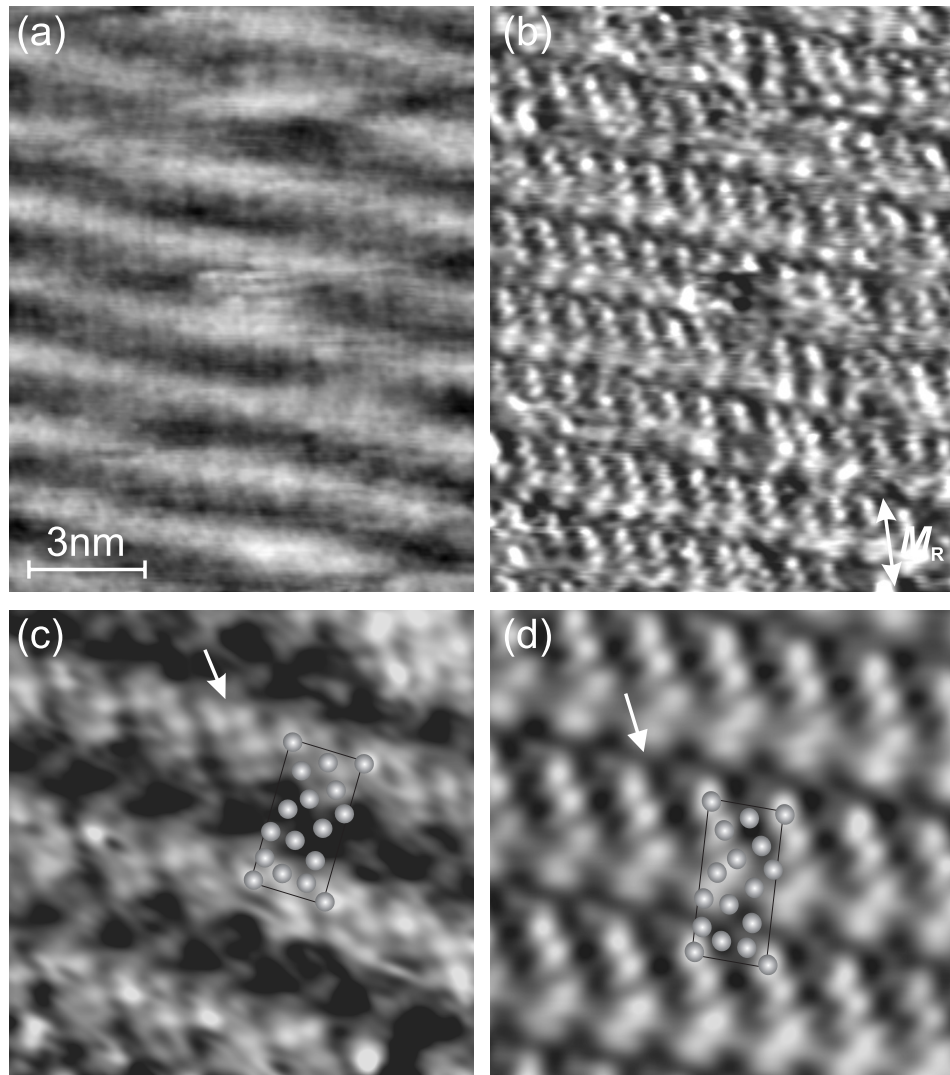
Figure 4.10: (a) High resolution Sp-STM images of (a) the topography and (b) the spin signal of the reconstructed Mn surface (U=0.1 V, I=3 nA). (c) atomic resolved image taken with a W tip (U=0.03 V, I=25 nA). (d) averaged spin image over many unit cells of (b). The black rectangles in c) and d) indicate the unit cell. The positions of the atoms within the unit cell estimated from (c) are superimposed on (d). The images are slightly distorted due to drift.

of the atoms fit with the minima and maxima of the spin polarization. Structurally, the 29 Mn atoms in the Wigner-Seitz cell of α-Mn canbe divided into 1 MnI, 4 MnII, 12 MnIII and 12 MnIV which are crystallographically inequivalent. In most experimental [18, 19, 21] and theoretical [87, 88] investigations of α-Mn, MnI and MnII atoms have much larger magnetic moments (around $2\,\mu_B$ or larger) than MnIII and MnIV (around $0.5\,\mu_B$). Thus, the terminated bulk α-Mn(001) surface exposes six high spin atoms in the area of $9\,\text{Å}\times18\,\text{Å}$. However, the positions of these high

spin atoms do not agree with the positions of the high spin atoms as observed with Sp-STM. This indicates that the reconstruction involves a reconfiguration of the surface atoms with respect to bulk α-Mn. When taking into account the largely covalent nature of the Mn-Mn bond in α-Mn, an open surface leaves dangling Mn bonds behind. To saturate these, it is likely that the surface Mn atoms form dimers as indicated by the double rows. This also explains the nearly antiparallel orientation of the moments reflected by the high contrast in the spin image. Neglecting the bonds to the subsurface atoms, the atoms of the dimers need an antiparallel magnetic alignment to form a covalent bond.

4.3.2 The non-collinearity of the spin structure of reconstructed Mn

To find out, if the spin structure at the surface is a collinear one, Sp-STM images of different tip orientations were taken. Figure 4.11 (b) and (d) show the spin images of two structural domains with perpendicular orientations of the reconstruction lines. The spin images show the same periodicity as Fig. 4.10 (d) but give less detailed information. Note that the two spin images were cut from one larger image, i.e., were recorded with the same tip. In order to reduce the noise level, we averaged the images over many unit cells. The averaged results are shown in the inset of these images. Structurally, the two perpendicular subpatterns are the same. They do not show significant differences in the topography (cf. Fig. 4.11 (a) and (c)) while in the spin channel, they appear differently. In Fig. 4.11 (b), the ring was almost perpendicular to the lines. The image shows bright dots corresponding to the high moment atoms in Fig. 4.10 (d). In the center between two bright lines, there are well separated gray dots which we identify as the intermediate contrast in Fig. 4.10 (d). Their topographic positions are in between the reconstruction lines. In Fig. 4.11 (d), the ring was almost parallel to the lines. The image is characterized by well ordered bright dots forming a rectangular shape. Our Sp-STM is sensitive to the in-plane spin polarization parallel to the magnetization direction of the ring. The brightness in the spin images reflects the magnitude of the spin polarization projected to the ring direction. When comparing the spin signals of two unit cells (cf. insets of Fig. 4.11 (b) and (d)), one realizes that they are not proportional, which is a necessary condition for a collinear spin arrangement. There are two possibilities that can explain the differences in the spin structure. First, the two domains have different spin configurations due to their different orientations with respect to the underlying Fe whisker magnetization. Second, the unit cell has a noncollinear spin structure not related to the underlying Fe. In order to distinguish between the two, we rotated the ring by 90° with respect to the Fe whisker magnetization. In the experiment, we used second Fe whisker which was rotated by 90°. In this case, the magnetization direction of the ring was perpendicular to the long edge of the Fe whisker. The resulting spin images are shown in Fig. 4.12 which revealed that when the ring is

parallel to the reconstruction lines, the spin image is similar to Fig. 4.11 (d). Well separated dots were observed. The spin image is similar to Fig. 4.11 (b) when the ring was perpendicular to the reconstruction lines. The image was characterized with bright lines. This means that the spin images depend only on the direction of the ring with respect to the direction of the reconstruction and not on the direction of the Fe magnetization. The Néel temperature of α-Mn is 95 K. The onset of antiferromagnetic order in the Mn reconstruction at room temperature is induced by the direct exchange coupling of Mn atoms with the ferromagnetic Fe atoms of the underlying Fe whisker. At the interface, the orientation of Mn moments is pinned by Fe moments. If there was no additional crystalgraphic anisotropy to break the symmetry, the orientation of Mn moments would follow that of Fe as in the bct Mn phase. This is not the case as was shown by the similarity of the spin images on rotated whiskers. Therefore, in the Mn reconstruction, the crystal field seems to
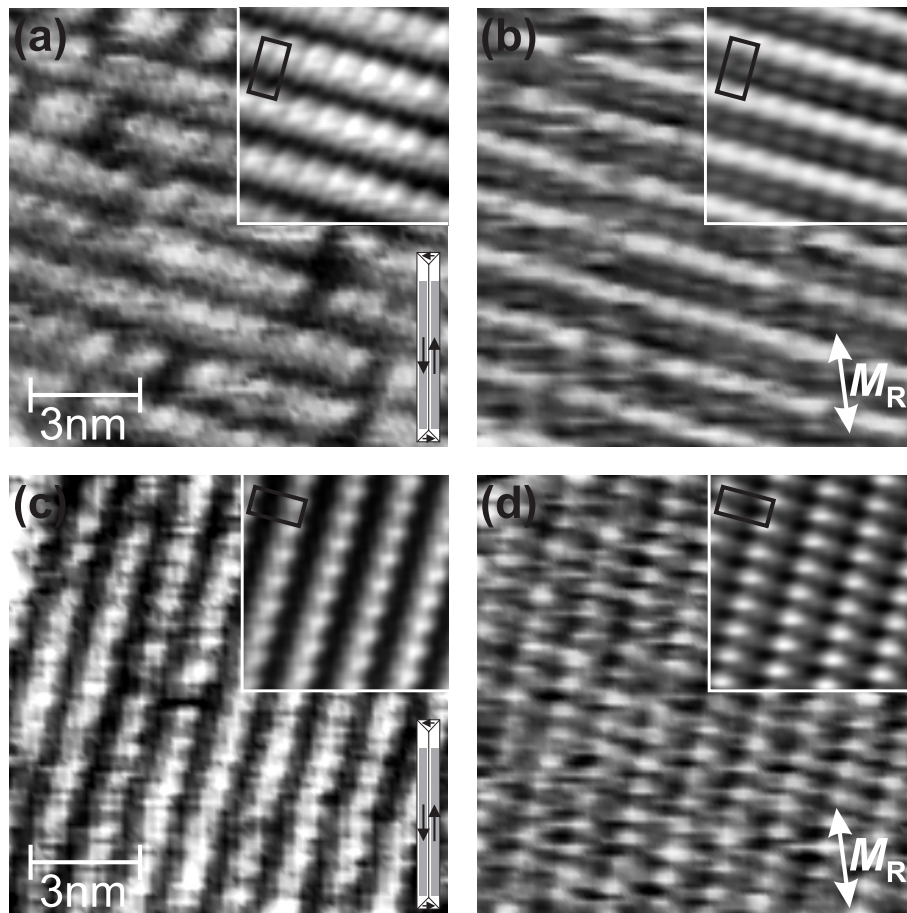

Figure 4.11: Topography (a), (c) and the corresponding spin signal (b), (d) of two perpendicular domains of the reconstructed Mn (U=0.1 V, I=3 nA). The orientation of the Fe whisker is represented by the schematic picture of Fe whisker with magnetic domains. M_R shows the magnetization direction of the ring. The images are cut from one large image.
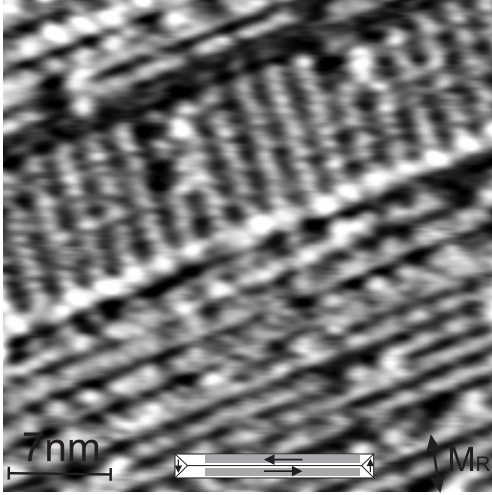
Figure 4.12: Spin image of Mn reconstruction on Fe(001) (U=0.1 V, I=3 nA). The magnetization of the ring was set perpendicular to the Fe whisker. The orientation of the Fe whisker is represented by the schematic picture of Fe whisker with magnetic domains. M_R shows the magnetization direction of the ring.

dominate the magnetic anisotropy and the magnetic structure. The magnetic structure of the reconstructed Mn is related to the Mn structure itself. The fact that the magnetic structure is not related to the orientation of the the reconstruction with respect to the Fe whisker, but different domains have different spin patterns implies that the reconstructed Mn has a noncollinear spin structure. The noncollinear antiferromagnetic structure of the reconstructed Mn surface is not surprising since the superstructure is similar to a doubled α-Mn while bulk α-Mn has a complex noncollinear spin structure [19].

If we take into account that the two perpendicular domains have the same spin structure, Fig. 4.11 (b) and (d) actually show two orthogonal components of this structure. We can combine the two spin images in Fig. 4.11 and obtain a magnetic vector map within the reconstruction unit cell. Special care needs to be taken in order to combine the two orthogonal components. The signal from lock-in amplifier only gives relative magnitude of the spin polarization. In this case, a magnetically compensated surface is assumed. The net spin polarization of one reconstruction unit cell is zero. Thus, the average signal over one complete unit cell can be treated as zero spin polarization. The average signal of Fig. 4.11 (b) and (d) are the same which agrees with the assumption of magnetically compensated surface. However, this cannot exclude the possibility that the averaged spin polarization have different projections on the the out-of-plane directions. Nevertheless, with the assumption of in-plane compensated surface, the inset images in Fig. 4.11 (b) and (d) can be rescaled to zero spin polarization as shown by Fig. 4.13 (a) and (b). The blue-white-red scale in Fig. 4.13 (a) and (b) is proportional to the spin polarization projected along the magnetization direction of the ring electrode. The relation between the two images are sketched in Fig. 4.13. Signal(a) and signal(b) are the rescaled spin polarization as shown by Fig. 4.13 (a) and (b) and give two orthogonal components of one unit. Thus, these two signals can be combined (rotate Fig. 4.13 (b) by 90° to fit with Fig. 4.13 (a)) as $\sqrt{signal(a)^2 + signal(b)^2}$ which gives
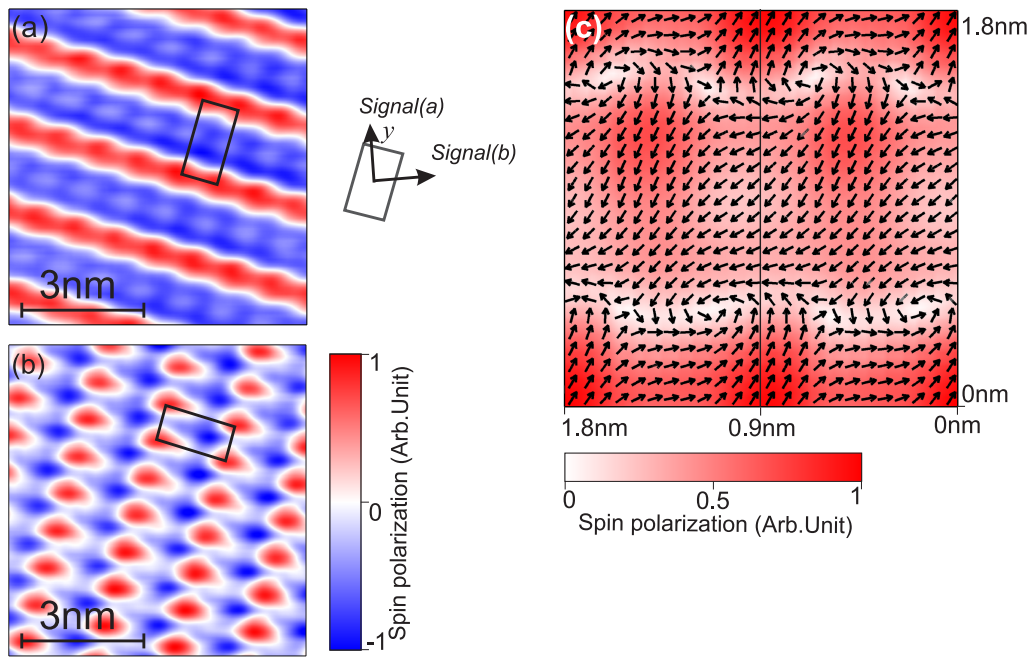
46

Figure 4.13: (a) and (b) are spin polarization of two domains averaged over many unit cell of Fig. 4.11 (b) and (d) scaled with the assumption of magnetically compensated surfaces. The color scale in (c) represents the magnitude of spin polarization of two Mn reconstruction unit cells by combining image (a) and (b) in a way as sketched on the left side of (c). Signal (a) and signal (b) represent the signal from image (a) and (b). The directions of the arrows in (c) gives the directions of the spin polarization.

the total spin polarization. The angle of the spin polarization can be determined by $signal(a)/signal(b)$ while the starting point of the angle is set by the orientation of ring. The resulting image is given in Fig. 4.13 (c). Both the size and the direction of the in-plane spin polarization vary within the unit cell as indicated by the white-red coded background and the black arrows in Fig. 4.13 (c). Clearly, the spin distribution within the unit cell deviates from a collinear configuration. Due to the limited lateral resolution of the combined scan of about 5 Å the vector plot does not resolve drastic change of spin polarization within the dimers. Fig. 4.13 (c), however, still reveals the complexity and non-collinearity of this reconstructed α-Mn. The antiferromagnetically coupled surface dimers and the noncollinear surface spin structure indicate a tendency of the surface to form a compensated in-plane spin structure.

4.4 Discussion: Resolving complex spin structures

Mapping the complex antiferromagnetic spin structure with Sp-STM

Traditional techniques for measuring complex antiferromagnetic structures are almost all bulk sensitive such as neutron scattering. These methods mostly operate in reciprocal space and involve complicated calculations to deduce the spin structure in real space. Moreover, these techniques require a certain amount of material to acquire reasonable signal which restricts the application of these techniques to epitaxial grown thin films.

Sp-STM offers a promising possibility to map complex antiferromagnetic spin structures in real space with atomic resolution. To determine the spin structure of the surface atoms in three dimensions, which is very important when measuring the non-collinear antiferromagnetic surfaces, the one out-of-plane and two in-plane components should be measured independently. For Sp-STM operating in constant mode and spectroscopic mode, separation of the in-plane and out-of-plane components is possible by modifying magnetization direction of the tip, but the magnetization direction in the plane is random. For the Sp-STM operating in differential magnetic mode, the direction of the tip magnetization can be changed by using different shaped tip, i.e., rod or ring. Since the magnetization direction of the ring is confined in the plane of the ring by the shape anisotropy, the in-plane direction can be exclusively decided.

The disadvantage of Sp-STM is that the spin image only gives a relative magnitude of spin polarization along certain direction. When the structure is very complicated, the explanation of the image becomes difficult. For example, in Fig. 4.10, we cannot assign spin direction to single atoms due to lack of knowledge of what signal represents zero spin polarization. In the case of a compensated surface, the zero spin polarization can be treated as the average signal. Thus, the direction of the spin polarization can be decided as well. In principle, the three dimensional spin arrangement of the surface atoms can then be figured out. Technically, this is nearly impossible because the spin polarization of the STM tip is uncontrollable. According to equation 3.4, a change of the spin polarization of the tip will change the contrast measured by the Sp-STM which means different images taken with different tips or even with one tip at different time are incomparable. In our case, a measurement of structurally and magnetically identical two orthogonal domains within one STM scan ensures the stability of the tip. Thus, a two dimensional vector map of spin polarization can be drawn.

The influence of the tip apex

A full understanding of atomically resolved spin images needs structural as well as magnetic information of the unit cell. It is difficult to obtain the arrangement of the surface atoms with STM especially when the surface atoms are reconstructed in large unit cells. One reason was already discussed in Chapter 2: the decay of the LDOS of a superstructure into the vacuum is much slower. The corrugation of electronic density above the surface is dominated by the superstructure which makes the single atoms hard to resolve. Second, when the corrugation of the superstructure is
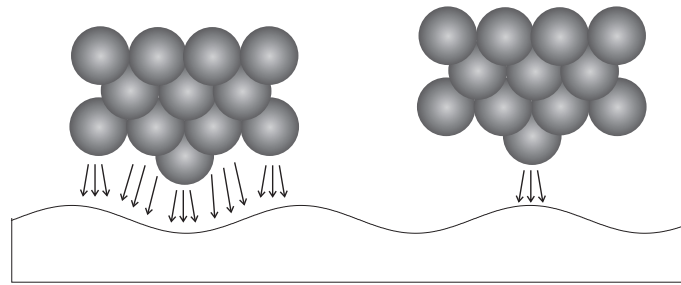
Figure 4.14: Schematics of the influence of the tip size in mapping a large corrugated reconstruction. The corrugation height is comparable to the size of the tip, i.e., around 1 Å. In the valley, a few atoms at the tip apex have comparable contribution to the tunneling current. In the peak position, the one atom at the very end dominates the tunneling current.

comparable to the size of the tip, the influence of the shape and size of the tip is not negligible. As sketched in Fig. 4.14, when the tip is at the valley position of the surface reconstruction, not only the last one atom at the tip apex gives the tunneling current, but also the atoms nearby may have a comparable contribution to the tunneling current. When the tip is at the peak position of the surface reconstruction, the contribution to the tunneling current of the very last atom is much lager than the other atoms at the tip apex. This has two direct effects on the STM images. First, the image is influenced by the shape of the tip apex. For example, in Fig. 4.6, the same structure shows slightly different features with different tips. Second, in the high resolution topography image as shown in Fig. 4.7, it is possible to resolve the single atoms at the peak position while in the valley, the high resolution is lost due to the finite size of the tip.

4.5   Conclusion

In conclusion, we have investigated the structural and magnetic properties of reconstructed Mn on Fe(001). First, we clarified that the structure of thick Mn films deviates from α-Mn. The structure is identified as $(\sqrt{10} \times 2\sqrt{10})R18.4°$. It is twice as large as the unit cell of α-Mn. Further, the spin configuration of the surface atoms of the reconstructed Mn was measured with Sp-STM. A noncollinear spin configuration in the unit cell was observed and a vector map of spin polarization was constructed from orthogonal measurements. The spin structure was explained on basis of the tendency of Mn to form covalent dimer bonds at the surface leading to a locally antiparallel orientation of the moments. Together with the complex crystallographic structure this results in a noncollinear spin configuration. Finally, we discussed the possibility of using Sp-STM to determine the noncollinear surface spin structure.

.

5. Structure and magnetic properties of equiatomic NiMn on Cu(001)

5.1 NiMn: an overview

Mn has five unpaired electrons in the outer shell which in principle gives a magnetic moment as large as $5\,\mu_B$, the largest among all transition metals. Such a large magnetic moment is believed to lead to the complexity of structural and magnetic behavior of Mn in its various single crystalline phases, as has been discussed in the previous Chapter. Due to its high magnetic moment, Mn plays an important role in determining the structure as well as the magnetic properties in Mn based alloys and compounds. Mn diluted semiconductors, such as MnGaAs [89], show fascinating properties which open the promising field of magnetic semiconductors. Alloys of Mn with ferromagnetic metals, such as Fe, Co, Ni show either ferromagnetic or antiferromagnetic order depending on the concentration of Mn and the structure of the alloys [90, 91, 34]. These alloys gained a lot of interest due to their applications.

In this work, we focus on the binary alloy NiMn as an antiferromagnetic model system. It has been shown in many studies that $Ni_x Mn_{100-x}$ alloys have different structural and magnetic phases at different compositions and temperatures. The detailed structural and magnetic phase diagram is given in Ref. [92]. More recent progress can be found in Ref. [90, 93]. In general, in the bulk, $Ni_x Mn_{100-x}$ undergoes a tetragonal distortion of the fcc lattice with either $c < a$ or $c > a$. Ni rich $Ni_x Mn_{100-x}$ alloys display ferromagnetism up to a Mn concentration of 25%. The onset of antiferromagnetic order is found at a Mn content of 30-35%. In between these two regimes, ferromagnetic long range order and antiferromagnetic short range order coexist [91, 94]. Long range chemically ordered structure of NiMn alloys are found in $Ni_{75}Mn_{25}$ and $Ni_{50}Mn_{50}$. $Ni_{75}Mn_{25}$ crystallizes in a Cu_3Au $(L1_2)$ structure and shows a strong ferromagnetism with Curie temperature of 753 K [95]. The magnetic moments of Mn and Ni are $3.83\,\mu_B$ and $0.47\,\mu_B$ [96]. $Ni_{50}Mn_{50}$ adopts a face centered tetragonal (fct) CuAu $(L1_0)$ structure and shows antiferromagnetism with Néel temperature as high as 1070 K [97].

The lattice constants of $L1_0$ $Ni_{50}Mn_{50}$ are a=b=3.74 Å and c=3.52 Å [97] as shown in Fig. 5.1. Mn and Ni atoms occupy alternative atomic sheets along the c axis. Neutron diffraction experiments showed that $Ni_{50}Mn_{50}$ has a collinear antiferro-

magnetic type-I (AF-I) spin structure where the nearest Mn atoms couple antiferromagnetically and the next nearest Mn atoms couple ferromagnetically [98]. The magnetic moments of Mn atoms are $4.0\,\mu_B$ according to Kasper et al. [98] and $(3.8\pm0.3)\,\mu_B$ according to Krén et al. [97]. The magnetic moments of Mn atoms lie in the Mn sheets, i.e., perpendicular to the c axis. Neutron diffraction experiments cannot distinguish between the two cases of Fig. 5.1 (a) and (b) because of antiferromagnetic domains in the bulk. The magnetic axis can be parallel either to [100] or to [110] direction of the crystal. The strong antiferromagnetic coupling of the nearest Mn atoms leads to a near vanishing of the Ni moments. The magnetic moment of Ni, if existing, is smaller than $0.2\,\mu_B$ [97].
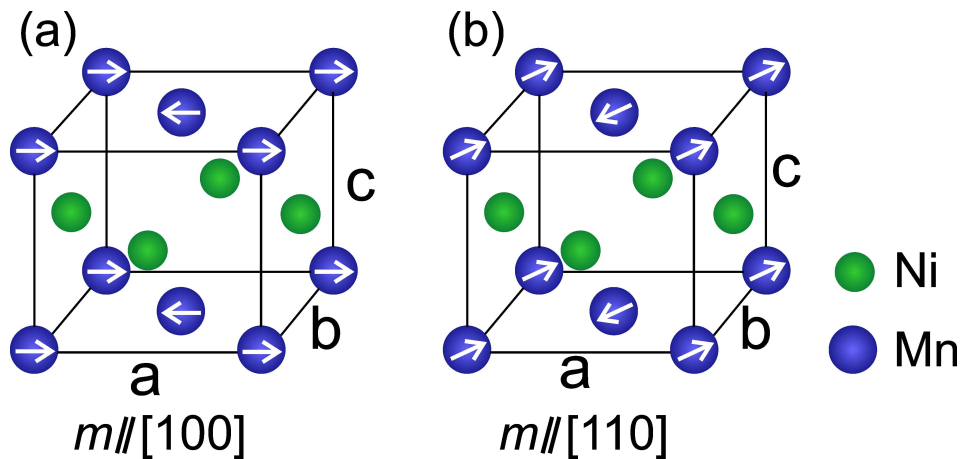
Figure 5.1: Structure and two possible spin arrangements of bulk $Ni_{50}Mn_{50}$. (a), the magnetic axis is along [100] direction. (b), the magnetic axis is along [110] direction.

Theoretical calculations confirmed the AF-I ground state of bulk $Ni_{50}Mn_{50}$ [99, 100]. Depending on the calculation methods used, magnetic moments are found to be $3.2\,\mu_B$ [99], $3.3\,\mu_B$ [100] or $3.4\,\mu_B$ [99] for Mn atoms and $<0.01\,\mu_B$ [99] for Ni atoms. The uniaxial magnetic anisotropy energy defined as the energy difference of the magnetic moments orientated perpendicular and parallel to the c axis is found to be -27.2 μeV/atom [99] which is consistent with the experimental results. The calculated four fold magnetic anisotropy energy in the ab-plane is -2.2 μeV/atom [99] which slightly favors the [100] direction. Such a small energy difference, as has been pointed by the authors [99], is at the limit of the accuracy of such calculations.

Due to the high Néel temperature of 1070 K of $Ni_{50}Mn_{50}$, many attempts were made to grow equiatomic NiMn thin films for its potential application as the pinning layer in exchange biased systems. To study the exchange properties, NiMn films were grown in contact with ferromagnetic layers. Most of the NiMn thin films were prepared by sputter deposition techniques [101, 102, 103, 104]. The substrates were usually Si wafers with certain seed layers such as Ta. The films were annealed to establish the antiferromagnetic $L1_0$ phase of NiMn. These NiMn films were in polycrystalline phase. Very few experiments of epitaxial grown single crystalline

Ni_xMn_{100-x} films have been published. Thamankar et al. [105] have grown Ni rich Ni_xMn_{100-x} on Cu(001). They found an improved layer-by-layer growth comparing to Ni/Cu(001). Wuttig et al. [106, 107] deposited Mn on Ni(001). They found that Mn and Ni intermix at a certain substrate temperature and form chemically ordered $Ni_{50}Mn_{50}$. LEED-IV measurements showed that Mn atoms stick out by 0.3 Å with respect to Ni atoms on the surface. Such a large buckling of the surface atoms was attributed to the large magnetic moments of the Mn atoms. O'Brien et al. [108] performed XMCD measurement on NiMn/Ni(001) following the preparation method of Wuttig et al. [106] and concluded that samples of 1, 2 and 4 ML Mn were ordered ferromagnetically and aligned parallel to the moments of Ni substrate. The results conflicted with the antiferromagnetic spin structure of bulk NiMn. They attributed the contradiction to the different lattice constant of bulk NiMn and NiMn on Ni(001). Calculations by Spišák et al. [99] showed that Mn is aligned antiferromagnetically from one layer to the next layer of NiMn on Ni(001). They proposed that the discrepancy with the experimental results is due to the roughness of the NiMn films. There are no further studies of this system published, yet.

Here, we grew equiatomic NiMn thin film on Cu(001) by co-evaporation which was initiated by our colleague C. Tieg [109]. We studied different thickness of NiMn thin films with LEED, LEED-IV, STM and Sp-STM. *Ab-initio* calculations were done for this system for comparison.

5.2   Growth and structure of NiMn on Cu(001)

Atomically flat Cu(001) surfaces were obtained by cycles of sputtering and annealing. Figure 5.2 gives STM images of the clean Cu(001) surface. The Cu(001) surface is characterized by terraces with a typical width larger than 50 nm. The steps run along the [110] direction of the crystal. Figure 5.2 (b) shows atomic resolution of the surface. The surface unit cell of Cu(001) surface has a size of 2.56 Å× 2.56 Å.

Ni and Mn were deposited on Cu(001) by co-evaporation while keeping the substrate temperature at 300 K. To achieve the right ratio between Ni and Mn, the growth rate of Ni was determined by depositing Ni on Cu(001). It is well known that Ni grows in a layer-by-layer fashion on Cu(001) up to 6 ML [110, 111]. The upper curve in Fig. 5.3 gives MEED oscillation of Ni on Cu(001) as a function of the deposition time. About six maxima were observed in the MEED curve while the oscillating amplitude reduced as the thickness of Ni increased. The maxima can be considered as the completion of each atomic layer. Thus, the growth rate of Ni on Cu(001) was determined, which was about 120 seconds per monolayer. It is not possible to determine the deposition rate of Mn directly in a similar way because Mn grows three-dimensionally on Cu(001). Fortunately, as already been pointed out in Ref. [105], the Ni rich Ni_xMn_{100-x} on Cu(001) shows an improved layer-by-layer
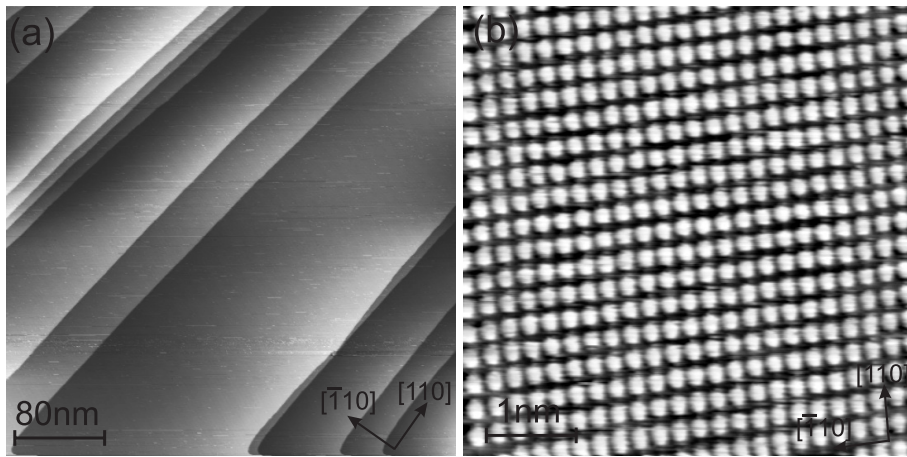
Figure 5.2: (a) Surface of Cu(001). $I_t = 3.0$ nA and $V_{bias} = 0.45$ V. (b) Atomically revolved STM image of Cu(001) surface. $I_t = 3.0$ nA and $V_{bias} = 0.04$ V. The crystalline orientations are indicated in the images. The scanning direction in (b) was rotated by 45° compared to (a).

growth compared to Ni/Cu(001). It was further demonstrated that the layer-by-layer fashion keeps as long as the ratio of Ni is above 40% when depositing Ni and Mn simultaneously on Cu(001) [109]. In the regime where the amount of Ni and Mn are almost equal, the layer-by-layer growth of NiMn can extend to more than 20 ML. Both Ni and equiatomic NiMn grow layer-by-layer on Cu(001). Therefore, if the MEED oscillations of NiMn show a periodicity which is half of that growing Ni alone, the ratio between Ni and Mn was considered as 50:50 as shown in Fig. 5.3. It is important to keep the rate of Ni constant in the experiments. From day to day measurements, the variation of the rate of Ni was within $\pm 5\%$. In this way, the ratio of Ni in NiMn thin films can be well controlled in the range from 45% to 55%. In
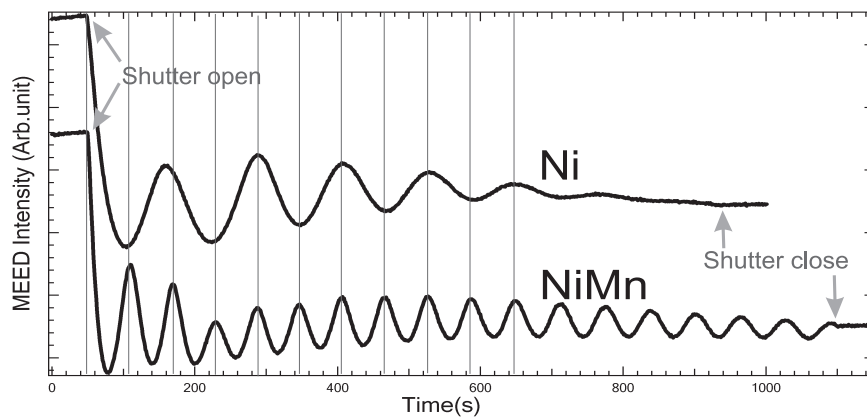

Figure 5.3: Intensity of the (0,0) MEED spot as a function of time during the growth of Ni and NiMn on Cu(001). The growth rate of NiMn is doubled compared to Ni.

the following text, if not especially specified, we prepared nearly equiatomic NiMn thin films.
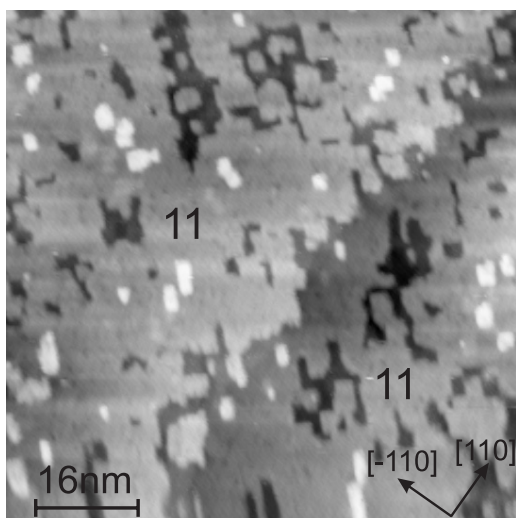

Figure 5.4: Topography of 10.8 ML NiMn on Cu(001). The tunneling current was 3 nA and the gap voltage was 0.57 V. The 11th layer on both side of a Cu step is marked by 11. The image is slightly distorted due to drift.

The morphology of NiMn films was checked with STM. Figure 5.4 gives the topography of 10.8 ML NiMn. We can see that the 11th layer (marked in the figure) was almost completed while the 12th layer (white areas) started to appear as some small square islands of a few nm in width. This reflects the layer-by-layer growth of NiMn. The edge of the islands are parallel to [010] direction of the crystal while the Cu steps are along [110] direction.

LEED observations reveal that NiMn films on Cu(001) have a chemical ordered structure. Figure 5.5 (a) and (b) show LEED patterns of clean Cu(001) and 10.8 ML NiMn on Cu(001), respectively. The pattern of Cu(001) gives sharp (1×1)
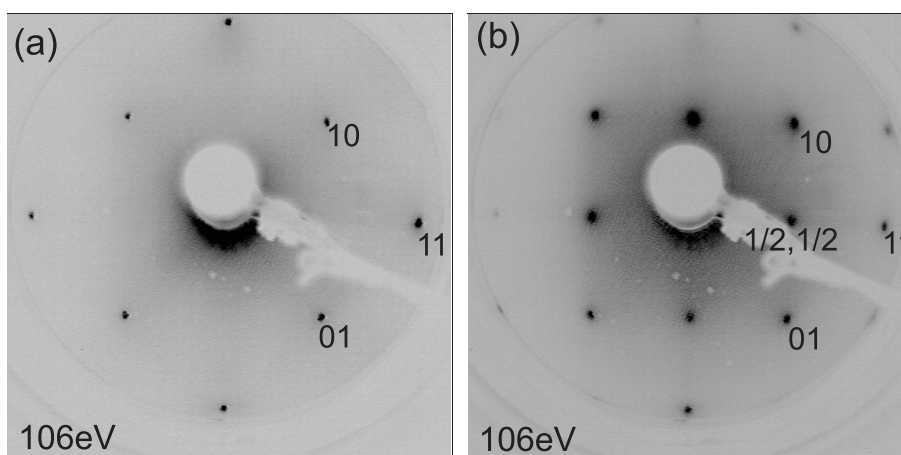

Figure 5.5: (a) (1×1) LEED pattern of clean Cu(001). (b) LEED pattern of 10.8 ML NiMn films on Cu(001). A $c(2 \times 2)$ superstructure was observed. (1×1) and $c(2 \times 2)$ diffraction spots are marked in the images.

55

spots while in the pattern of NiMn thin films, additional spots appeared at $c(2 \times 2)$ positions. The $c(2 \times 2)$ spots are quite strong compared to the (1×1) spots. A chemical order of NiMn was proposed by C. Tieg [109] as the reason for the $c(2\times2)$ pattern. In the chemical disordered binary alloy films, in general, only (1×1) LEED spots were observed, for example, in FeMn on Cu(001) [34]. According to the bulk
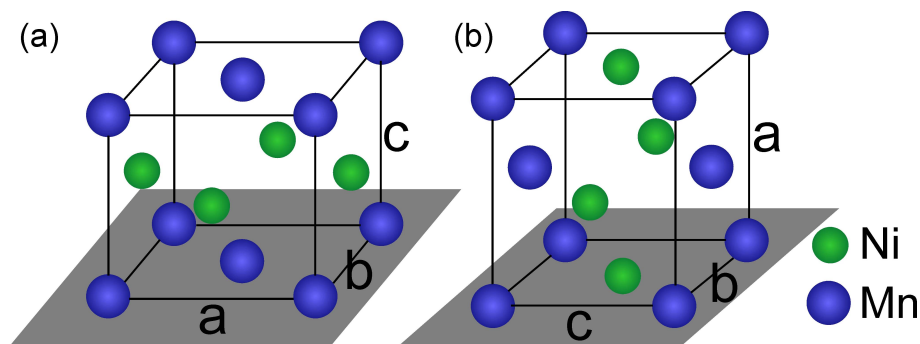

Figure 5.6: Two possible chemically ordered structures of NiMn thin films on Cu(001). The gray planes represent the Cu surface. (a) Ni (Mn) sheets are parallel to the Cu surface, (b) Ni (Mn) sheets are perpendicular to the Cu surface.

structure NiMn, there are two ways for NiMn to sit on the Cu(001) surface. One is shown in Fig. 5.6 (a), the Mn and Ni sheets are parallel to Cu(001) surface. In this case, the chemical order itself does not give a $c(2 \times 2)$ superstructure. Most probably, the Mn and Ni sheets are perpendicular to the Cu(001) surface as shown in Fig. 5.6 (b). In this case, the arrangement of surface Mn and Ni atoms naturally gives the $c(2\times2)$ superstructure. Since the NiMn films grow epitaxially on Cu(001) in a very nice layer-by-layer fashion and LEED patterns do not show any movement of the (1×1) spots, it can be assumed that in-plane lattice of NiMn thin films follows that of Cu(001).

STM observations confirmed the chemical order of the NiMn surface. Figure 5.7 (a) gives an atomically resolved topographic image of NiMn on Cu(001). The surface is characterized by bright spots forming a $c(2 \times 2)$ superstructure (as shown by square I), which originates from the chemical order of the NiMn surface. We think that the bright dots represent one element (either Mn or Ni). Additional features were present in the image as marked by square II. The bright dot (labeled as 2) in the center is closer to the bright dot in the right-bottom corner (labeled as 1). Correspondingly, the dark positions, which represent one element as well, are also distinguished as 3 and 4 with slightly different brightness. It appears that two nearest Mn (Ni) atoms at the surface tend to attract. The height difference between 1 and 2 (2 and 3, 3 and 4) measured from the STM image is about 0.15 Å. However, these values cannot be simply treated as the real height of the atoms because STM measures the charge density at the surface. From topographic image, one cannot distinguish between Mn and Ni. The lateral positions of the atoms extracted from Fig. 5.7 (a) are given in Fig. 5.7 (b). The central atom in square II moved away
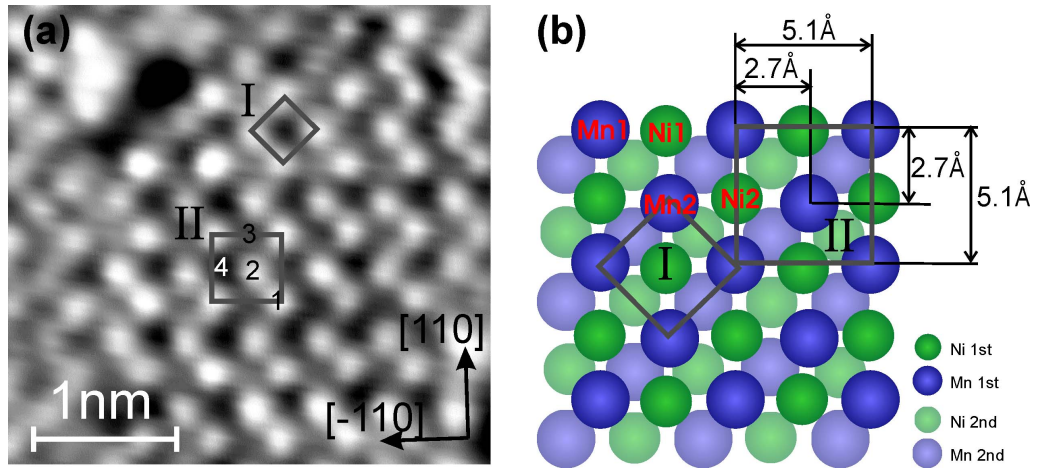
Figure 5.7: (a) Atomically resolved image of 14.7 ML NiMn on Cu(001). Square I marks the $c(2 \times 2)$ unit cell which originates from the chemical order of NiMn surface. Square II represents a $p(2 \times 2)$ structure which comes from the difference between surface Mn (Ni) atoms. 1, 2, 3 and 4 indicates four inequivalent sites at the surface. U_{bias}=20 mV, $I_t = 3$ nA. (b) Lateral positions of the surface atoms extracted from (a). Square I and II mark the unit cell corresponding to (a). Mn1, Mn2, Ni1, Ni2 represent Mn and Ni atoms of the inequivalent sites on the surface. Only the positions of the bright dots in (a) were measured which correspond to either Mn or Ni. The inner layer of NiMn is also drawn to show the broken symmetry of the surface. The error bar of these values is around 0.05 Å.

from the center of square II by about (0.15 Å, 0.15 Å) to the right-bottom corner. Due to the two-fold symmetry of the NiMn films, the shift parallel to the Mn sheets or perpendicular to the Mn sheets are not equivalent. It cannot be determined from the STM images. These questions will be answered later in this section with the LEED-IV measurements.

Square II in Fig. 5.7 represents a $p(2 \times 2)$ superstructure in real space which was not observed on as grown films with LEED. The $p(2 \times 2)$ spots appeared in the LEED pattern when the sample was annealed to 350 K as shown in Fig. 5.8 (b). The $p(2 \times 2)$ spots were much weaker than the $c(2 \times 2)$ spots. As a comparison, Figure 5.8 (a) gives the LEED pattern of NiMn film without annealing where only $c(2 \times 2)$ spots were observed. Since from the STM image, the $p(2 \times 2)$ superstructure was already observed in the NiMn films without annealing(cf. Fig. 5.7 (a)), the appearance of the $p(2 \times 2)$ spots in the LEED pattern was considered as the reduction of the background. Figure 5.9 gives the morphology of 8.4 ML NiMn films after annealing to 350 K which proved that the films were much smoother. The orientation of the islands was the same as in Fig. 5.4 while the size of the islands increased.

The origin of $p(2 \times 2)$ structure is unclear, yet. It has been found by Wuttig et al. [107] that a Mn rich surface of NiMn on Ni(001) gave a metastable $p(2 \times 2)$ superstructure. The lattice constant of Ni is 3.52 Å, only 2.8% smaller than Cu. The
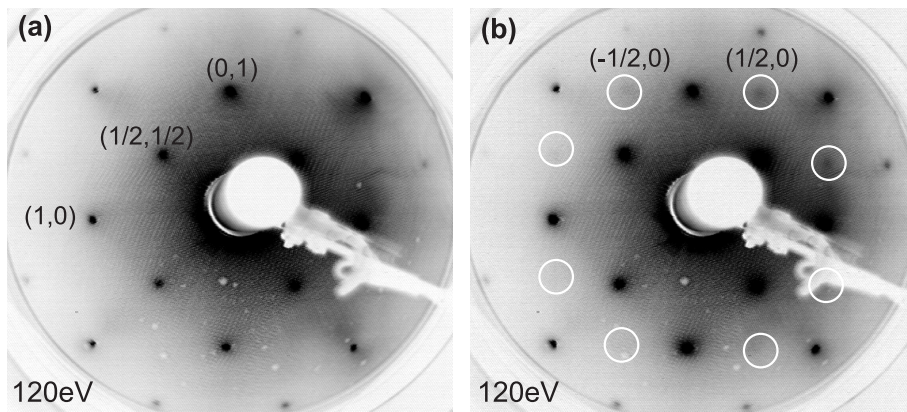
Figure 5.8: LEED pattern of 8.4 ML NiMn on Cu(001). (a) as deposited, only $c(2 \times 2)$ spots were observed. (b) after annealing to 350 K. Weak $p(2 \times 2)$ spots appeared as indicated in the image. The pattern was over exposed to visualize the $p(2 \times 2)$ spots. The positions of $p(2 \times 2)$ spots are marked with white circle. Due to the inhomogeneity of the LEED screen, only a few of them are clearly visible.

study of NiMn/Ni(001) done by Wuttig et al. [106] showed very similar properties as NiMn/Cu(001). Due to the inhomogeneity of NiMn films which cannot be avoided in co-evaporation, locally Ni or Mn rich areas are possible. The Mn rich surface may give a $p(2 \times 2)$ superstructure. However, the STM image (cf. Fig. 5.7 (a)) showed equal amount of Ni and Mn atoms in the $p(2 \times 2)$ superstructure. It is also possible that the $p(2 \times 2)$ superstructure comes from chemical or magnetic interaction between surface Mn (Ni) atoms. The dangling bonds of Mn atoms at the surface tend to form dimers as has been shown in the previous chapter. The interaction between surface atoms may change the position of the surface atoms. The large buckling (0.3 Å) of surface atoms in NiMn thin films on Ni(001) [106] was at-
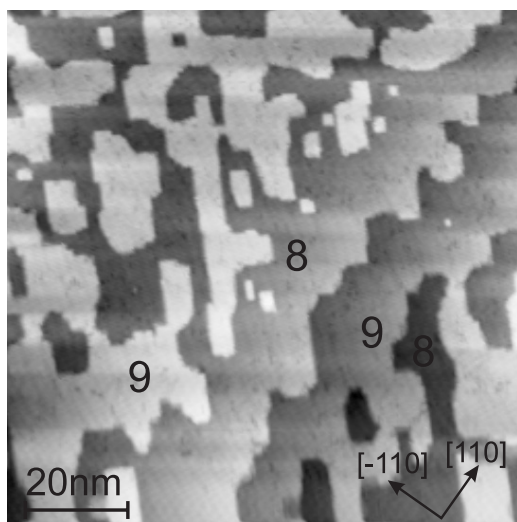

Figure 5.9: Topography of 8.4 ML NiMn on Cu(001) after annealing to 350 K. The tunneling current was 3 nA and the gap voltage was 0.5 V. The 8th and 9th layers are indicated in the image. The image is slightly distorted due to drift.

58

tributed to the large magnetic moments of Mn atoms. It is possible that lateral shifts of the atoms shown in Fig. 5.7 (a) also originate from the magnetic interaction. This will be further discussed later in this Chapter.

LEED-IV measurements

From STM and LEED observations, the lateral positions of the atoms can be determined while the normal positions are still unknown. A buckling of surface atoms was observed in STM. As STM measures the local density of states, the buckling can have chemical origin or can be due to a displacement. In order to solve this problem, LEED-IV measurements and simulation were done for NiMn thin films (see Fif. 5.10). In the UHV chamber described in Chapter 3, it was not possible to achieve normal incidence of the electron beam which is critical in LEED-IV measurements. Therefore, the LEED-IV measurements were performed in another UHV chamber equipped with LEED, MEED and AES. NiMn films thicker than 12 ML were grown. The sample was cooled down to 150 K during the LEED-IV measurements to decrease the background intensity. The LEED-IV simulations were done by Dr. Aimo Winkelmann.
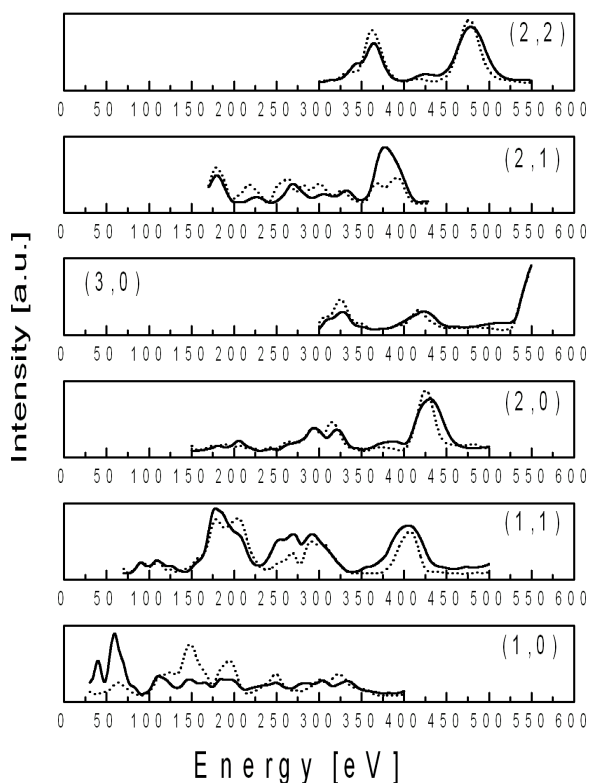

Figure 5.10: LEED-IV curves of NiMn films. Solid line: the experimental results, dotted line: the calculated curves.

In the simulations, the contribution of underlying Cu atoms was omitted. This is reasonable as the NiMn film was much thicker than the electron penetration depth. In the first step, only a $c(2 \times 2)$ surface reconstruction was considered. The in-plane lattice was fixed to the value of Cu(001) which reduced the computation time significantly. Mn and Ni atoms were moved independently normal to the surface. The agreement between calculations and experimental results was not satisfying. The R factor, which gives the deviation between the normalized experimental and theoretical intensity spectra, was as high as 0.5. Later, special care was taken for the first two NiMn layers. A $p(2 \times 2)$ surface reconstruction was considered which means that the two nearest Mn (Ni) atoms on the surface (and the second layer) were allowed to move independently in all three dimensions. Figure 5.10 gives the experimental I-V curves together with the calculated curves. The R factor decreased to 0.36. The calculated results are given in Fig. 5.11. Figure 5.11 (a) shows the lateral positions of the surface atoms. In the $p(2 \times 2)$ unit cell as marked with square II, the Mn atom in the center moves toward the right-bottom corner, i.e., the Mn atom moves out of the Mn sheet. The Mn atoms at the corners of square II do not move with respect to the second layer. No lateral deviation of Ni atom from $c(2 \times 2)$ structure was found. Figure 5.11 (b) gives the vertical positions of atoms. In the first layer, the Mn atoms are higher than the Ni atoms. The Mn atoms at the surface can be divided into two groups with a vertical distance of 0.21 Å. Correspondingly,
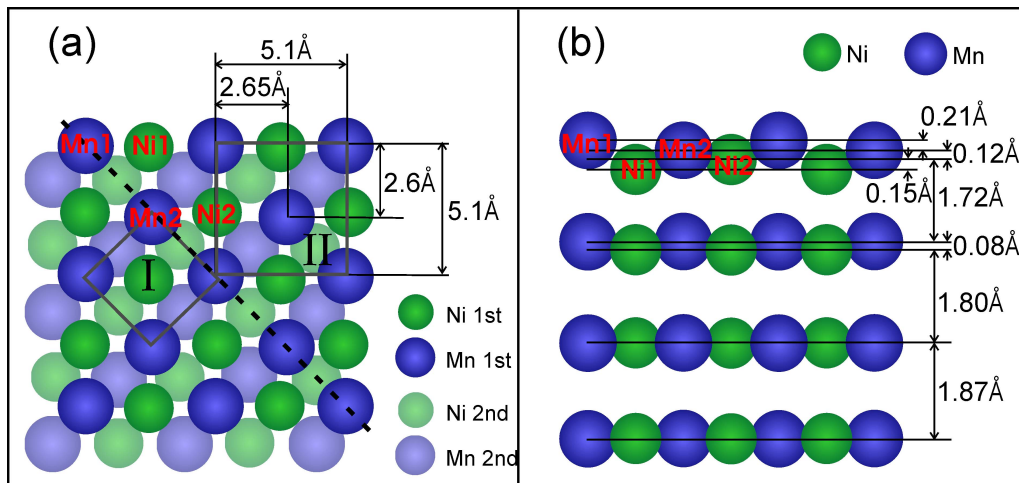

Figure 5.11: (a) Lateral positions of Mn and Ni surface atoms deduced from LEED I-V simulations. The shift of the Mn atoms in the surface plane results in a $p(2 \times 2)$ superstructure. $c(2 \times 2)$ and $p(2 \times 2)$ unit cells are marked by the gray square I and II. Two layers of NiMn are drawn to show the NiMn sheets perpendicular to the surface. (b) Vertical positions of Mn and Ni atoms (cut plane as shown by the black dotted line in (a)). A large buckling with Mn atoms sticking out with respect to the Ni atoms was found. Two nearest Mn (Ni) atoms of the surface layer have different normal positions which reflect the $p(2 \times 2)$ symmetry. Mn1, Mn2, Ni1, Ni2 represent Mn and Ni atoms of the inequivalent sites on the surface.

60

the Ni atoms are also divided into the two groups with a distance of 0.15 Å. The lower Mn is higher than the upper Ni by 0.12 Å. The bucking between Ni and Mn is propagating to the second layer where Mn is higher than Ni by 0.08 Å. The distance between the first layer and second layer (also the second layer and third layer) is different from the distance between other atomic layers. From the fourth layer on, the layer height is constant (1.87 Å). The volume of fcc unit cell of the NiMn thin films (3.62 Å$\times$ 3.62 Å$\times$ 3.74 Å$=$ 49.01 Å^3) is almost the same as the bulk (3.74 Å$\times$ 3.74 Å$\times$ 3.52 Å$=$ 49.24 Å^3).

Comparing the LEED-IV and STM results, one sees a nice agreement. First, if we assume that the bright dots in Fig. 5.7 (a) are Mn atoms, the lateral shift of Mn from the central position of $p(2 \times 2)$ is (0.15 Å, 0.15 Å). The result from LEED-IV is (0.06 Å, 0.10 Å). The values determined from STM images are larger than the LEED-IV results. At this point, we need to consider the error bars in STM and LEED-IV measurements. In the STM images, the positions are the maxima of the charge density. This interpretation has its drawbacks because the highest charge density does not necessarily represent the center of the atom. The error bar is around 0.05 Å in the determination of the position of the atoms from the STM image. The error bar in the LEED-IV calculations is evaluated by the change of the *R*-factor as a function of the structural parameters. The error bar is mostly below 0.05 Å. The different shift vectors measured with STM and LEED-IV therefore agree within the error bars. Thus, LEED-IV calculation confirmed the presence of $p(2 \times 2)$ superstructure. It gives the layer spacing of NiMn thin films and shows that Mn atoms stick out with respect to Ni atoms. These structural data were used in the calculation of spin structure of NiMn thin films.

In this section, we discussed the growth and structure of NiMn thin films on Cu(001). The structure was determined with the LEED-IV and STM measurements. Besides the $c(2 \times 2)$ superstructure which arises from the chemical order, an additional $p(2 \times 2)$ superstructure was observed in STM and confirmed by combined LEED-IV measurements and calculations. The origin of the $p(2 \times 2)$ superstructure is unclear. From the chemical order, there is no symmetry breaking that leads to a $p(2 \times 2)$ unit cell. A possible reason is the magnetic interaction of the atoms. In the following section, the magnetic properties of the NiMn will be discussed.

5.3 Magnetic properties of NiMn on Cu(001)

The onset of antiferromagnetism of NiMn thin films on Cu(001) at room temperature is around 8 ML as has been demonstrated by XMCD-PEEM and MOKE measurements on Co/NiMn bilayers [109]. The spin structure of NiMn thin films remained unclear. The NiMn surface was studied on the atomic scale in our experiments with spin-polarized scanning tunneling microscopy.

5.3.1 Spin contrast between Mn and Ni

In our experiments, no spin contrast was observed between neighboring terraces in the bias voltage interval from -1 V to 1 V. As has been discussed in Chapter 2, there are two kinds of antiferromagnetic surfaces: compensated and uncompensated surfaces. For an in-plane uncompensated surface, spin contrast between atomic layers should be observable. Thus, at least the in-plane components of the spin polarization of NiMn is compensated in the energy interval from -1 V to 1 V.
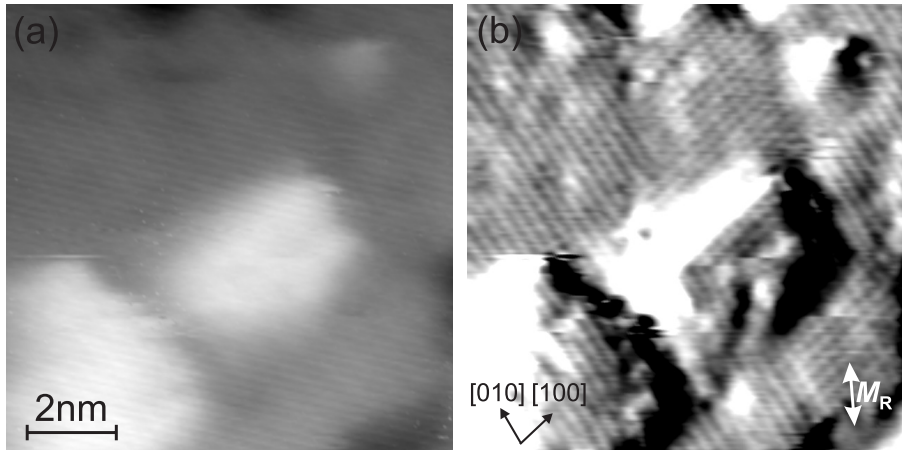

Figure 5.12: Topography (a) and corresponding spin image (b) of 8.1 ML NiMn films on Cu(001). The crystalline orientations are indicated in the image. M_R gives the magnetization direction of the ring. U_{bias}=0.5 V, $I_t = 3$ nA.
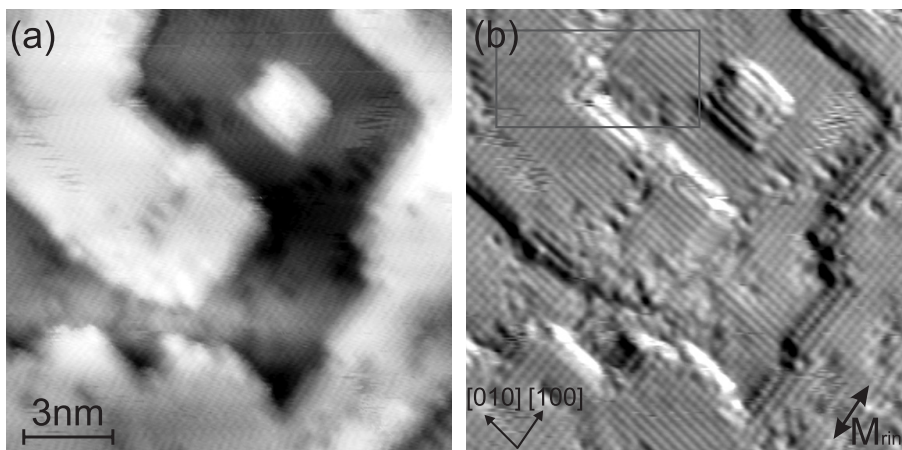

Figure 5.13: Topography (a) and corresponding spin image (b) of 10.5 ML NiMn films on Cu(001) after annealing to 350 K. The marked area is shown in Fig. 5.14 (a). The crystalline orientations are indicated in the image. M_{Ring} gives the magnetization direction of the ring. U_{bias}=0.5 V, $I_t = 3$ nA.

Two kinds of films have been studied: One was grown at room temperature, the other was grown at room temperature and then annealed to 350 K. STM studies have shown that the only difference between these two kinds films was that the surface is smoother after annealing. Sp-STM measurements confirmed the similarities between the as-deposited and annealed NiMn films. No difference was observed in the spin signal from these two kinds of films.

Figure 5.12 gives the topography and spin image of 8.1 ML NiMn films. The magnetization of the ring was arranged almost parallel to [110] direction of the crystal. The accuracy of the alignment was within $\pm 10°$. In the topographic image, the surface is characterized by flat terraces (gray) with atomic height islands (white) of about 2 nm in width. In the spin image, parallel lines running along the [010] and [100] were observed. The details of these features were more clearly seen on the annealed surfaces.

After annealing to 350 K, the film was much smoother. The topography and corresponding spin signal are given in Fig. 5.13. In the topography, the image is
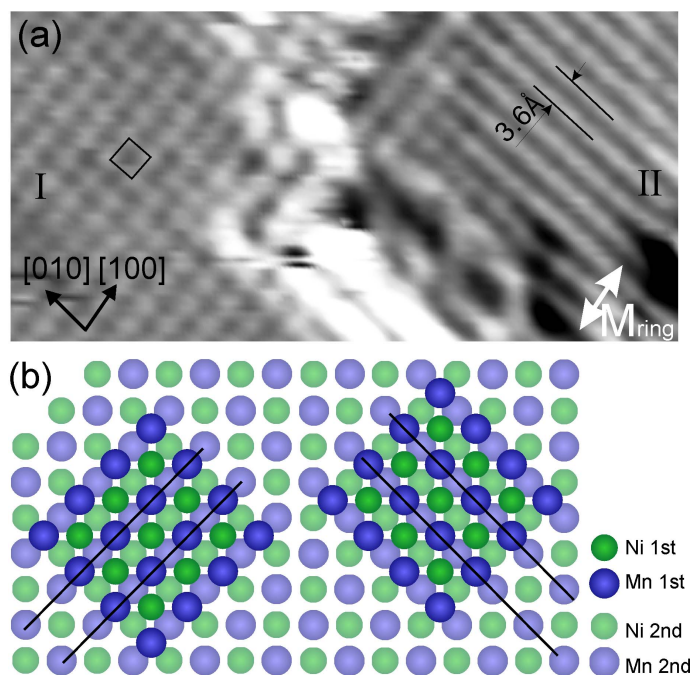

Figure 5.14: (a) Spin image of 10.5 ML NiMn films on Cu(001) after annealing to 350K. Two patterns are indicated in the image. Pattern I shows a square lattice of $3.6\,\text{Å} \times 3.6\,\text{Å}$. Pattern II is more stripe-like. The distance between the stripes in is $3.6\,\text{Å}$. M_{Ring} gives the magnetization direction of the ring. (b) Schematic explanation of the origin of two domains of NiMn film. The different spin patterns arise from the different orientations of the two structural domains relative to the magnetization direction of the ring. The black lines indicate the Mn (Ni) sheets perpendicular to the surface which lead to a 2-fold symmetry of NiMn films.
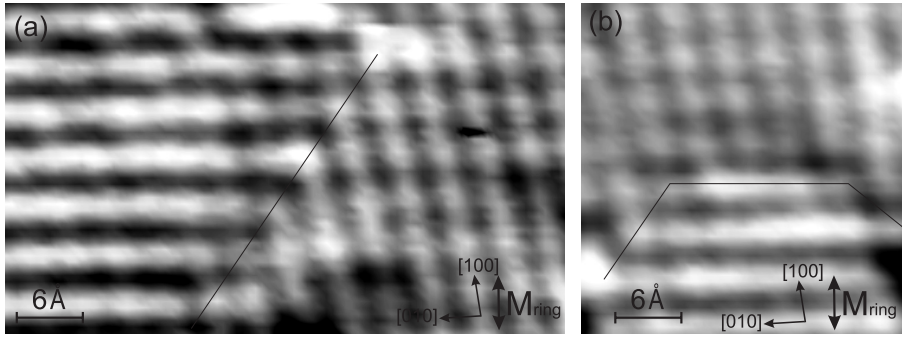
Figure 5.15: Spin image of 10.5 ML NiMn films on Cu(001). Domain walls running along [110] (a) and [100] (b) directions are marked by the black lines. The crystalline orientations are indicated in the image. M_{Ring} gives the magnetization direction of the ring.

characterized by NiMn terraces with step edges along [010] and [100] directions. In this case, the magnetization of the ring was set parallel to the [100] direction of the crystal. Two different patterns were observed which are more clearly visible in the enlarged image in Fig 5.14 (a). In the left part of Fig. 5.14 (a), the spin image shows a square lattice. The size of the lattice as indicated in the image is $3.6\,\text{Å} \times 3.6\,\text{Å}$ which is exactly the size of the chemical unit cell. In the right part of the image, the pattern looks more like parallel stripes. The distance between stripes is 3.6 Å. The spin unit cell overlaps with the chemical unit cell. The spin contrast can be attributed to the difference between Ni and Mn atoms, i.e., Ni and Mn show different spin polarization. The two different patterns observed in the spin channel correspond to two structural domains of NiMn depending on the orientations of the Mn (Ni) sheets. These two structural domains are perpendicular to each other as shown in Fig. 5.14 (b). The two domains are expected to have the same spin structure due to the four fold symmetry of the Cu substrate. Depending on their relative orientations to the magnetization direction of the ring, two different spin patterns were observed in the Sp-STM measurements. One is more square like (Pattern I) and the other is more stripe like (Pattern II). The two different patterns imply a noncollinear spin structure of the NiMn surface. Although the surface layer has a four-fold symmetry, it is broken to a two-fold symmetry due to the Ni and Mn sheets. The stripe pattern reflects the local two-fold symmetry of the film.

Since there are two structural domains of NiMn films, the natural question about the size of the domains and the width of domain walls arises. As can be seen from Fig. 5.12 and 5.13, the domain size is between 5 and 10 nm in width. The annealing procedure did not change the size of the domains. The domains are usually separated by disordered regions where aggregation of Ni or Mn may happen. In some cases, a continuous change between domains was also observed as shown in Fig. 5.15. The domain walls run along [1$\bar{1}$0] or [010] directions. The transition is within one lattice constant which suggests the formation of domain walls are mainly due to the structural change. The appearance of domain walls was always accompanied

by the structural domains. We never observed a pure magnetic domain wall, i.e., no domain wall was present within one structural domain. This is consistent with the fact that domain walls are unfavorable in antiferromagnetic materials [112].

5.3.2 Two dimensional vector map of the spin polarization

If a magnetic structure similar to bulk NiMn is assumed for NiMn thin films on Cu(001), Mn atoms of neighboring atomic layers couple antiferromagnetically while Ni moments almost vanish. The assumption is confirmed with *ab-initio* calculations which will be discussed later in this Chapter. Sp-STM measures the spin polarization of the surface layer. It cannot directly give information of the inner layers. Since the magnetic structure of the surface layer follows that of the inner layers, we expect that the spin contrast is reversed between neighboring terraces on the surface. In the following discussion, a compensated surface was assumed. Thus, Ni and Mn show equal but opposite spin polarization on one terrace.
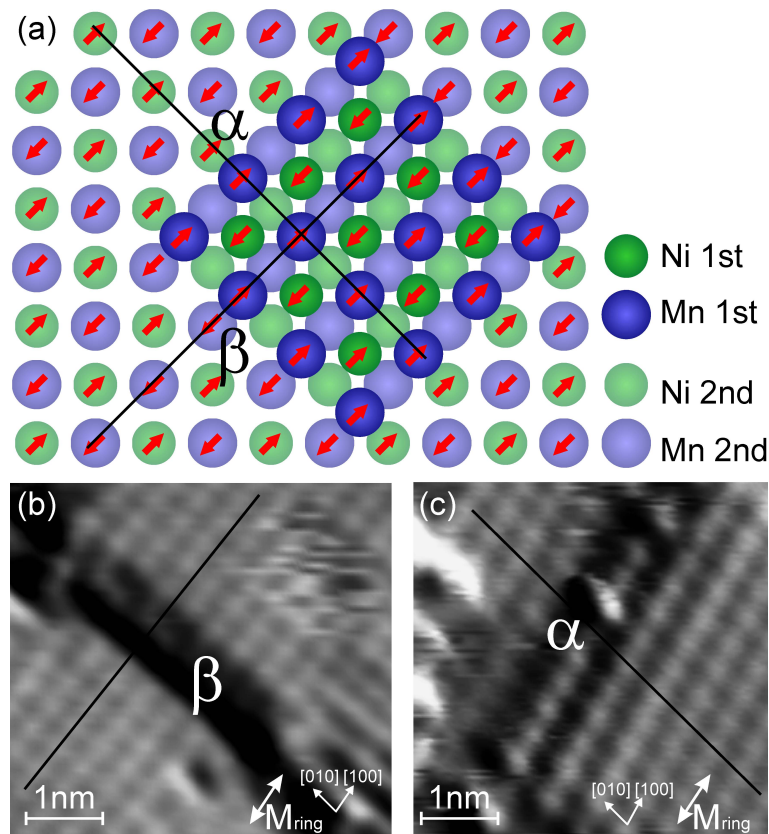

Figure 5.16: (a) Schematic diagram of two kinds of steps. The red arrows represent the measured spin polarization of the atoms along the ring direction. Two different steps are marked as α and β. (b) and (c) are STM observations of α and β steps.

65

In the case of pattern I as shown in Fig. 5.16 (b), when the step runs along [010] direction, the spin contrast is shifted by half of the spin unit cell as indicated by the black line. The black line is on the bright dots on the lower terrace while it is in between the bright dots on the upper terrace. When the step runs along [100] direction (cf. Fig. 5.16 (c)), the black line is on the bright dots on both sides of the step edge. The structural orientation can be determined by comparing the behavior of the spin contrast at step edges with the antiferromagnetic spin structure of NiMn as shown in Fig. 5.16 (a). The spin polarization is reversed between the first and the second layer as a consequence of antiferromagnetic coupling of nearest Mn atoms. There are two kinds of steps. One is defined as step α where the step is parallel to the Mn (Ni) sheets. As indicated by the black line, the spin polarization of the atoms in the line are pointing to one direction on both sides of the step edge. The other is defined as step β where the step is perpendicular to the Mn (Ni) sheets. As indicated by the black line, the spin polarization of the atoms in the line are pointing to opposite direction on two sides of the step edge. Step β is consistent with Fig. 5.16 (b) and step α is consistent with Fig. 5.16 (c). Thus, it can be concluded in the case of pattern I, the magnetization of the ring is parallel to the Mn (Ni) sheets.
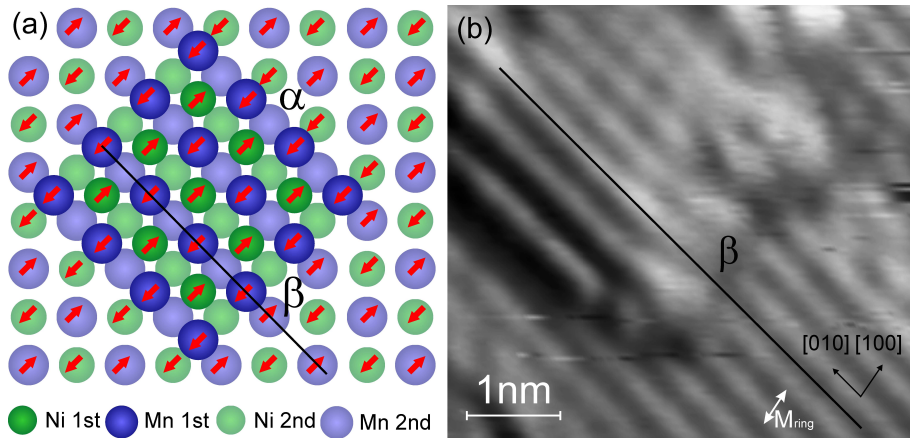

Figure 5.17: (a) Schematic diagram of two kinds of steps. The red arrows represent the measured spin polarization of the atoms along the ring direction. Two different steps are marked as α and β. (b) STM observations of step β.

A similar analysis can also be done for the case of pattern II. Again, at the step β (cf. Fig. 5.17 (a)), the spin contrast is shifted by half of the $c(2 \times 2)$ unit cell which corresponds to a step running along the [100] direction as experimentally observed in Fig. 5.17 (b). Step α is not shown because the position of the atoms were not clearly distinguishable along the stripe pattern. In the case of pattern II, the magnetization of the ring is perpendicular to the Mn (Ni) sheets.

The two structural domains as shown in Fig. 5.14 (c) are considered to have the same spin structure. The two different patterns observed in the spin image actually give two orthogonal components of one domain as the substrate itself is of four-fold

symmetry. In our experiments, the change of tunneling current upon the reversal of tip magnetization was measured which is defined as the spin polarization of the tunneling current. Our Sp-STM images show the relative magnitude of the spin polarization between Ni and Mn. The offset, or zero spin polarization cannot be directly determined from the Sp-STM images. Since the surface of the NiMn films is compensated, the zero point can be assumed as the average value. Thus, a two dimensional vector map of spin polarization can be drawn in the way as has been discussed in the previous Chapter. Figure 5.18 (a) and (b) are rescaled to the zero
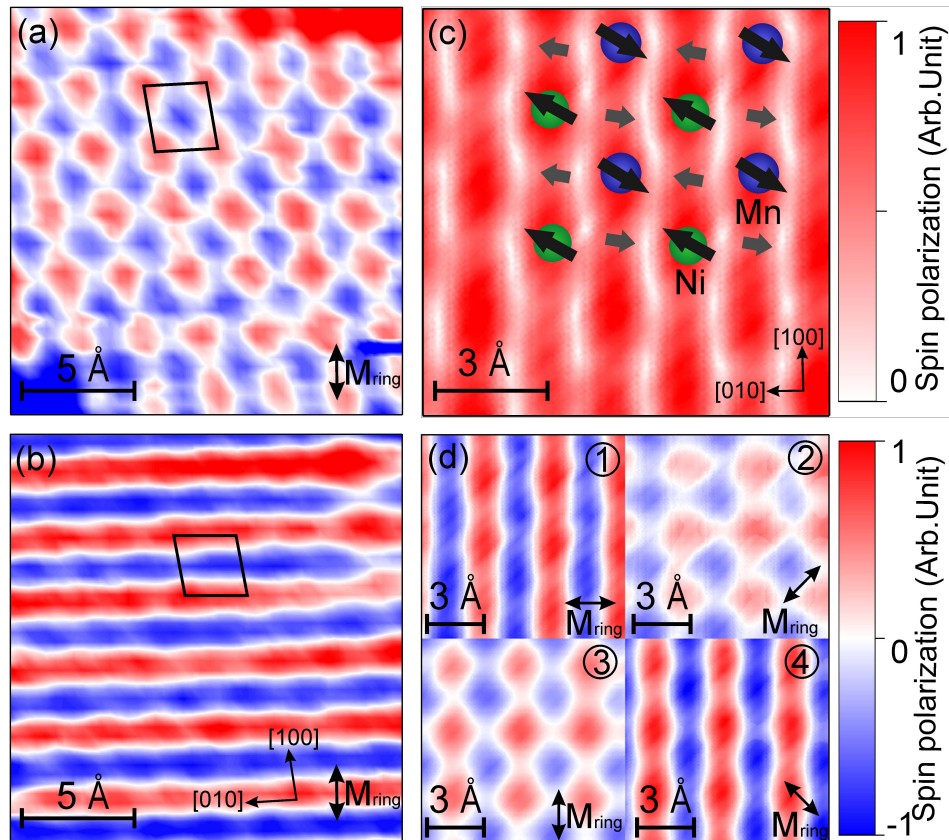

Figure 5.18: (a) and (b) are spin images of two domains cut from one larger image. The images are rescaled to the zero spin polarization. The black parallelogram shows the spin unit cell of the surface. It should be square. The deviation from square was due to drift. The crystalline orientations are indicated in the image. M_{Ring} gives the magnetization direction of the ring. (c) The red-white coded background represents the magnitude of the spin polarization calculated by combining image (a) and (b). (b) is rotated by 90° to fit with (a). The Mn (Ni) sheets are parallel to [100] direction. The drift was corrected. The magnitude and directions of the spin polarization of the surface atoms are indicated by the black arrows. The gray arrows represent the magnitude and directions of the spin polarization of the four-fold hollow sites. (d) shows the calculated spin image from (c) with four different ring orientations as indicated by 1, 2, 3, and 4.

67

spin polarization. The ring was arranged parallel to the [100] direction. (a) and (b) were cut from one image such that the tip can be treated as unchanged. Figure 5.18 (c) gives the magnitude after combining image (a) and (b) together. The arrows attached to the atoms show the magnitude and directions of spin polarization of surface atoms. Since the directions and magnitude of the spin polarization of the surface are known, the spin images with various ring orientations can be calculated as well. Figure 5.18 (d) gives the image with the ring parallel to $[0\bar{1}0]$, $[1\bar{1}0]$, [100] and [110] as indicated by 1, 2, 3 and 4, respectively. 1 and 3 correspond to Fig. 5.18 (b) and (a). 2 and 4 agrees well with Fig. 5.12.

Two notes should be made for the vector map of spin polarization. First, the surface Mn and Ni atoms have an almost collinear spin structure. It has a preferential magnetic axis along $[\bar{1}10]$ direction which differs from the bulk NiMn spin structure. In the bulk, the magnetic axis lies in the Mn sheet, i.e., either along [010] (in-plane) or along [001] (out-of-plane). At this stage, we do not know if the reorientation of the magnetic axis happens only at the surface or in the whole films. Second, in the vacancy positions of the surface, as marked by the gray arrows in Fig. 5.18 (c), the surface shows opposite spin polarization as well. There are no atoms belonging to the surface layer at these positions. The spin-polarized states in these positions are related to the subsurface atoms. These states reflect the two-fold symmetry of the NiMn thin films.

5.4 Discussion: magnetic interaction of the surface layer

Depending on the orientation of the Mn sheets with respect to the ring, the NiMn domains can be characterized as pattern I and II as shown in Fig. 5.14 (a). They reveal the $c(2 \times 2)$ symmetry of the surface and the two-fold symmetry of NiMn. In the atomically resolved topography and LEED observations, a $p(2 \times 2)$ super-structure was observed as well. The origin of that reconstruction is not clear, yet. If it is related to the magnetic interaction between the surface atoms, the symmetry should also be visible in the spin image. In the above discussion, the spin-polarized measurements were done at a bias voltage of 0.5 V. Only a $c(2 \times 2)$ unit cell was observed at this voltage in the spin images.

5.4.1 Voltage dependence of the spin contrast

A magnetic unit cell of $p(2 \times 2)$ size was observed when the bias voltage was changed. Figure 5.19 gives the voltage dependent spin images. The images of the upper and middle rows show the evolvement of pattern I and pattern II with the bias voltage, respectively. The images were taken successively with the same tip. The
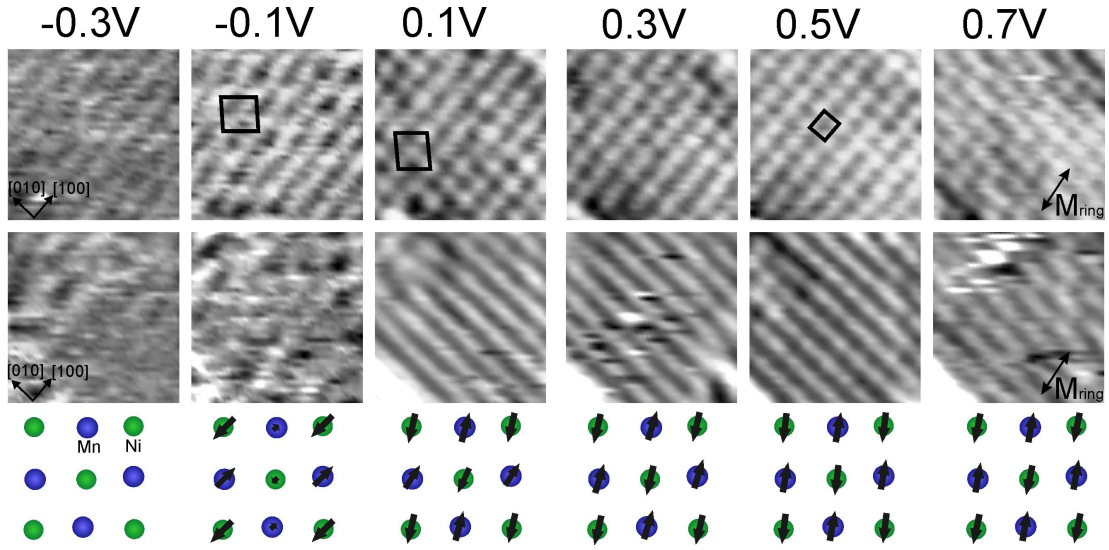
Figure 5.19: Upper row: voltage dependent spin images of pattern I where the ring is parallel to the Mn (Ni) sheets. A $c(2 \times 2)$ unit cell is indicated in the image taken at 0.5 V. A $p(2\times2)$ unit cell is indicated in the images taken at -0.1 V and 0.1 V. Middle row: voltage dependent spin images of pattern I where the ring is perpendicular to the Mn (Ni) sheets. The tunneling current was kept constant at 3 nA. The size of the images are 3 nm × 3 nm. The M_{Ring} gives the orientation of the ring. Lower row: configuration of spin polarization at different voltages. No configuration is drawn at -0.3 V due to the weak spin contrast. The length of the arrows at the same voltage are only comparable at the same bias voltage.

images of the two domains at the same bias voltage were cut from one large image. For pattern II (middle row of Fig. 5.19), where the ring is perpendicular to the Mn (Ni) sheets, no spin contrast was observed at negative voltages. At positive voltages, stripe patterns were observed. The contrast changes slightly with the voltage, but the pattern stays the same. As to the pattern I (upper row of Fig. 5.19), where the ring is parallel to Mn (Ni) sheets, the voltage dependent behavior is more complex. Between 0.3 V and 0.7 V, a $c(2 \times 2)$ unit cell was observed. At 0.1 V, the $c(2 \times 2)$ symmetry is slightly broken and a $p(2 \times 2)$ unit cell appears. As marked by the black square in the image, the central dot is weaker than the dots in the corners. At -0.1 V, the $c(2 \times 2)$ unit was not visible any more and the image is dominated by the $p(2 \times 2)$ unit cell. At even lower voltage, the $p(2 \times 2)$ cell disappeared. The images show a weak stripe pattern running parallel to the magnetization direction of the ring at negative bias voltages. The appearance of $p(2 \times 2)$ symmetry in the images agrees with the structural observation. It suggests that magnetic interaction is responsible for the $p(2 \times 2)$ symmetry, i.e., the lateral displacement of surface Mn atoms as shown in Fig. 5.7.

The magnitude and directions of spin polarization of the surface atoms can be plotted for different voltages as shown in the lower row of Fig. 5.19. The vectors were obtained by combining the two orthogonal measurements from above. At positive

69

voltage, a nearly collinear configuration was observed with magnetic axis along [110] direction. At 0.1 V, the structure deviates from a collinear configuration. The magnitude of spin polarization is also slightly different between the two Mn atoms in the $p(2 \times 2)$ unit cell (the same holds for Ni moments). At -0.1 V, the magnetic axis is along [100] direction. The magnitude of spin polarization between Mn (Ni) atoms are different. The change of the direction of spin polarization below the Fermi edge implies a noncollinear spin polarization within one atom. This can be due to spin-orbit interaction between the bands of opposite spin. The change of spin unit cell from well ordered $c(2 \times 2)$ to $p(2 \times 2)$ goes hand-in-hand with the non-collinearity of the spin structure of NiMn surface.

As has already been discussed in Chapter 2, in the spin-polarized STM measurements, the measured quantity is the spin polarization of the tunneling current which depends on properties of the tip, the sample and the tunneling barrier. In vacuum tunneling, the tunneling barrier can be treated as constant. The spin polarization of the STM tip is treated as constant as well within the Tersoff-Hamann approximation [37, 38]. Thus, the spin polarization of the tunneling current reflects the properties of the sample. It is proportional to the spin polarization of the integrated density of states from the Fermi level to eV (V is the bias voltage). A voltage dependence of spin contrast was reported by a few groups in different systems [113, 114]. The interpretation is based on the spin-polarized electronic structure of the systems investigated. In order to understand the energy dependence of the spin contrast, *ab-initio* calculations were carried out for NiMn thin films on Cu(001).

5.4.2 *Ab-initio* local spin-density calculations

The electronic structure of NiMn films were computed from first principle using local spin-density approximation of density-functional theory with Perdew-Wang exchange-correlation potential [115]. The scalar-relativistic Korringa-Kohn-Rostoker (KKR) method was applied to a semi-infinite system, hence taking into account the appropriate boundary conditions of the surface [116]. The calculations were done by Dr. Arthur Ernst.

The structural model given by the LEED-IV and atomically resolved STM observation as discussed before was adopted in the calculation. 6 ML NiMn on Cu(001) and a $p(2 \times 2)$ unit were considered. The lateral positions of the atoms were taken from the STM measurements (cf. Fig. 5.7 (b)). The vertical positions of the atoms were adopted from the LEED-IV measurements (cf. Fig. 5.11 (b)). The error bars in the structural measurements were considered in the *ab-initio* calculations and did not influence the results considerably.

The calculations show that the antiferromagnetic phase is energetically more favorable than the ferromagnetic phase. Nearest Mn atoms couple antiferromagnetically and second nearest Mn atoms couple ferromagnetically which is consistent with
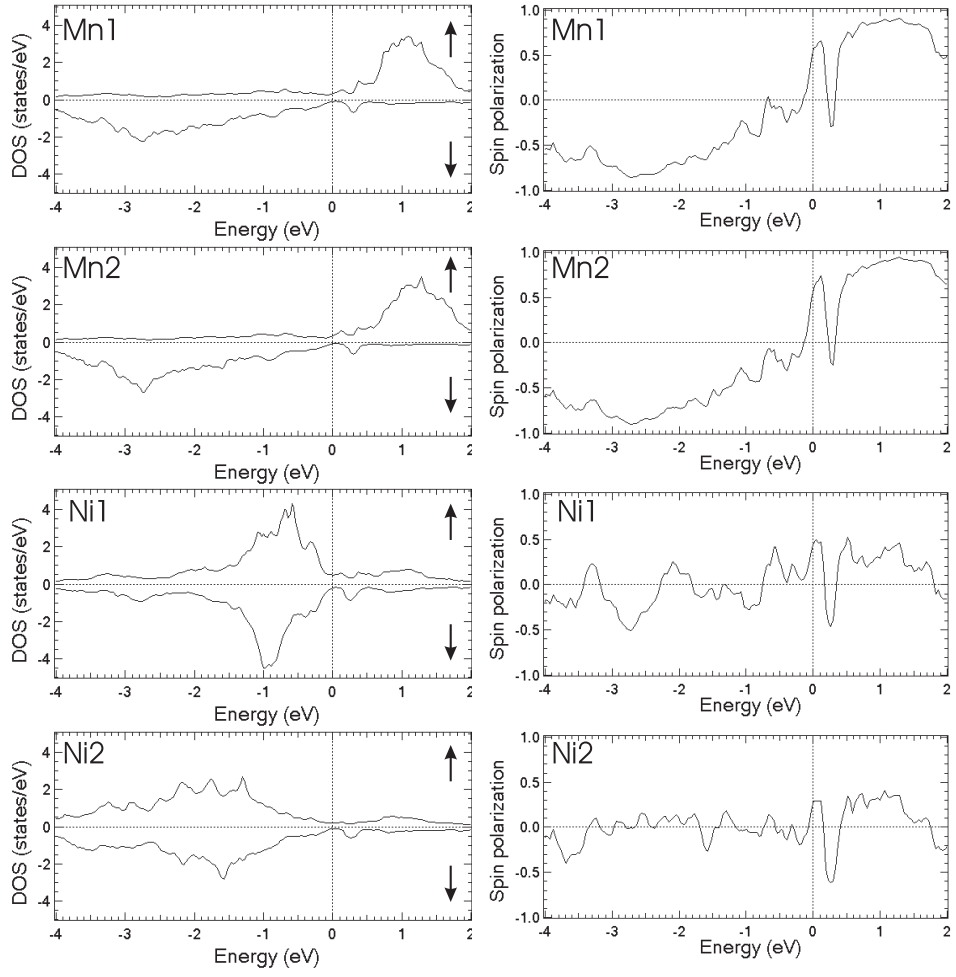
Figure 5.20: Density of states (left) and spin polarization (right) of NiMn surface. The atomic species (Mn1, Mn2, Ni1, Ni2) are indicated in the figure. The labeling of the atoms is identical to Fig. 5.11.

the spin structure of bulk NiMn. The magnetic moment of Mn are as large as 3.8 μ_B while the Ni moments almost vanish (<0.05 μ_B) in the NiMn films. The total energy of the films of $p(2 \times 2)$ symmetry was found to be lower than that of $c(2 \times 2)$ terminated films indicating that the observed reconstruction lowers the energy of the film. Since the $p(2 \times 2)$ symmetry is considered at the surface, there are two different Mn (Mn1 and Mn2) and two different Ni (Ni1 and Ni2) atoms at the surface. Figure 5.20 gives the density of states and spin polarization of these four different atoms at the surface. Interestingly, at the surface the Ni moments do not vanish. The magnetic moments of Ni1 (0.30 μ_B) is much larger than that of Ni2 (0.08 μ_B). The magnetic moments of Mn1 (3.69 μ_B) and Mn2 (3.91 μ_B) are slightly different. Though the magnetic moments of Mn is much larger than Ni at the surface, the calculated spin polarization of Mn and Ni are comparable close
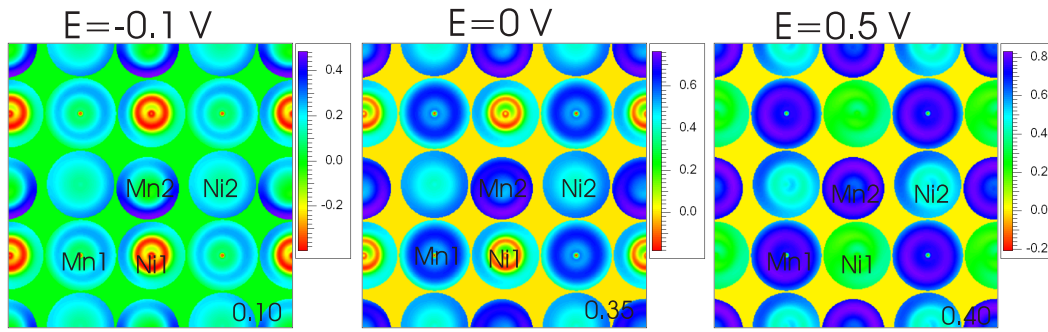
71

Figure 5.21: Local spin polarization of the surface layer in real space at the energy of -0.1 eV, 0 eV and 0.5 eV. The numbers in each image give the net spin polarization at this energy.

to the Fermi edge. The density of states (DOS) and spin polarization of Mn1 and Mn2 close to the Fermi edge are nearly the same. The DOS and spin polarization of Ni1 and Ni2 differs a lot below the Fermi level but are nearly identical above the Fermi level. In the voltage dependent spin-polarized measurements, at negative voltages from -0.3 V to -0.1 V, the spin contrast is very weak. This agrees with the small spin polarization of both Ni and Mn below the Fermi edge. At -0.1 V, a $p(2\times2)$ unit cell was observed. This comes from the difference of spin polarization between Ni1 and Ni2 close to the Fermi edge. At positive bias voltages from 0.1 V to 0.7 V, a high spin contrast between Ni and Mn was obtained which gives the $c(2\times2)$ unit cell. This agrees with the highly spin-polarized states of both Mn and Ni above the Fermi level. The change of spin unit cells agrees with the calculated spin polarization image of the surface. Figure 5.21 plots the spin polarization of the surface atoms at different energy at the position of the atoms in real space. In the calculations, a spherical potential was assumed for the atoms. Thus, in the vacancy positions at the surface, no electrons are present. It reflects the four-fold symmetry of surface, but cannot reveal the 2-fold symmetry of the films. At -0.1 V, Ni1 shows a high spin polarization which gives the $p(2\times2)$ unit cells. At 0.5 V, the spin images are dominated by the $c(2\times2)$ unit cells.

Despite all these agreements between the theoretical and experimental results, there are a few discrepancies. First, the calculations show a net spin polarization arising from the surface which means a layer-wise spin contrast should be visible in the spin image. However, the experiments give a compensated surface at an energy interval from -1 V to 1 V. Second, the calculations (cf. Fig. 5.20) show that both Ni and Mn atoms have highly polarized states above the Fermi edges. Ni and Mn couple ferromagnetically, i.e., the spin polarization of Ni and Mn has the same sign. The experimental results suggest that Ni and Mn have opposite spin polarization. The disagreement between experimental results and theoretical calculations have two possible reasons. First, in the calculations, the spin-orbit coupling is not included. The direction of the spin polarization is not known. Possibly, at the surface, Mn moments are tilted toward the [110] direction or even out-of-plane, Ni

72

moments lie in the surface plane, such that they compensate the in-plane component of the Mn moments. The spin structure of the surface layer can be similar to the 3-Q spin structure of antiferromagnetic fcc crystals, for example, FeMn. In the FeMn/Cu(001) system [34, 31], the in-plane magnetic moments are totally compensated while uncompensated net moments arise perpendicular to the surface. Second, only collinear configurations of the spin structure were considered in the calculations. In the collinear calculations, the ferromagnetic coupling between Mn and Ni atoms at surface is favored over the antiferromagnetic coupling. The experimental results clearly shows a noncollinear spin structure from the voltage dependence of the spin images. It is expected that the noncollinear configuration of the surface moments will reduce the total energy which may lead to the magnetically compensated surface.

With above discussions, a conclusion about the spin structure of NiMn thin films and surfaces can be drawn. The *ab-initio* calculations show large magnetic moments on Mn sites and small moments on Ni sites at the surface. Nearest Mn atoms couple antiferromagnetically and next nearest Mn atoms couple ferromagnetically. However, the magnetic axis of this collinear structure is not clear. Sp-STM measurements shows the spin structure of NiMn surface is more complicated. Ni and Mn show opposite, but comparable magnitude of spin polarization at the surface at positive bias voltage. At negative voltage, two nearest Mn (Ni) surface atoms show very different magnitude of spin polarization resulting in a $p(2 \times 2)$ unit cell. This agrees with the topographic observation which imply the magnetic interaction between surface atoms is responsible for the broken symmetry. The NiMn surface has a noncollinear spin structure which leads to the in-plane compensation of surface spin polarization.

5.5   Future prospect: Co/NiMn bilayer on Cu(001)

Ferromagnetic (FM) layers in direct contact with antiferromagnetic (AFM) layers have attracted interests in the last two decades. Due to the exchange coupling between the FM and AFM layer, the FM layer is pinned by the AFM layer. The FM/AFM bilayer is widely used in spin valve structures. However, the physical principle of exchange coupling is not clear. It is generally believed that the interface between FM and AFM layers plays an important role. The Co/NiMn bilayer system was intensively studied in sputtered films [101, 102, 103, 104]. These studies mostly focus on improving the quality of NiMn films as an AFM pinning layer. These films are in a poly-crystalline phase where the AFM domains are disordered. The only study of single crystalline Co/NiMn bilayer was done in our institute by C. Tieg [109]. He observed the breakdown of large Co domains of hundreds of μm into small domains of a few μm in Co/NiMn bilayer on Cu(001) as the thickness NiMn exceeds a certain thickness which is believed as the onset of antiferromagnetism

in the NiMn thin films. The domains were observed with PEEM which is element specific so that in the same time. Domains of Mn and Ni were also observed. They agree with the Co domains. XMCD-PEEM is sensitive to ferromagnetic order. Domains of Mn (Ni) imply that the magnetic moments of Mn (Ni) atoms are aligned ferromagnetically to one direction. The thickness dependent measurements demonstrate the ferromagnetic order of Mn (Ni) is only present at the interface which is induced by the Co moments. The NiMn film still keeps its antiferromagnetic structure.

Following the results of C. Tieg [109], we deposited Co on NiMn/Cu(001) and imaged them with Sp-STM. Preliminary results were obtained. Figure 5.22 (b) shows a domain wall in the Co film running across the image separating two large domains. The domain size already exceeds the scan area which means the domains are lager than a few μm. In the zoomed image as shown in Fig. 5.23, one can clearly see that the domain wall runs along the step edge. The wall width is estimated to 15 nm.

A few notes should be made for these images. The Cu(001) surface is usually characterized by terraces in a few hundred nanometers range and step bunches where the step density is high. The atomic steps run along [110] direction of the crystal. In the presence of defects at the surface as shown in Fig. 5.22 (a), the steps are not straight. They have a chord like shape. In this case, parts of the steps are along [110] while other parts are more close to [100] direction as shown in Fig. 5.23 (a). The domain walls of Co were observed in areas of [100] steps. One possible reason for this can be related to the antiferromagnetic domains of NiMn thin films.
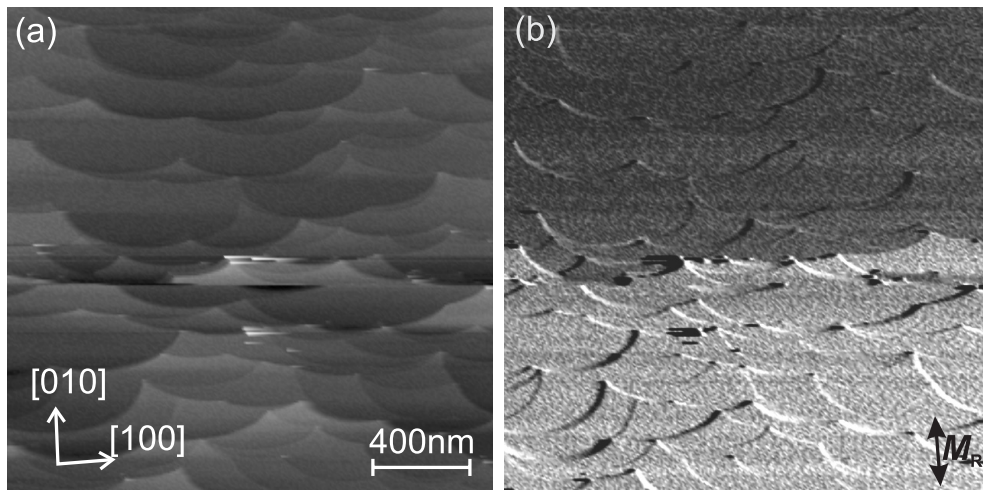

Figure 5.22: Topography (a) and corresponding spin signal (b) of 4 ML Co on 14 NiMn/Cu(001).

There are two structural domains which are perpendicular to each other in NiMn films. The NiMn thin films consist of alternating Mn and Ni atomic sheets which are perpendicular to the surface. The structural domains arise from the orientation

of the Mn (Ni) sheets, i.e., parallel to [100] or [010] crystalline direction. The structural domains are responsible for the magnetic domains on the NiMn surface. The structural domain sizes are typically of around 10 nm. Compared to the long exchange length of Co of the order of 30 nm, the contribution of the pinning effect from NiMn is locally canceled out. Due to the fact that the domain walls of Co run along the step edges of Cu(001), it can be expected at the step edge, the growth of NiMn has a preference for a certain direction. Mn (Ni) sheets are along [100] or [010] so that at the step edge along [110], the formation of the two kinds NiMn structural domains have equal probability. However, at the step edge along [100] or [010] direction, the Mn (Ni) sheets may grow along the step or perpendicular the step which may result in a preference for one orientated and by this to a large single structural domain along the step. In this larger domain, the exchange coupling is possibly not canceled yout. This assumption can explain why the domain walls of Co always appear at the step bunched area.
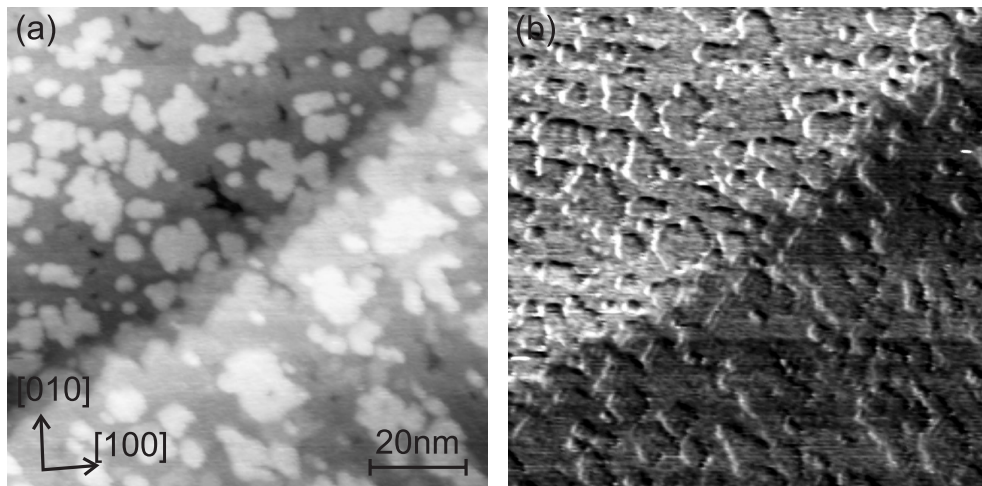

Figure 5.23: Enlarged images of Fig. 5.22. The domain wall runs along the step edge.

However, it is difficult to verify this assumption. First, one must demonstrate that NiMn forms single domains at the step edges along [100] and [010] directions. Second, one must demonstrate that the single domain causes the formation of Co domain walls along the step edges. We tried to increase the step density of the Cu surface by removing half a monolayer of Cu by Ar^+ sputtering followed by low temperature annealing. Almost square shaped atomic deep holes were created in this way. As already mentioned, in the equilibrium state, the steps on Cu(001) runs along [110] or [1$\bar{1}$0] direction. The holes created in this ways have step edges along [110] and [1$\bar{1}$0] as well. This does not lead to a preferential growth of single NiMn domain in this case. A miscut Cu surface with [100] steps is also not an option because these step edges are unstable and the step edges along [110] or [1$\bar{1}$0] are formed. The key point in solving this problem is to find step edges that run along [100] direction. It is not easy to obtain them in high amount while it is still possible

in a localized area, for example, as shown in Fig. 5.23. We will try to figure out the NiMn domains at step edges along [100] direction by resolving the atomic spin structure. This may give some hints about the mechanism of FM/AFM exchange coupling of this system.

6. Conclusion

In this work, the surface spin structure of antiferromagnetic thin films was studied on the atomic scale with spin-polarized scanning tunneling microscopy operating in the differential magnetic mode. In-plane spin sensitivity was achieved by using a soft magnetic ring as STM electrode. The magnetization direction of the ring is switched periodically by applying a high frequency alternating current to the coil wound around the ring. In the case of a magnetic surface, the tunneling current depends on the relative orientation between the magnetization direction of the surface and the ring due to the tunneling magnetic resistance effect. The change of the tunneling current upon the reversal of the tip can be extracted by the lock-in amplifier. The signal is proportional to the projection of the spin polarization of the surface atoms on the ring direction. The advantage of the technique is the well defined in-plane direction of spin sensitivity which is determined by the shape anisotropy of the ring. This is essential in resolving noncollinear antiferromagnetic spin structures.

Two different systems were investigated. One is the surface of reconstructed Mn films grown on Fe(001). The other is equiatomic NiMn films on Cu(001).

When Mn was deposited on Fe(001) at a substrate temperature of 373 K, the pseudomorphic growth changes to the three-dimensional growth at a Mn thickness of 10 to 20 ML depending on the growth conditions. The change of growth mode is accompanied by a structural transition from simple bct Mn to a $(\sqrt{10} \times 2\sqrt{10})R18.4°$ reconstructed Mn. The size of the reconstruction is 9 Å×18 Å which is twice as large as the α-Mn(001) surface unit cell. The Sp-STM measurements on the reconstructed Mn surface show that the reconstructed Mn has a noncollinear antiferromagnetic spin structure at room temperature. The non-collinearity of the spin structure is consistent with the noncollinear antiferromagnetic spin structure of α-Mn. Atomic resolution within the reconstruction unit cell was achieved in both structure and spin. Mn atoms at surface tend to form dimers. An antiparallel magnetic coupling of the two atoms of one dimer was demonstrated by comparing the structural and spin images. From two orthogonal scans, the vector field of the spin polarization of the large unit cell was constructed.

Equiatomic NiMn adopts an almost perfect layer-by-layer growth on Cu(001) in the co-evaporation mode. The NiMn thin films have a face centered tetragonal structure with the Mn and Ni occupying alternating atomic sheets. The Mn (Ni) sheets are perpendicular to the surface which result in two perpendicular structural

domains. The top most surface layer is reconstructed with Mn atoms sticking out in comparison to the position of Ni atoms. Sp-STM measurements showed the surface is compensated. A noncollinear surface spin configuration was observed. The surface spin structure was influenced by the two-fold symmetry of the thin film. Voltage dependent spin images shows a possible interaction between surface Mn (Ni) atoms which may be responsible for the weak $p(2 \times 2)$ diffraction pattern observed in LEED. A spin model combining the theoretical calculation and the experimental results was proposed. Finally, the exchange coupling in Co/NiMn bilayer is discussed. Domain walls in Co were found following the [001] step edge of the Cu substrate.

Bibliography

[1] Hubert, A. & Schäfer, R. Magnetic domains: the analysis of magnetic microstructures. *Springer, Berlin* (1998).

[2] Bitter, F. Experiments on the nature of ferromagnetism. *Phys. Rev.* **41**, 507 (1932).

[3] Hubert, A. Theory of 2-phase domain structures in superconductors and ferromagnets. *Phys. Status Solidi* **24**, 669 (1967).

[4] Martin, Y. & Wickramasinghe, H. K. Magnetic imaging by 'force microscopy' with 1000 Å resolution. *Appl. Phys. Lett.* **50**, 1455 (1987).

[5] Abelmann, L. *et al.* Comparing the resolution of magnetic force microscopes using the CAMST reference samples. *J. Magn. Magn. Mater.* **190**, 135 (1998).

[6] Williams, H. J., Foster, F. G. & Wood, E. A. Observation of magnetic domains by the Kerr effect. *Phys. Rev.* **82**, 119 (1951).

[7] Durkan, C., Shvets, I. V. & Lodder, J. C. Observation of magnetic domains using a reflection-mode scanning near-field optical microscope. *Appl. Phys. Lett.* **70**, 1323 (1997).

[8] Kirk, K. J., Chapman, J. N., McVitie, S., Aitchison, P. R. & Wilkinson, C. D. W. Switching of nanoscale magnetic elements. *Appl. Phys. Lett.* **75**, 3683 (1999).

[9] Koike, K., Matsuyama, H., Todokoro, H. & Hayakawa, K. Magnetic domain observation using spin-polarized scanning electron-microscopy. *Scanning Microscopy* **1**, 31 (1987).

[10] Graf, J., Jozwiak, C., Schmid, A. K., Hussain, Z. & Lanzara, A. Mapping the spin-dependent electron reflectivity of Fe and Co ferromagnetic thin films. *Phys. Rev. B* **71**, 144429 (2005).

[11] Chen, C. T. *et al.* Element-specific magnetic hysteresis as a means for studying heteromagnetic multilayers. *Phys. Rev. B* **48**, 642 (1993).

[12] Heinze, S. *et al.* Real-space imaging of two-dimensional antiferromagnetism on the atomic scale. *Science* **288**, 1805 (2000).

[13] Binnig, G., Rohrer, H., Gerber, C. & Weibel, E. Tunneling through a controllable vacuum gap. *Appl. Phys. Lett.* **40**, 178 (1982).

[14] Binnig, G., Rohrer, H., Gerber, C. & Weibel, E. Surface studies by scanning tunneling microscopy. *Phys. Rev. Lett.* **49**, 57 (1982).

[15] Julliere, M. Tunneling between ferromagnetic films. *Phys. Lett. A.* **54**, 225 (1975).

[16] Pierce, D. T. Spin-polarized electron microscopy. *Physica. Scripta* **38**, 291 (1988).

[17] Alvarado, S. F. & Renaud, P. Observation of spin-polarized-electron tunneling from a ferromagnet into GaAs. *Phys. Rev. Lett.* **68**, 1387 (1992).

[18] Yamada, T., Kunitomi, N., Nakai, Y., Cox, D. & Shirane, G. Magnetic structure of α-Mn. *J. Phys. Soc. Jpn.* **28**, 615 (1970).

[19] Lawson, A. C. *et al.* Magnetic and crystallographic order in α-manganese. *J. Appl. Phys.* **76**, 7049 (1994).

[20] Yamada, T. & Tazawa, S. Magnetic symmetry of α-Mn and parasitic ferromagnetism from magnetic torque measurements. *J. Phys. Soc. Jpn.* **28**, 609 (1970).

[21] Yamagata, H. & Asayama, K. NMR study of antiferromagnetic α-Mn metal. *J. Phys. Soc. Jpn.* **28**, 609 (1970).

[22] Walker, T. G. & Hopster, H. Magnetism of Mn layers on Fe(100). *Phys. Rev. B* **48**, 3563 (1993).

[23] Schlickum, U., Janke-Gilman, N., Wulfhekel, W. & Kirschner, J. Step-induced frustration of antiferromagnetic order in Mn on Fe(001). *Phys. Rev. Lett.* **92**, 107203 (2004).

[24] Kleiber, M., Bode, M., Ravlić, R. & Wiesendanger, R. Topology-induced spin frustrations at the Cr(001) surface studied by spin-polarized scanning tunneling spectroscopy. *Phys. Rev. Lett.* **85**, 4606 (2000).

[25] Tulchinsky, D., Unguris, J. & Celotta, R. Growth and magnetic oscillatory exchange coupling of Mn/Fe(001) and Fe/Mn/Fe(001). *J. Magn. Magn. Mater.* **212**, 91 (2000).

[26] Stöhr, J. *et al.* Images of the antiferromagnetic structure of a NiO(100) surface by means of X-Ray magnetic lineardichroism spectromicroscopy. *Phys. Rev. Lett.* **83**, 1862 (1999).

[27] Balcar, E. & Lovesey, S. W. Theory of magnetic neutron and photon scattering. *Oxford University Press* (1989).

[28] Roth, W. L. Magnetic Structures of MnO, FeO, CoO, and NiO. *Phys. Rev.* **110**, 1333 (1958).

[29] Shaked, H., J. Faber, J. & Hitterman, R. L. Low-temperature magnetic structure of MnO: a high-resolution neutron-diffraction study. *Phys. Rev. B.* **38**, 11901 (1988).

[30] Bradley, A. J. & Thewlis, J. The crystal structure of α-manganese. *Proc. R. Soc. London, Ser. A* **115**, 456 (1927).

[31] Kuch, W. *et al.* Tuning the magnetic coupling across ultrathin antiferromagnetic films by controlling atomic-scale roughness. *Nature Materials* **5**, 128 (2006).

[32] Nakamura, K., Freeman, A. J., Wang, D. S., Zhong, L. & Fernandez-de-Castro, J. Magnetic structures at the ferromagnetic NiFe and antiferromagnetic NiMn interface in exchange-biased films: Role of noncollinear magnetism and roughness. *Phys. Rev. B.* **65**, 012402 (2001).

[33] Kawagoe, T., Suzuki, Y., Bode, M. & Koike, K. Evidence of a topological antiferromagnetic order on ultrathin Cr(001) film surface studied by spin-polarized scanning tunneling spectroscopy. *J. Appl. Phys.* **93**, 6575 (2003).

[34] Kuch, W. *et al.* Three-dimensional noncollinear antiferromagnetic order in single-crystalline FeMn ultrathin films. *Phys. Rev. Lett.* **92**, 017201 (2004).

[35] Hamers, R. J. Atomic-resolution surface spectroscopy with the scanning tunneling microscopy. *Annu. Rev. Phys. Chem.* **40**, 531 (1989).

[36] Bardeen, J. Tunneling from a many-particle point of view. *Phys. Rev. Lett.* **6**, 57 (1961).

[37] Tersoff, J. & Hamann, D. R. Theory and application for the scanning tunneling microscope. *Phys. Rev. Lett.* **50**, 1998 (1983).

[38] Tersoff, J. & Hamann, D. R. Theory of the scanning tunneling microscope. *Phys. Rev. B.* **31**, 805 (1985).

[39] Slonczewski, J. C. Conductance and exchange coupling between two ferromagnets separated by a tunneling barrier. *Phys. Rev. B.* **39**, 6995 (1989).

[40] Alvarado, S. F. Tunneling potential barrier dependence of electron spin polarization. *Phys. Rev. Lett.* **75**, 513 (1995).

[41] Suzuki, Y., Nabhan, W. & Tanaka, K. Magnetic domains of cobalt ultrathin films observed with a scanning tunneling microscope using optically pumped GaAs tips. *Appl. Phys. Lett.* **71**, 3153 (1997).

[42] Johnson, M. & Clark, J. Spin-polarized scanning tunneling microscope: copcept, design and preliminary results from a prototype operated in air. *J. Appl. Phys.* **67**, 6141 (1990).

[43] Wortmann, D., Heinze, S., Kurz, P., Bihlmayer, G. & Blügel, S. Resolving complex atomic-scale spin structures by spin-polarized scanning tunneling microscopy. *Phys. Rev. Lett.* **86**, 4132 (2001).

[44] Wiesendanger, R., Güntherodt, H.-J., Güntherodt, G., Gambino, R. J. & Ruf, R. Observation of vacuum tunneling of spin-polarized electrons with the scanning tunneling microscope. *Phys. Rev. Lett.* **65**, 247 (1990).

[45] Bode, M., Getzlaff, M. & Wiesendanger, R. Spin-polarized vacuum tunneling into the exchange-split surface state of Gd(0001). *Phys. Rev. Lett.* **81**, 4256 (1998).

[46] Kubetzka, A. *et al.* Revealing antiferromagnetic order of the Fe monolayer on W(001): spin-polarized scanning tunneling microscopy and first-principles calculations. *Phys. Rev. Lett.* **94**, 087204 (2005).

[47] Schlickum, U. Spin-polarized scanning tunneling microscopy studies on in-plane magnetization components of thin antiferromagnetic films on Fe(001). *Ph.D thesis* (2005). Halle.

[48] Wulfhekel, W. & Kirschner, J. Spin-polarized scanning tunneling microscopy on ferromagnets. *Appl. Phys. Lett.* **75**, 1944 (1999).

[49] Schlickum, U., Wulfhekel, W. & Kirschner, J. Spin-polarized scanning tunneling microscope for imaging the in-plane magnetization. *Appl. Phys. Lett.* **83**, 2016 (2003).

[50] Heinze, S., Blügel, S., Pascal, R., Bode, M. & Wiesendanger, R. Prediction of bias-voltage-dependent corrugation reversal for STM images of bcc (110) surfaces: W(110), Ta(110), and Fe(110). *Phys. Rev. B.* **58**, 16432 (1998).

[51] Berdunov, N., Murphy, S., Mariotto, G. & Shvets, I. V. Atomically resolved spin-dependent tunneling on the Oxygen-terminated $Fe_3O_4(111)$. *Phys. Rev. Lett.* **93**, 057201 (2004).

[52] Yang, H., Smith, A. R., Prikhodko, M. & Lambrecht, W. R. L. Atomic-scale spin-polarized scanning tunneling microscopy applied to $Mn_3N_2(010)$. *Phys. Rev. Lett.* **89**, 226101 (2002).

[53] Hofer, W. A., Foster, A. S. & Shluger, A. L. Theories of scanning probe microscopes at the atomic scale. *Rev. Morden. Phys.* **75**, 1287 (2003).

[54] Wintterlin, J. *et al.* Atomic-resolution imaging of close-packed metal surfaces by scanning tunneling microscopy. *Phys. Rev. Lett.* **62**, 59 (1989).

[55] Wöll, C., Chiang, S., Wilson, R. J. & Lippel, P. H. Determination of atom positions at stacking-fault dislocations on Au(111) by scanning tunneling microscopy. *Phys. Rev. B.* **39**, 7988 (1989).

[56] Chen, C. J. Origin of atomic resolution on metal surfaces in scanning tunneling microscopy. *Phys. Rev. Lett.* **65**, 448 (1990).

[57] Hofer, W. A., Redinger, J. & Podloucky, R. Modeling STM tips by single absorbed atoms on W(100) films: 3d and 4d transition-metal atoms. *Phys. Rev. B.* **64**, 125108 (2001).

[58] Hofer, W. A., Redinger, J. & Vargab, P. Modeling STM tips by single absorbed atoms on W(100) films: 5d transition metal atoms. *Solid State Communications* **113**, 245 (2000).

[59] Sacks, W., Gauthier, S., Rousset, S., Klein, J. & Esrick, M. A. Surface topography in scanning tunneling microscopy: A free-electron model. *Phys. Rev. B.* **36**, 961 (1987).

[60] Ertl, G. & Küppers, J. Low energy electrons and surface chemistry. *VHC, Weinheim* (1985).

[61] Auger, P. The effect of a photoelectric compound. *Journal de Physique et le Radium* **6**, 205–U12 (1925).

[62] Pendry, J. B. Low energy electron diffraction. *Academic Press, London* (1974).

[63] Heinz, K. LEED and DLEED as modern tools for quantitative surface structure determination. *Rep. Prog. Phys* **58**, 637 (1995).

[64] Braun, W. Applied RHEED: reflection high-energy electron diffraction during crystal growth. *Springer, Berlin* (1999).

[65] Kirschner, J., Engelhard, H. & Hartung, D. An evaporation source for ion beam assisted deposition in ultrahigh vacuum. *Review of Scientific Instruments* **73**, 3853 (2002).

[66] Forino, M. Tip sharpening by normal and reverse electrochemical etching. *Review of Scientific Instruments* **64**, 159 (1993).

[67] Oepen, H. P. & Kirschner, J. Magnetization distribution of 180° domain walls at Fe(100) single-crystal surfaces. *Phys. Rev. Lett.* **62**, 819 (1989).

[68] Hobbs, D., Hafner, J. & Spišák, D. Understanding the complex metallic element Mn. I. Crystalline and noncollinear magnetic structure of α-Mn. *Phys. Rev. B.* **68**, 014407 (2003).

[69] Tebble, R. & Craik, D. Magnetic materials. *Intersicence, London* (1969).

[70] Asada, T. Electronic structures and magnetism of α and β Mn. *J. Magn. Magn. Mater.* **140-144**, 47 (1995).

[71] Preston, G. D. The crystal structure of β-manganese. *Philos. Mag.* **5**, 1207 (1928).

[72] Kasper, J. S. & Roberts, B. W. Antiferromagnetic structure of α-Manganese and a magnetic structure study of β-Manganese. *Phys. Rev.* **101**, 537 (1956).

83

[73] Masuda, Y., Kobayashi, S., Asayama, K. & Itoh, J. Nuclear magnetic resonance in α- and β-Magnanese metals. *J. Phys. Soc. Jpn.* **19**, 460 (1964).

[74] Jo, T. & Hirai, K. Lattice distortion and multiple spin density wave state in γ-Mn alloys. *J. Phys. Soc. Jpn.* **55**, 2017 (1986).

[75] Uchishib, H. Antiferromagnetism of γ-phase manganese alloys containing Ni, Zn, Ga, and Ge. *J. Phys. Soc. Jpn.* **31**, 346 (1971).

[76] Arrott, A. S., Heinrich, B., Purcell, S. T., Cochran, J. F. & Urquhart, K. B. Engineering magnetic materials on the atomic scale. *J. Appl. Phys.* **61**, 3721 (1987).

[77] Tian, D., Li, H., Wu, S. C., Jona, F. & Marcus, P. M. Atomic and electronic structure of thin films of Mn on Pd(111). *Phys. Rev. B.* **45**, 3749 (1992).

[78] Ounadjela, K. *et al.* Structural changes in metastable epitaxial Co/Mn superlattices. *Phys. Rev. B.* **49**, 8561 (1994).

[79] Andrieu, S., Fischer, H. M., Piecuch, M., Traverse, A. & Mimault, J. Structure of Mn films grown on (111) and (001) fcc Ir determined by EXAFS and the multiple-scattering approach. *Phys. Rev. B.* **54**, 2822 (1996).

[80] Grigorov, I. L., Fitzsimmons, M. R., Siu, I.-L. & Walker, J. C. Observation and analysis of multidomain epitaxy of α-Mn on MgO(111). *Phys. Rev. Lett.* **82**, 5309 (1999).

[81] Wuttig, M., Gauthier, Y. & Blügel, S. Magnetically driven buckling and stability of ordered surface alloys: Cu(100) $c(2 \times 2)$Mn. *Phys. Rev. Lett.* **70**, 3619 (1993).

[82] Rader, O. *et al.* Electronic structure of two-dimensional magnetic alloys: $c(2 \times 2)$ Mn on Cu(100) and Ni(100). *Phys. Rev. B.* **55**, 5404 (1997).

[83] Kim, S. K., Tian, Y., Montesano, M., Jona, F. & Marcus, P. M. Simple structure and soft elastic behavior of Mn on Fe(001). *Phys. Rev. B.* **54**, 5081 (1996).

[84] Andrieu, S. *et al.* Growth, structure, and magnetic properties of thin Mn films epitaxially grown on (001) bcc Fe. *Phys. Rev. B.* **57**, 1985 (1998).

[85] Passamani, E. C., Croonenborghs, B., Degroote, B. & Vantomme, A. Interface and bulk properties of Fe/Mn sandwich structures. *Phys. Rev. B.* **67**, 174424 (2003).

[86] Pierce, D. *et al.* Non-collinear exchange coupling in Fe/Mn/Fe(001): insight from scanning tunneling microscopy. *J. Magn. Magn. Mater.* **222**, 13 (2000).

[87] Sliwko, V., Mohn, P. & Schwarz, K. The electronic and magnetic structures of α- and β-manganese. *J. Phys.: Condens. Matter* **6**, 6557 (1994).

[88] Antropov, V. P., van Schilfgaarde, M. & Harmon, B. Magnetic phase stability of 3d-metals and plutonium. *J. Magn. Magn. Mater.* **140-144**, 1355 (1995).

[89] Sawicki, M. Magnetic properties of (Ga,Mn)As. *J. Magn. Magn. Mater.* **300**, 1 (2006).

[90] Fishman, R. S., Lee, W.-T., Liu, S. H. & et al. Structural and magnetic phase transitions in Mn-Ni alloys. *Phys. Rev. B.* **61**, 12159 (2000).

[91] Cable, J. W. & Tsunoda, Y. Magnetic short-range order and magnetic mements of Co-Mn and Ni-Mn alloys. *Phys. Rev. B.* **50**, 9200 (1994).

[92] Malssaski, T. B., Murray, J. L., Bennett, L. H. & Baker, H. Binary alloy phase diagrams. *ASM, Materials Park, OH* **2nd ed** (1986).

[93] Ding, L., Ladwig, P. F., Yan, X. & Chang, Y. A. Thermodynamic stability and diffusivity of near-equiatomic Ni-Mn alloys. *Appl. Phys. A.* **80**, 1186 (2002).

[94] Abdul-Razzaq, W. & Kouvel, J. S. Magnetic phase diagram of disordered Ni-Mn near the multicritical point. *Phys. Rev. B.* **35**, 1764 (1987).

[95] Magnetic properties of metals. *Springer-Verlag* (1991).

[96] Paoletti, A. & Ricci, F. P. A polarized neutron investigation of the $MnNi_3$ alloy. *J. Appl. Phys.* **34**, 1571 (1963).

[97] Krén, E., Nagy, E., Nagy, I., Pál, L. & Szabó, P. Structures and phase trasnformations in Mn-Ni system near equiatomic concentration. *J. Phys. Chem. Solids* **29**, 101 (1968).

[98] Kasper, J. S. & Kouvel, J. S. The antiferromagnetic structure of NiMn. *J. Phys. Chem. Solids* **11**, 231 (1959).

[99] Spišák, D. & Hafner, J. Electronic and magnetic structure of Mn-Ni alloys in two and three dimensions. *J. Phys.: Condens. Matter* **11**, 6359 (1999).

[100] Sakuma, A. Electronic structures and magnetism of CuAu-type MnNi and MnGa. *J. Magn. Magn. Mater.* **187**, 105 (1998).

[101] Toney, M. F., Samant, M. G., Lin, T. & Mauri, D. Thickness dependence of exchange bias and structure in MnPt and MnNi spin valves. *Appl. Phys. Lett.* **81**, 4565 (2002).

[102] Oppeneer, P. M. *et al.* Buried antiferromagnetic films investigated by x-ray magneto-optical reflection spectroscopy. *Phys. Rev. B.* **67**, 052401 (2003).

[103] Spenato, D., Youssef, J. B., Gall, H. L. & Ostoréro, J. From ferromagnetic-ferromagnetic to ferromagnetic-antiferromagnetic exchange coupling in NiFe/MnNi bilayers. *J. Appl. Phys.* **89**, 6898 (2001).

[104] Wang, Y.-H., Lai, C.-H., Chang, C.-R., Yang, J.-S. & Lo, C. K. Uniaxial anisotropy induced by field annealing in (001) NiMn/Co films. *J. Appl. Phys.* **89**, 6603 (2001).

[105] Thamankar, R., Bhagwat, S. & Schumann, F. O. Perpendicular anisotropy in Ni rich Ni_xMn_{1-x} ultrathin films. *J. Phys.: Condens. Matter* **16**, 6029 (2004).

[106] Wuttig, M. & Knight, C. C. LEED structure determination of tetragonal MnNi films on Ni(100). *Phys. Rev. B.* **48**, 12130 (1993).

[107] Wuttig, M., Flores, T. & Knight, C. C. Structure and growth of Mn on Ni(100). *Phys. Rev. B.* **48**, 12082 (1993).

[108] O'Brien, W. L. & Tonner, B. P. Magnetic propertis of Mn/Cu(001) and MnNi/Ni(001)c(2×2) surface alloys. *Phys. Rev. B.* **51**, 617 (1995).

[109] Tieg, C. Growth, structure and magnetic properties of single-crystalline antiferromagnetic NiMn films and bilayer of NiMn and Co on Cu(001). *Ph.D thesis* (2005). Halle.

[110] Huang, F., Kief, M. T., Mankey, G. J. & Willis, R. F. Magnetism in the few monolayers limit: a surface magneto-optical Kerr-effect study of the magnetic behavior of ultrathin films of Co, Ni and Co-Ni alloys on Cu(100) and Cu(111). *Phys. Rev. B.* **49**, 3962 (1994).

[111] Shen, J., Giergiel, J. & Kirschner, J. Growth and morpholpgy of Ni/Cu(100) ultrathin films: An *in situ* study using scanning tunneling microscopy. *Phys. Rev. B.* **52**, 8454 (1995).

[112] Bode, M. *et al.* Atomic spin structure of antiferromagnetic domain walls. *Nature Materials* **5**, 477 (2006).

[113] Smith, A. R., Yang, R. & Yang, H. Bias-voltage dependence in atomic-scale spin polarized scanning tunneling microscopy of Mn_3N_2(010). *Mater. Res. Soc.* **804**, 41 (2004).

[114] Schlickum, U. *et al.* Effect of antiferromagnetic layers on the spin-dependent transport in magnetic tunnel junctions. *Phys. Rev. B.* **74**, 054409 (2006).

[115] Perdew, J. P. & Wang, Y. Accurate and simple analytic representation of the electron-gas correlation energy. *Phys. Rev. B.* **45**, 13244 (1992).

[116] Ernst, A., Lueders, M., Temmerman, W. M., Szotek, Z. & van der Laan, G. Theoretical study of magnetic layers of nickel on copper: dead or alive? *J. Phys.: Condens. Matter* **12**, 5599 (2000).

Acknowledgements

.

Curriculum vitae

First Name	Chunlei
Family Name	Gao
Date of Birth	March 16, 1977 (Jiangsu, P. R. China)
Nationality	Chinese
E-mail	*clgao@mpi-halle.de*

EDUCATION

Aug. 2003 - present	Max Planck Institute of Microstructure Physics and Martin-Luther-University Halle Wittenberg (Halle, Germany) Ph.D. candidate (Supervisor: Prof. Jürgen Kirschner)
Aug. 2000 - Jul. 2003	Fudan University (Shanghai, P. R. China) Master's Degree in Physics
Aug. 1996 - Jul. 2000	Fudan University (Shanghai, P. R. China) Bachelor's Degree in Physics

.

Eidesstattliche Erklärung

Ich erkläre hiermit, dass ich keine anderen als die von mir angegebenen Quellen und Hilfsmittel zur Erstellung meiner Dissertation verwendet habe. Den benutzten Werken wörtlich oder inhaltlich entnommene Stellen sind als solche gekennzeichnet.

Chunlei Gao

Halle (Saale), im September 2006